

Large Interferometer For Exoplanets (LIFE):

III. Spectral resolution, wavelength range and sensitivity requirements based on atmospheric retrieval analyses of an exo-Earth

B.S. Konrad^{1,2,*}, E. Alei^{1,2}, D. Angerhausen^{1,2,3}, Ó. Carrión-González⁴, J.J. Fortney⁵, J.L. Grenfell⁶, D. Kitzmann⁷, P. Mollière⁸, S. Rugheimer⁹, F. Wunderlich⁶, S.P. Quanz^{1,2}, and the *LIFE* Collaboration¹⁰

¹ ETH Zurich, Institute for Particle Physics & Astrophysics, Wolfgang-Pauli-Str. 27, 8093 Zurich, Switzerland

² National Center of Competence in Research PlanetS (www.nccr-planets.ch)

³ Blue Marble Space Institute of Science, Seattle, United States

⁴ Zentrum für Astronomie und Astrophysik, Technische Universität Berlin, Hardenbergstrasse 36, D-10623 Berlin, Germany

⁵ Department of Astronomy and Astrophysics, University of California, Santa Cruz, CA, USA 95064

⁶ Department of Extrasolar Planets and Atmospheres (EPA), Institute of Planetary Research (PF), German Aerospace Centre (DLR), Rutherfordstr. 2, 12489 Berlin, Germany

⁷ University of Bern, Center for Space and Habitability, Gesellschaftsstrasse 6, 3012 Bern, Switzerland

⁸ Max-Planck-Institut für Astronomie, Königstuhl 17, 69117 Heidelberg, Germany

⁹ Dept of Physics, University of Oxford, Oxford, OX1 3PU, UK

¹⁰ www.life-space-mission.com

Received -; accepted -

ABSTRACT

Context. Temperate terrestrial exoplanets are likely to be common objects, but their discovery and characterization is very challenging because of the small intrinsic signal compared to that of their host star. Various concepts for optimized space missions to overcome these challenges are currently being studied. The *LIFE* initiative focuses on the development of a space-based mid-infrared (MIR) nulling interferometer probing the thermal emission of a large sample of exoplanets.

Aims. This study derives the minimum requirements for the signal-to-noise ratio (S/N), the spectral resolution (R), and the wavelength coverage for the *LIFE* mission concept. Using an Earth-twin exoplanet as reference case, we quantify how well planetary/atmospheric properties can be derived from its MIR thermal emission spectrum as a function of wavelength range, S/N and R .

Methods. We combine a cloud-free 1D atmospheric radiative transfer model, a noise model for observations with the *LIFE* interferometer and the nested sampling algorithm for Bayesian parameter inference to retrieve for planetary/atmospheric properties. We simulate observations of an Earth-twin exoplanet orbiting a G2V star at 10 pc from the Sun with different levels of exozodiacal dust emissions. We investigate a grid of wavelength ranges (3 – 20 μm , 4 – 18.5 μm , and 6 – 17 μm), S/N s (5, 10, 15, and 20 determined at a wavelength of 11.2 μm) and R s (20, 35, 50, and 100).

Results. H_2O , CO_2 , and O_3 are detectable if $S/N \geq 10$ (uncertainty $\leq \pm 1.0$ dex). We find upper limits for N_2O (abundance $\leq 10^{-3}$), CO , N_2 , and O_2 are unconstrained in all cases. The lower limits for a CH_4 detection are $R = 50$, and $S/N = 10$. Our retrieval framework correctly determines the exoplanet's radius (uncertainty $\leq \pm 10\%$), surface temperature (uncertainty $\leq \pm 20$ K), and surface pressure (uncertainty $\leq \pm 0.5$ dex) in all cloud-free retrieval analyses. Based on our current assumptions, the observation time required to reach the specified S/N for an Earth-twin at 10 pc amounts to ≈ 6 -7 weeks with 4×2 -m apertures.

Conclusions. We provide first order estimates for the minimum technical requirements for *LIFE* via the retrieval study of an Earth-twin exoplanet. We conclude that a minimum wavelength coverage of 4 – 18.5 μm , a spectral resolution of $R = 50$ and an S/N of at least 10 is required. With the current assumptions, the atmospheric characterization of several Earth-like exoplanets at a distance of 10 pc and within a reasonable amount of observing time will require apertures ≥ 2 meters.

Key words. Methods: statistical – Planets and satellites: terrestrial planets – Planets and satellites: atmospheres

1. Introduction

Since the detection of 51 Peg b, the first planetary companion to a solar-type star (Mayor & Queloz 1995), exoplanet research has become one of the pillars of modern astrophysics. With more than 4000 exoplanets currently known¹, scientists have begun to uncover the vast diversity among exoplanet objects and extra-solar systems. A long-term goal is the discovery and the atmo-

spheric characterization of a large sample of terrestrial exoplanets, with a specific focus on temperate objects.

In this context, a direct detection approach is essential in order to investigate the diversity of planetary atmospheres, assess the potential habitability of some objects, and look for so-called biosignatures in their atmospheres. Different concepts for large exoplanet imaging space-missions are currently being assessed, with *LUVUOIR* (Peterson et al. 2017) and *HabEx* (Gaudi et al. 2020), which aim at directly measuring the reflected spectrum of exoplanets in the visible (VIS) and near-infrared (NIR) range, being prominent examples. The *Large In-*

* Correspondence: konradb@student.ethz.ch, sascha.quanz@phys.ethz.ch

¹ <https://exoplanetarchive.ipac.caltech.edu>

terferometer For Exoplanets (*LIFE*) initiative² follows a complementary approach by focusing on the prospects of a large, space-based mid-infrared (MIR) nulling interferometer which will observe the thermal emission spectrum and subsequently characterize the atmospheres of a large sample of (terrestrial) exoplanets (Quanz et al. 2018, 2019, 2021). The *LIFE* initiative aims to combine various efforts to push towards an eventual launch of such a large, space-based MIR nulling interferometer. The work we present here aims to constrain some of the instrument requirements for *LIFE* and is the third paper in a series. The first paper of the series (Quanz et al. 2021) quantifies the exoplanet detection performance of *LIFE* and compares it with large single-aperture mission concepts for reflected light. The second paper (Ottiger et al., *subm.*) introduces the *LIFE* instrument simulator and the necessary signal extraction algorithms.

The choice of the MIR wavelength range for *LIFE* pays dividends. More molecules have strong absorption bands in the MIR spectra of Earth-like planets which allows to better assess the atmospheric structure and composition (e.g., Des Marais et al. 2002; Line et al. 2019) and the infrared appears to be less affected by the presence of hazes and clouds (see, e.g., Kitzmann et al. 2011; Rugheimer et al. 2013; Arney et al. 2018; Lavvas et al. 2019; Fauchez et al. 2019; Komacek et al. 2020; Wunderlich et al. 2021), which is a major challenge at visible wavelengths (see, e.g., Sing et al. 2016, for Jovian planets).³ Importantly, emission spectra allow us to constrain the planetary radius (e.g., Line et al. 2019), which is degenerate with the planetary albedo in reflected-light measurements (Carrión-González et al. 2020).

Finally, the MIR range includes a rich portfolio of biosignatures (e.g., Catling et al. 2018). Biosignatures in an exoplanet context are gases or features that can be detected at interplanetary distances and that are produced by life. Among the main biosignature gases there are O₂ and its photochemical product ozone (O₃), methane (CH₄), nitrous oxide (N₂O), chloromethane (CH₃Cl), phosphine (PH₃), and dimethyl sulfide (C₂H₆S, commonly known as DMS). Many of these gases could also be generated by abiotic processes and therefore be false positives in the search for biosignatures (Schwieterman et al. 2018; Harman & Domagal-Goldman 2018). However, the presence of multiple biosignature gases in the spectrum, along with other planetary context that points towards habitability, would increase the robustness of the detection of life on an exoplanet. The most widely known set of multiple biosignatures is the so-called ‘triple fingerprint’ of carbon dioxide (CO₂), water vapor (H₂O) and ozone (O₃), well detectable in Earth’s thermal emission spectrum and potentially detectable in terrestrial exoplanets (see, e.g., Selsis et al. 2002). The simultaneous presence of reducing and oxidizing species in an atmosphere, such as O₂ and O₃ in combination with CH₄, is a strong combinatory biosignature, with no currently known false positives. These species would not be both present in large quantities in an atmosphere over long timescales without disequilibrium processes driven by the presence of life (Lederberg 1965; Lovelock 1965). We refer the reader to Schwieterman et al. (2018) for a review about biosignatures and Catling et al. (2018) for a Bayesian framework for assessing the confidence level of a biosignature detection.

While there is ample scientific justification for choosing the MIR wavelength regime for detailed (atmospheric) investiga-

tions of terrestrial exoplanets, deriving a concept for a space-mission, as pursued by the *LIFE* initiative, requires the derivation of fundamental mission and instrument requirements, including instrument sensitivity, wavelength range coverage and spectral resolution. Earlier steps in this direction were presented in von Paris et al. (2013) for the former *Darwin* mission concept (Léger et al. 1996). In a more recent study, Feng et al. (2018) used a Bayesian atmospheric retrieval approach to quantify the power of reflected light observations, as foreseen by *HabEx* or *LUVOIR*, as a function of instrument parameters.

Here, we aim at providing minimum requirements for the parameters listed above for the *LIFE* mission concept using an atmospheric retrieval framework. Such a framework allows us to derive quantitative estimates on the main atmospheric and planetary parameters from a simulated exoplanetary spectrum (see, e.g., Madhusudhan 2018; Deming et al. 2018; Barstow & Heng 2020, for recent reviews). Using a Bayesian approach, the space of input parameters (e.g., atmospheric abundances) is explored iteratively to assess which combination of values best fits the simulated observations. Doing that for various combinations of signal-to-noise ratio (S/N) of the emission spectrum, wavelength range and spectral resolution allows us to understand, how well the simulated planet can be characterized. In the present study, we use a cloud-free modern Earth-twin exoplanet as our reference case. As Earth is the only planet known to host life, we are particularly interested in assessing if and how well some of its main atmospheric constituents can be detected for various combinations of instrument parameters. We are aware that by ignoring clouds we are somewhat simplifying the problem. However, we remind the reader that the main aim of our analysis is to get first estimates for sensitivity, wavelength range and spectral resolution requirements for *LIFE*. Subsequent work will investigate other types of exoplanets and atmospheric compositions providing additional constraints on some of the requirements.

In Section 2, we introduce our retrieval framework. It combines a 1-D atmospheric forward model based on the *petitRADTRANS* radiative transfer code (Mollière et al. 2019), with the *LIFE* instrument simulator (Ottiger et al., *subm.*; cf. Quanz et al. 2021), that adds astrophysical noise terms to the simulated Earth spectrum, and a Nested Sampling approach (Skilling 2006) for Bayesian parameter inference. We validate the retrieval framework in Section 3. Then, we perform a series of retrievals of the theoretical emission spectrum of a cloud-free Earth-twin exoplanet as it would be observed by *LIFE*, varying the wavelength range, the S/N, and the spectral resolution. Results are presented in Section 4. We discuss our results and compare our study with other works in Section 5. We summarize our main findings and conclusions in Section 6.

2. Methods

Our atmospheric retrieval framework aims to infer the atmospheric P-T (pressure-temperature) structure and composition from simulated mock-observations of the MIR thermal emission spectrum of an Earth-twin planet. At its heart, the framework consists of two elements. Firstly, we need a parametric model for the atmosphere, which calculates the emergent light spectrum corresponding to a set of model parameters (Section 2.1). Secondly, a parameter estimation algorithm is required to optimize the model parameters, such that the spectrum produced by the atmospheric model best fits the simulated observational data (Section 2.2). These two elements are then combined to form our retrieval framework (Section 2.3). An illustrative schematic summarizing our retrieval framework is given in Figure 1.

² www.life-space-mission.com

³ However, clouds can also increase reflectivity and signal for molecules like molecular oxygen (O₂) that are well-mixed in the atmosphere of a terrestrial planet (Kawashima & Rugheimer 2019).

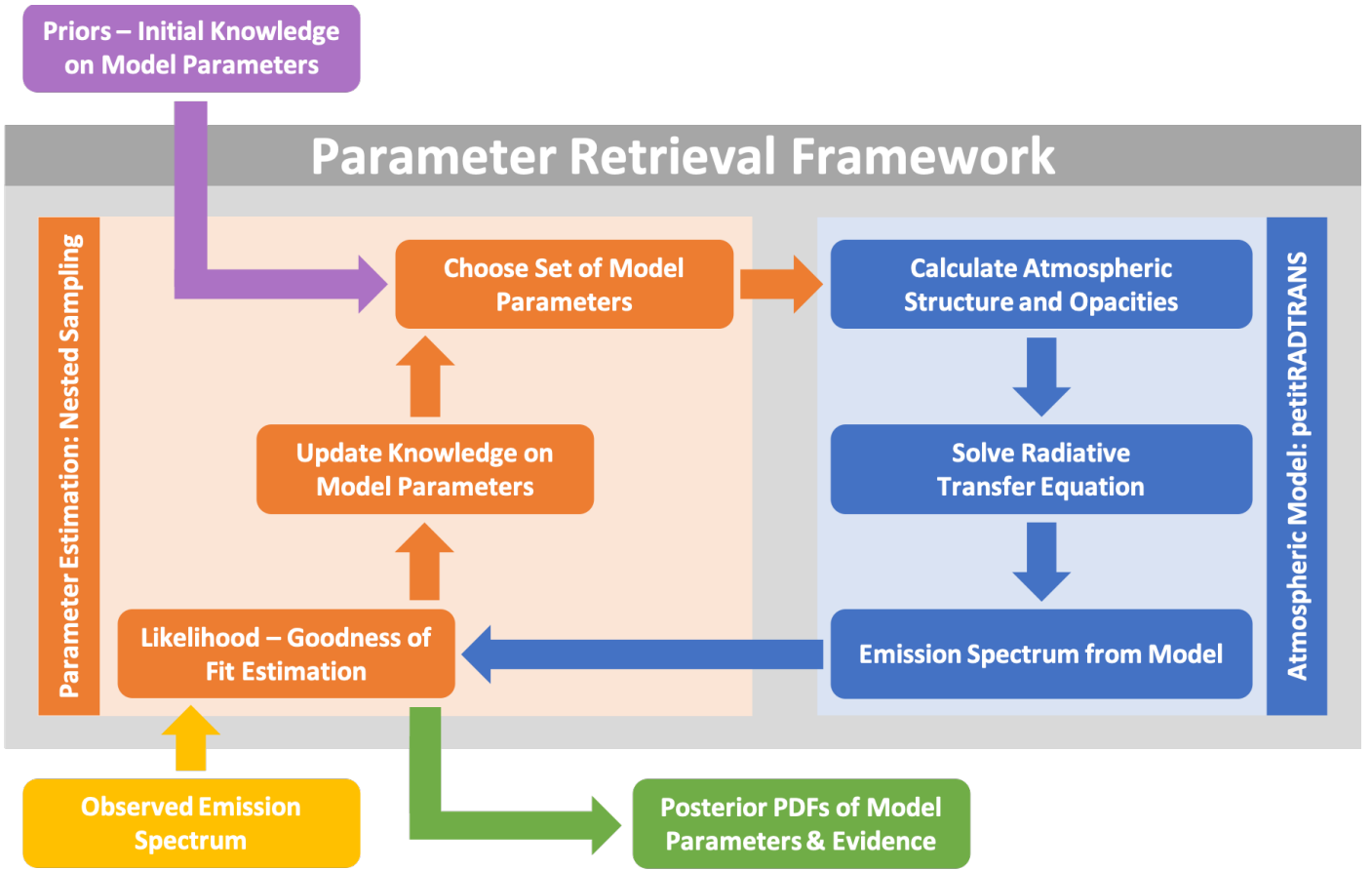


Fig. 1: Schematic illustrating our atmospheric retrieval framework.

2.1. Atmospheric Model

We use the 1-D radiative transfer code `petitRADTRANS` (Mollière et al. 2019). To calculate the thermal emission spectrum of terrestrial exoplanets in the MIR wavelength range, `petitRADTRANS` passes a featureless black-body spectrum at the surface temperature through discrete atmospheric layers, which interact with the radiation field. We characterize each layer by its temperature, pressure, and the opacity sources present.

2.1.1. Atmospheric Pressure-Temperature (P-T) Structure

Throughout this work, we parametrized the P-T structure of Earth’s atmosphere using a 4th order polynomial:

$$T(P) = \sum_{i=0}^4 a_i P^i. \quad (1)$$

Here, P denotes the atmospheric pressure and T the corresponding temperature. The parameters a_i are the parameters describing the polynomial P-T model. We chose this polynomial P-T model over other P-T profile parametrizations (e.g., models from Madhusudhan & Seager 2009; Guillot 2010; Mollière et al. 2019), since it provides a comparable description of the atmospheric P-T structure using fewer model parameters (see Appendix A for further information).

2.1.2. Opacity Sources in `petitRADTRANS`

`petitRADTRANS` is capable of considering several different opacity sources that are potentially present in exoplanet atmospheres. In the computationally favourable low spectral resolution mode ($R = 1000$), the opacities originating from different atmospheric gases are calculated via the correlated-k method (Goody et al. 1989; Lacis & Oinas 1991; Fu & Liou 1992). Absorption lines from different molecules, collision-induced absorption (CIA), and atmospheric pressure broadening effects can be taken into account. Rayleigh and cloud scattering, as well as the scattering of direct radiation from the host star, can be considered. However, the scattering solution is achieved in an iterative way and the opacity handling is different (see Mollière et al. 2020, for more information). These changes increase the spectrum calculation time by roughly an order of magnitude when scattering is included in the computation.

In Figure 2 we compare our scattering- and cloud-free Earth-twin MIR emission spectrum, which assumes uniform chemical abundances throughout the atmosphere to other cloud-free and cloudy models (Daniel Kitzmann, private communications; Rugheimer et al. 2015). These models consider scattering as well as non-uniform abundances. We see that scattering contributions and non-uniform abundances only have a minor impact on Earth’s in the MIR and the differences between the cloud-free spectra are of similar magnitude as the most optimistic `LIFESM` noise estimate. This justifies our approach of excluding scattering from our retrieval routine. Thus, we neglect effects linked to the incident stellar radiation, which reduces number of parameters retrieved and thereby the computing time.

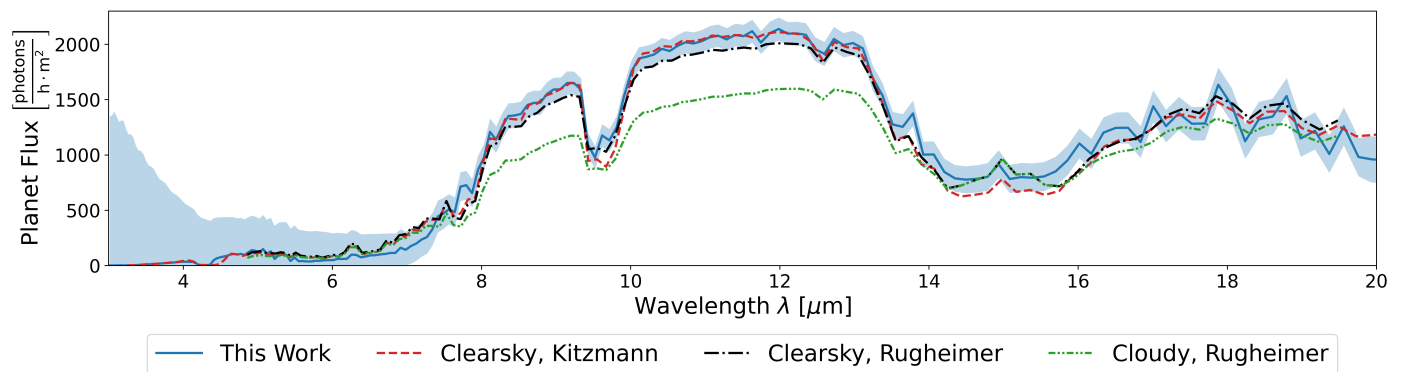


Fig. 2: Comparison of the Earth-twin MIR emission spectra calculated with various different models. We plot the photon flux received from an Earth-twin located 10 pc from the sun. The solid blue line is the MIR thermal emission calculated with `petitRADTRANS` using the settings discussed in Section 2.3.1. The blue-shaded region indicates the most optimistic LIFESM uncertainty ($S/N = 20$) used in our retrievals. The red dashed line represents a cloud-free Earth model which accounts for scattering by Daniel Kitzmann (private communications). The green and black dashed-dotted lines are the cloudy (60% cloud coverage) and cloud-free modern Earth spectra from Rugheimer et al. (2015) that account for scattering.

We also neglect scattering and absorption by clouds. As can be seen from Figure 2, this is a significant simplification of the problem. The presence of (opaque) clouds in an atmosphere will partially or fully obscure the view of the exoplanet’s surface. Therefore, we expect systematic shifts in the surface temperature/pressure and potentially also in the retrieved planetary radius if clouds are present in an atmosphere. Additionally, a partial cloud coverage combined with vertically non-constant atmospheric abundances could lead to systematic offsets in the retrieved abundances. For example, if an atmospheric gas is only present below an optically thick cloud deck, it is likely not detectable via a MIR retrieval study. These potential effects require further attention in future works. However, as we are interested in first estimates for specific instrument requirements, focusing on a cloud-free atmosphere is justifiable. Complete details on the implementation are given in Section 2.3.1.

2.2. Parameter Estimation

Our retrieval study utilizes a Bayesian parameter inference tool to sample the posterior probability distributions of the atmospheric forward model parameters.

Bayesian Parameter inference methods are based on Bayes’ theorem, which provides a method for estimating model parameters based on experimental data (see, e.g., Trotta 2017; van de Schoot et al. 2021). Let us consider a model \mathcal{M} described by a set of parameters $\Theta_{\mathcal{M}}$ and experimental data \mathcal{D} . Bayes’ theorem states:

$$P(\Theta_{\mathcal{M}}|\mathcal{D}, \mathcal{M}) = \frac{P(\mathcal{D}|\Theta_{\mathcal{M}}, \mathcal{M})P(\Theta_{\mathcal{M}}|\mathcal{M})}{P(\mathcal{D}|\mathcal{M})}. \quad (2)$$

$P(\Theta_{\mathcal{M}}|\mathcal{D}, \mathcal{M})$ is called posterior (or posterior probability) and represents the probability of different sets of model parameters $\Theta_{\mathcal{M}}$ under the constraint of the experimental data \mathcal{D} and model \mathcal{M} .

$P(\mathcal{D}|\Theta_{\mathcal{M}}, \mathcal{M})$ provides a probabilistic measure of how well a specific set of parameters $\Theta_{\mathcal{M}}$ for the model \mathcal{M} describes the data \mathcal{D} . We calculate this probability via a log-likelihood function $\ln(\mathcal{L}(\Theta_{\mathcal{M}}))$:

$$\ln(\mathcal{L}(\Theta_{\mathcal{M}})) = \sum_{i=1}^N \left(-\frac{1}{2} \ln(2\pi\sigma_i^2) - \frac{1}{2} \frac{(\mathcal{D}_i - \mu_i(\Theta_{\mathcal{M}}))^2}{\sigma_i^2} \right). \quad (3)$$

Table 1: Jeffrey’s scale (Jeffreys 1998).

$\log_{10}(K)$	Probability	Strength of Evidence
< 0	< 0.5	Support for \mathcal{M}_2
$0 - 0.5$	$0.5 - 0.75$	Very weak support for \mathcal{M}_1
$0.5 - 1$	$0.75 - 0.91$	Substantial support for \mathcal{M}_1
$1 - 2$	$0.91 - 0.99$	Strong support for \mathcal{M}_1
> 2	> 0.99	Decisive support for \mathcal{M}_1

Notes. Scale for the interpretation of the Bayes’ factor $K = \mathcal{Z}_{\mathcal{M}_1}(\mathcal{D})/\mathcal{Z}_{\mathcal{M}_2}(\mathcal{D})$. The scale is symmetrical, which means that negative values up to -2 correspond to very weak/substantial/strong/decisive support for \mathcal{M}_2 .

Our log-likelihood function assumes that each of the N measured data points \mathcal{D}_i behaves as a normally distributed quantity. The mean $\mu_i(\Theta_{\mathcal{M}})$ is a value predicted by the model \mathcal{M} using parameters $\Theta_{\mathcal{M}}$ corresponding to \mathcal{D}_i . σ_i is the measurement error on the data point \mathcal{D}_i .

$P(\Theta_{\mathcal{M}}|\mathcal{M})$ is the prior probability (or ‘prior’) of the model parameters $\Theta_{\mathcal{M}}$ and represents the knowledge on the model parameters before taking the observational data into account.

$P(\mathcal{D}|\mathcal{M})$ is a normalization constant, which ensures that the posterior is normalized to unity and is frequently referred to as the Bayesian evidence $\mathcal{Z}_{\mathcal{M}}(\mathcal{D})$:

$$\mathcal{Z}_{\mathcal{M}}(\mathcal{D}) = P(\mathcal{D}|\mathcal{M}) = \int \mathcal{L}(\Theta_{\mathcal{M}})P(\Theta_{\mathcal{M}}|\mathcal{M})d\Theta_{\mathcal{M}}. \quad (4)$$

Additionally, the evidence $\mathcal{Z}_{\mathcal{M}}(\mathcal{D})$ enables the comparison of the performance of different models \mathcal{M}_i to each other and to decide which model best describes the observed data \mathcal{D} . We can compare two models \mathcal{M}_1 and \mathcal{M}_2 by considering the Bayes’ factor K

$$K = \frac{P(\mathcal{M}_1|\mathcal{D})}{P(\mathcal{M}_2|\mathcal{D})} = \frac{\mathcal{Z}_{\mathcal{M}_1}(\mathcal{D})}{\mathcal{Z}_{\mathcal{M}_2}(\mathcal{D})}, \quad (5)$$

where we assumed that the prior probabilities $\mathcal{P}(\mathcal{M}_i)$ for both models are the same. An approach to interpreting the value of K is via Jeffrey’s scale (Jeffreys 1998) given in Table 1.

Due to the model comparison capabilities of the evidence $\mathcal{Z}_{\mathcal{M}}(\mathcal{D})$, we choose the ‘nested sampling’ algorithm (Skilling

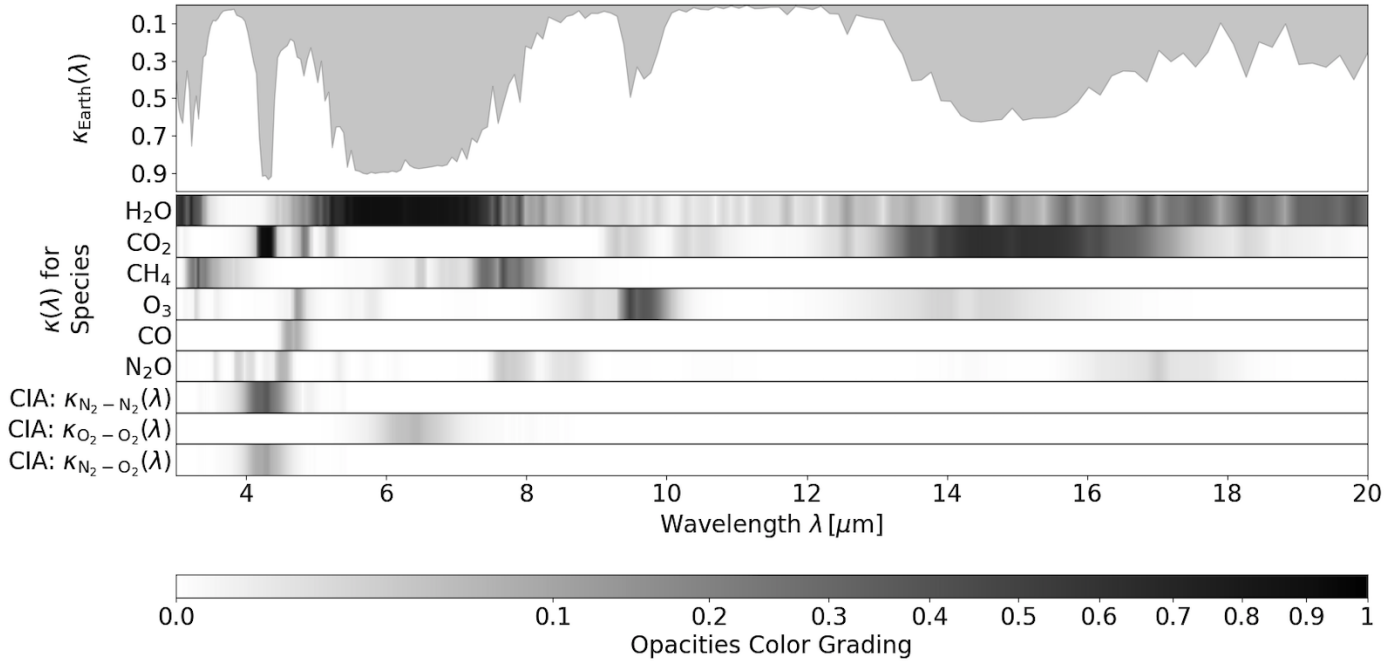


Fig. 3: *Upper panel*: The opacity of a cloudless Earth-twin atmosphere as a function of wavelength. Grey shading shows the amount of light blocked by the atmosphere. *Lower panel*: Contribution of the different molecules to the opacity of the Earth-twin atmosphere as a function of wavelength. Dark regions indicate a high opacity as is indicated by the colorbar.

Table 2: Line lists used throughout this study.

Species	Database	References
CO ₂	ExoMol	Yurchenko et al. (2020)
O ₃	HITRAN 2012	Mollière et al. (2019); Rothman et al. (2013)
CH ₄	ExoMol	Chubb et al. (2021); Yurchenko et al. (2020)
CO	HITEMP	Rothman et al. (2010)
H ₂ O	HITEMP	Rothman et al. (2010)
N ₂ O	ExoMol	Chubb et al. (2021)

2006) over MCMC algorithms, such as the Metropolis-Hastings algorithm (Hastings 1970; Metropolis et al. 1953), since it provides a direct estimate for the Bayesian evidence $\mathcal{Z}_{\mathcal{M}(\mathcal{D})}$. Furthermore, nested sampling is computationally less expensive and better at handling multimodal posterior distributions (Skilling 2006).

Specifically, we utilize the open-source `pyMultiNest` package (Buchner et al. 2014), which makes the nested sampling implementation `MultiNest` (Feroz et al. 2009) accessible to the Python language. `MultiNest` is based on the original nested sampling algorithm (Skilling 2006) and uses the ‘importance nested sampling’ algorithm (Feroz et al. 2013) to obtain more accurate estimates of the Bayesian evidence $\mathcal{Z}_{\mathcal{M}(\mathcal{D})}$.

2.3. Retrieval Setup

2.3.1. Forward Model and Noise Terms

We generate a correlated-k `petitRADTRANS` spectrum ($R = 1000$) of an Earth-twin exoplanet using the parameter values listed in Table 3 (Input column) assuming an atmosphere consisting of 100 layers. We used the line lists from

the ExoMol database (Tennyson et al. 2016) for CO₂, CH₄, and N₂O, and from the HITRAN/HITEMP database (Rothman et al. 1995, 2010) for O₃, CO, and H₂O. We summarize the reference papers corresponding to the opacity line lists in Table 2. For N₂ and O₂ we consider collision induced absorption (CIA) (as discussed in Schwieterman et al. 2015). All other atmospheric gases have distinct absorption features within the MIR range even at low abundances (see Figure 3). Furthermore, we assume constant abundances of all molecules vertically throughout the atmosphere.

We then resample the calculated MIR emission spectrum to the desired spectral resolution, keeping a constant resolution $R = \lambda/\Delta\lambda$ across the spectrum. This results in wavelength bins of variable width, where the width at short wavelengths is smaller than at long wavelengths. For the spectral resampling we use the `SpectRes` tool (Carnall 2017), which allows for time efficient resolution reduction of MIR spectra whilst keeping the overall flux and energy conserved. We then use the radius R_{pl} and the distance from Earth d_{Earth} to scale the photon flux found with `petitRADTRANS` F_{pRT} to the flux *LIFE* would detect (F_{LIFE}):

$$F_{\text{LIFE}} = F_{\text{pRT}} \frac{R_{\text{pl}}^2}{d_{\text{Earth}}^2} \quad (6)$$

Throughout this work, we define the S/N of a spectrum as the S/N calculated in the reference bin at 11.2 micron. This wavelength was chosen as it lies close to the peak flux and it does not coincide with strong absorption lines. The S/N at all other wavelengths is determined by the noise model, which relates the S/N for the reference bin to the S/N in all other wavelength bins.

For the retrieval validation we perform in Section 3, we only consider the photon noise of the planet spectrum. For the grid retrievals performed in Section 4.2, we obtain noise estimates via the `LIFESIM` tool (see Ottiger et al., *subm.*). `LIFESIM` accounts for photon noise contributions from the planet’s emission spectrum,

stellar leakage as well as local- and exo-zodiacal dust emission. In our simulations, we assume that the noise does not impact the predicted flux values, but instead only adds uncertainties to the simulated spectral points. As discussed in Feng et al. (2018), randomization of the individual spectral points based on the S/N allows to simulate accurate observational instances. At the same time, retrieval studies on such instances will result in biased results since the random placement of the small number of data points will impact the retrieval's performance. The ideal analysis would study many (≥ 10) data realizations for each considered spectrum and assess instrument performance by considering the posteriors found for these different noise instances. However, the number of cases (96) we consider and the computation time per case (≈ 1 day on 90 CPUs) make such a study computationally unfeasible (≥ 30 months of cluster time). By not randomizing the individual spectral points, we eliminate the biases introduced by noise instances. However, we are aware that this approach will likely result in optimistic results. Namely, we expect an unrealistic centering of posteriors on the truths. Additionally, for molecules at the sensitivity limit (weak spectral features), we expect overly optimistic results (see, e.g., Feng et al. 2016). In Appendix C, we perform retrievals on randomized noise instances to study these effects in more detail.

2.3.2. Priors

The assumed prior ranges for the polynomial P-T profile and the ground pressure shown in Table 3 are chosen such that a wide range of atmospheric structures (e.g., Venus or Mars atmosphere) are allowed (e.g., P_0 is considered over the range 10^{-4} to 1000 bar as indicated by $\mathcal{U}(-4, 3)$).

As demonstrated in Ottiger et al. (subm.), the detection of a planet during the search phase of the *LIFE* mission will already provide first estimates for the radius R_{pl} of the object. Specifically, for small, rocky planets within the habitable zone, the authors showed that a detection in the search phase would provide an estimate R_{est} for the true planet radius R_{true} with an accuracy of $R_{\text{est}}/R_{\text{true}} = 0.97^{\pm 0.18}$. For our simulations we therefore assume that a rough estimate of the radius is already known and we assume a Gaussian prior for this parameter (with 20% uncertainty). A constraint on R_{pl} can then be used to obtain a constraint on the planet's mass M_{pl} via a statistical mass-radius relation (see, e.g., Hatzes & Rauer 2015; Wolfgang et al. 2016; Zeng et al. 2016; Chen & Kipping 2016; Otegi et al. 2020). In our retrievals, we use Forecaster⁴ (Chen & Kipping 2016), a tool that allows us to set a prior on the planetary mass M_{pl} from the known estimate for the radius R_{pl} . The tool relies on the statistical analysis of 316 objects (Solar System objects and exoplanets), for which well-constrained mass and radius estimates are available. It produces accurate predictions for a large variety of different objects spanning from dwarf planets to late-type stars.

For the trace gases, we assume uniform priors between -15 and 0 in \log_{10} mass fraction. For the bulk constituents N_2 and O_2 we assume a uniform prior between 0 and -3 in \log_{10} mass fraction. This range gives us an increased sampling density in the high abundance regime, where we expect the sensitivity limit to be located for N_2 and O_2 . Furthermore, we use N_2 as filling gas in our atmosphere, which ensures that $\sum(\text{gas abundances}) = 1$.

3. Validation

Before running our retrieval framework for simulated *LIFE* data, we validate its accuracy and performance. For the retrieval validation, we retrieve a full resolution ($R = 1000$) Earth-twin MIR thermal emission spectrum covering the wavelength range $3 - 20 \mu\text{m}$. We generate the validation input spectrum using `petitRADTRANS` and the parameter values provided in Table 3. We only consider photon noise from the spectrum itself and chose an S/N of 50 at $11.2 \mu\text{m}$. Furthermore, we assume that the photon noise does not impact the simulated flux values, but instead only adds uncertainties to the spectral points.

In our retrievals, we run the `pyMultiNest` package using 700 live points and a sampling efficiency of 0.3 as suggested for parameter retrieval by the documentation⁵. We summarize the results in Figure 4 and Table 3 (last column).

The corner plot in Figure 4a suggests that the exoplanet's radius R_{pl} is retrieved to a very high precision with an uncertainty of roughly $0.001 R_{\oplus}$, a significant improvement over the assumed prior distribution. Similarly, the retrieved posterior for the exoplanet mass M_{pl} is more strongly constrained than the assumed prior distribution, with the standard deviation of the posterior ($0.2 \cdot \log_{10}(M_{\oplus})$) being significantly smaller than the standard deviation of the prior ($0.4 \cdot \log_{10}(M_{\oplus})$). The centering of the R_{pl} and M_{pl} posteriors on the true values and the lack of significant correlation between the two posteriors implies that the surface gravity g_{pl} is estimated accurately. The surface pressure P_0 and surface temperature T_0 are both accurately retrieved to a very high precision with an uncertainty of roughly 0.1 K for T_0 and 0.1 bar for P_0 (see Figures 4a and 4b). Further, we observe a correlation between the planetary radius R_{pl} and the surface temperature T_0 . This indicates that a higher T_0 , which results in more emission per surface area, can be compensated by a smaller R_{pl} , which results in a smaller emitting area.

From the retrieved posterior distribution of N_2 we see that our retrieval framework allows us to rule out low N_2 abundances in Earth's atmosphere via the $\text{N}_2\text{-N}_2$ CIA feature at $4 \mu\text{m}$. However, the same $\text{N}_2\text{-N}_2$ CIA feature is too weak to rule out very high N_2 abundances. In contrast, the retrieval did not manage to find evidence for O_2 in Earth's atmosphere. However, the retrieval managed to limit the O_2 abundance to maximally 0.35 in mass fraction.

The retrieved posterior distributions for the remaining molecules show a strong correlation with the M_{pl} posterior, and consequently with the surface gravity g_{pl} . This correlation is evident in the corner plot of Figure 4a since both M_{pl} and the molecular abundances of most retrieved trace gases exhibit a similarly shaped, non-gaussian posterior distribution. This is a well known physical degeneracy and has been described in other studies (see, e.g., Mollière et al. 2015; Feng et al. 2018; Madhusudan 2018; Quanz et al. 2019); it is not related to a numerical artifact. The degeneracy appears since the same spectral feature can be explained by different combinations of gravity and atmospheric composition. This degeneracy originates from the mass appearing in the form of the surface gravity in the hydrostatic equilibrium. Therein, the surface gravity is degenerate with the mean molecular weight of the atmospheric species. Since we derive the mean molecular weight from the abundances of the trace gases, this connects the planet's mass to the trace gas abundances present in its atmosphere. Further evidence for this degeneracy can be found Figure 4c. Despite the degeneracy between the re-

⁴ <https://github.com/chenjj2/forecaster>

⁵ https://johannesbuchner.github.io/PyMultiNest/pymultinest_run.html

Table 3: List of parameters used in the retrievals, their input values, prior distributions, and the validation results.

Parameter	Description	Input	Prior	Validation
$\sqrt[4]{a_4}$	P-T Parameter (Degree 4)	1.14	$\mathcal{U}(0.5, 1.8)$	$1.12^{+0.05}_{-0.04}$
a_3	P-T parameter (Degree 3)	23.12	$\mathcal{U}(0, 100)$	$22.65^{+1.74}_{-1.54}$
a_2	P-T Parameter (Degree 2)	99.70	$\mathcal{U}(0, 500)$	$98.90^{+3.72}_{-3.44}$
a_1	P-T Parameter (Degree 1)	146.63	$\mathcal{U}(0, 500)$	$146.07^{+4.75}_{-4.84}$
a_0	P-T Parameter (Degree 0)	285.22	$\mathcal{U}(0, 1000)$	$285.01^{+3.16}_{-3.08}$
$\log_{10}(P_0 [\text{bar}])$	Surface Pressure	0.006^1	$\mathcal{U}(-4, 3)$	$0.01^{+0.02}_{-0.02}$
$R_{\text{pl}} [R_{\oplus}]$	Planet Radius	1.0	$\mathcal{G}(1.0, 0.2)$	$1.00^{+0.01}_{-0.01}$
$\log_{10}(M_{\text{pl}} [M_{\oplus}])$	Planet Mass	0.0	$\mathcal{G}(0.0, 0.4)$	$-0.09^{+0.18}_{-0.22}$
$\log_{10}(\text{N}_2)$	N_2 Mass Fraction	$-0.107^{1,2}$	$\mathcal{U}(-3, 0)$	$-0.14^{+0.09}_{-0.11}$
$\log_{10}(\text{O}_2)$	O_2 Mass Fraction	$-0.679^{1,2}$	$\mathcal{U}(-3, 0)$	$-0.75^{+0.18}_{-0.17}$
$\log_{10}(\text{H}_2\text{O})$	H_2O Mass Fraction	-3.000	$\mathcal{U}(-15, 0)$	$-3.09^{+0.18}_{-0.22}$
$\log_{10}(\text{CO}_2)$	CO_2 Mass Fraction	$-3.387^{1,2}$	$\mathcal{U}(-15, 0)$	$-3.47^{+0.18}_{-0.22}$
$\log_{10}(\text{CH}_4)$	CH_4 Mass Fraction	$-5.770^{1,2}$	$\mathcal{U}(-15, 0)$	$-5.85^{+0.18}_{-0.23}$
$\log_{10}(\text{O}_3)$	O_3 Mass Fraction	-6.523^2	$\mathcal{U}(-15, 0)$	$-6.61^{+0.18}_{-0.23}$
$\log_{10}(\text{CO})$	CO Mass Fraction	-6.903^2	$\mathcal{U}(-15, 0)$	$-7.02^{+0.23}_{-0.28}$
$\log_{10}(\text{N}_2\text{O})$	N_2O Mass Fraction	-6.495^2	$\mathcal{U}(-15, 0)$	$-6.60^{+0.24}_{-0.27}$

Notes. The last column shows the output value with 1σ uncertainties for each parameter obtained in the validation run (Section 3). $\mathcal{U}(x, y)$ denotes a boxcar prior with a lower threshold x and upper threshold y ; $\mathcal{G}(\mu, \sigma)$ represents a Gaussian prior with mean μ and standard deviation σ . For a_4 we choose a prior on $\sqrt[4]{a_4}$, which allows us to sample small values more densely, typical of a 4th order coefficient, and then take the 4th power to obtain a_4 .

References. ⁽¹⁾ NASA's planet factsheet: <https://nssdc.gsfc.nasa.gov/planetary/factsheet/earthfact.html> ⁽²⁾ Table A1 in Seager et al. (2016)

trieved mass and molecule abundances, the relative difference between the input spectrum and the spectra corresponding to the retrieved parameters is small.

The posteriors of CO and N_2O are broader, roughly Gaussian, and less correlated with M_{pl} . This indicates that the constraint imposed by the retrieval framework on the abundances of these species is not solely limited by the degeneracy with M_{pl} , but also by our retrieval's sensitivity for CO and N_2O .

A method of dealing with these strong correlations is to consider relative instead of absolute abundances. This allows us to minimize the impact of systematic uncertainties that affect all retrieved trace gas abundances in the same way at the cost of losing information on the absolute abundances. Relative abundances of trace gases are of interest to us since they provide a probe to whether an atmosphere is in chemical disequilibrium, which could potentially be upheld by life. For example, we could consider the abundance of CH_4 or N_2O relative to a strongly oxidizing species such as O_2 (or O_3 , which is a photochemical product of O_2) as first suggested in Lovelock (1965) and Lippincott et al. (1967). These gases react rapidly with each other and therefore the simultaneous presence of both molecules is only possible if they are continually replenished at a high rate. On Earth, O_2 is constantly produced via photosynthesis and there is a continuous flux of CH_4 into the atmosphere due to biological methanogenesis and anthropogenic methane production. Similarly, the N_2O in Earth's atmosphere is continually replenished by a large range of microorganisms via incomplete denitrification. On Earth, these biological processes lead to CH_4 and N_2O abundances that are

many orders of magnitude larger than the chemical equilibrium. Another interesting ratio of atmospheric gases to consider is the ratio between CO and CH_4 . A large amount of CO accompanied by a lack of significant CH_4 could be interpreted as an antibiosignature as suggested in Zahnle et al. (2008). For a more exhaustive discussion of potential biosignatures we refer the reader to e.g. Schwieterman et al. (2018).

The retrieved atmospheric P-T structure is displayed in Figure 4b. Our retrieval framework extracts the P-T structure of Earth's lower atmosphere accurately to very high precision. With decreasing pressure, the uncertainty on the retrieved P-T structure increases due to a lack of signatures from the low-pressure atmospheric layers ($\lesssim 10^{-4}$ bar) in the exoplanet's thermal emission spectrum.

4. Results

In the following, we analyze the performance of the retrieval suite in characterizing an Earth-twin planet orbiting a Sun-like star at 10 pc from our Earth. We first estimate the fundamental detection limits of our retrieval suite for the trace gas abundances for different input spectra as described in Section 4.1. We then introduce the full grid of retrievals that was run in Section 4.2. The results are presented in Sections 4.3 and 4.4.

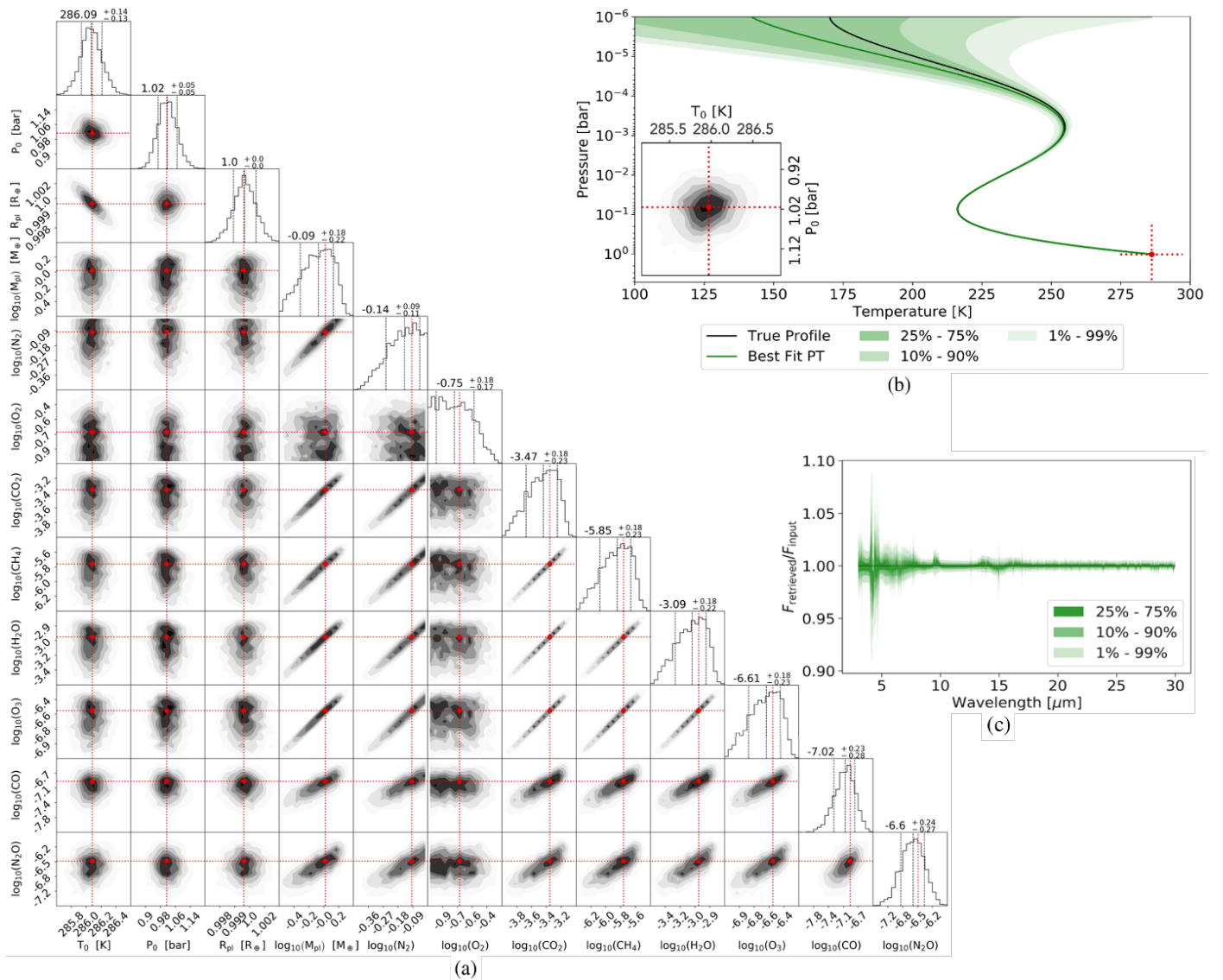


Fig. 4: Summary of the validation run outlined in Section 3. (a): Corner plot for the posterior distributions of the planetary surface temperature T_0 , surface pressure P_0 , radius R_{pl} , mass M_{pl} and retrieved abundances of different molecules. The red lines indicate the values used to generate the input spectrum. Additionally, we plot the retrieved median and the 16th and 84th percentile as dashed lines in every posterior plot. (b): Retrieved P-T profile. The shaded green regions show the uncertainties on the retrieved profile. In the bottom left corner of the P-T profile plot, we display P_0 and T_0 . The red cross marks the input values. (c): The retrieved emission spectrum $F_{retrieved}$ relative to the input emission spectrum for the retrieval F_{input} .

4.1. Detection Limit Analysis

We define the fundamental detection limits of our retrieval suite as the lowest possible molecular abundances that are retrievable for the atmospheric gases considered. For abundances below the detection limit, the corresponding spectral features are lost in the observational noise. Specifically, we estimate the detection limits of the trace gases considered in our retrievals at different values for R (20, 50, 1000), S/N (10, 20, 50), and for the largest and smallest assumed bandwidth (3 – 20 μm , 6 – 17 μm).

To do so, we generate spectra from the parameter values listed in Table 3, but set the abundance of one trace gas to 0 for each generated spectrum. We then use these spectra as retrieval input assuming only photon noise of the planet to be present and retrieve the absent trace gas. We pass all other model parameters to the retrieval as knowns.

By construction, the retrieval routine should rule out any abundance of the missing gas down to the detection limit abundance at which the spectral features can no longer be distinguished from the noise. The posterior distribution should therefore be a flat distribution (all values are equally probable) for abundances smaller than the threshold value. For values greater than the detection limit, the probability should be close to null. The threshold value can therefore be interpreted as a detection limit for the gas abundance.

The resulting posterior distribution for the trace gas can be approximated by the logistic function (a soft step function):

$$f(x) = \frac{c}{1 + e^{a \cdot x + b}}. \quad (7)$$

Here, x is the concentration of the trace gas for which the detectability is being considered. The constants a , b , and c are unique for each posterior. In Table 4, we provide the abundance

Table 4: Results obtained in the retrieval sensitivity analysis.

R	S/N	Range [μm]	$\log_{10}(\text{H}_2\text{O})$	$\log_{10}(\text{CO}_2)$	$\log_{10}(\text{O}_3)$	$\log_{10}(\text{CH}_4)$	$\log_{10}(\text{CO})$	$\log_{10}(\text{N}_2\text{O})$
20	10	3 – 20	$-6.13^{\pm 0.38}$	$-6.51^{\pm 0.33}$	$-7.22^{\pm 0.38}$	$-6.04^{\pm 0.51}$	$-4.14^{\pm 1.32}$	$-3.39^{\pm 1.23}$
		6 – 17	$-6.11^{\pm 0.54}$	$-6.61^{\pm 0.52}$	$-7.04^{\pm 0.30}$	$-5.91^{\pm 0.57}$	UC	$-3.09^{\pm 1.04}$
	20	3 – 20	$-6.68^{\pm 0.45}$	$-7.08^{\pm 0.48}$	$-7.55^{\pm 0.27}$	$-6.68^{\pm 0.53}$	$-5.28^{\pm 0.63}$	$-4.55^{\pm 1.05}$
		6 – 17	$-6.63^{\pm 0.40}$	$-7.05^{\pm 0.44}$	$-7.47^{\pm 0.37}$	$-6.67^{\pm 0.56}$	UC	$-4.30^{\pm 1.02}$
50	10	3 – 20	$-6.60^{\pm 0.49}$	$-7.08^{\pm 0.52}$	$-7.45^{\pm 0.31}$	$-6.49^{\pm 0.42}$	$-5.26^{\pm 0.67}$	$-4.33^{\pm 1.07}$
		6 – 17	$-6.47^{\pm 0.45}$	$-7.05^{\pm 0.46}$	$-7.46^{\pm 0.28}$	$-6.56^{\pm 0.55}$	UC	$-3.86^{\pm 0.98}$
	20	3 – 20	$-6.99^{\pm 0.34}$	$-7.48^{\pm 0.34}$	$-7.75^{\pm 0.22}$	$-7.09^{\pm 0.45}$	$-5.82^{\pm 0.36}$	$-5.28^{\pm 0.75}$
		6 – 17	$-6.98^{\pm 0.34}$	$-7.50^{\pm 0.41}$	$-7.84^{\pm 0.36}$	$-7.08^{\pm 0.33}$	UC	$-5.10^{\pm 0.87}$
1000	50	3 – 20	$-9.29^{\pm 0.25}$	$-9.27^{\pm 0.27}$	$-9.02^{\pm 0.27}$	$-8.81^{\pm 0.29}$	$-7.88^{\pm 0.29}$	$-8.35^{\pm 0.35}$
Terrestrial abundances:			-3.00	-3.39	-5.77	-6.52	-6.90	-6.50
<i>LIFE</i> retrieval expectation:			✓	✓	✓	~	✗	✗

Notes. All abundances are given in mass fractions in \log_{10} . We provide the threshold abundances for a detection at different R and S/N configurations, which we define as the half maximum of the retrieved soft step posterior distribution. Additionally, we provide the 16th and 84th percentile of the logistic function as denoted by the ‘ \pm ’. ‘UC’ stands for unconstrained and signifies that the retrieval does not manage to constrain the species of interest. In the last two rows, we display the assumed Earth-twin abundances and whether we expect such an abundance to be retrievable in low R and S/N cases, respectively: ‘✓’ = retrievable; ‘~’ = case dependent; ‘✗’ = not retrievable.

corresponding to the half maximum and the 16th and 84th percentile of the fitted logistic function for all tests we ran. The half maximum together with the percentiles provides an estimate for the detection limit of our retrieval suite.

The results we obtain for the R = 1000 test case (see Table 4) predict that all atmospheric trace gases should be detectable in such a retrieval setup. This is in agreement with the retrieval validation presented in Section 3.

For the cases with R \leq 50, we predict H₂O, CO₂ and O₃ to be easily detectable in an Earth-like atmosphere, since the true abundances are more than one order of magnitude larger than the retrieval’s estimated detection limit. For CH₄, the true abundance is comparable to the retrieval’s detection limit. Thus, we expect the performance for CH₄ to depend strongly on the R and S/N of the input spectrum. The true CO and N₂O abundances lie at least one order of magnitude below the estimated detection limits and are therefore irretrievable. The upper limit of CO exhibits a strong dependence on the wavelength range considered because the only CO feature in the MIR is located at $\sim 4.7 \mu\text{m}$ (see Figure 3). Excluding the wavelength range 3 – 6 μm from the analysis makes the CO abundance impossible to constrain.

This test study has provided best-case detection limits for the abundance in Earth-like atmospheres. However, retrieval of all parameters will lead to an overall increase in these detection limits. Additionally, adding additional astrophysical noise terms will also negatively impact the detection limits for the trace gases.

4.2. Retrieval Grid

We choose to consider the following grid of wavelength ranges, R values and S/N values in our final grid of retrieval studies:

- Wavelength ranges: 3 – 20 μm , 4 – 18.5 μm , and 6 – 17 μm
- Spectral resolutions: R = 20, 35, 50, and 100.
- Signal to noise ratios: S/N = 5, 10, 15, and 20 fixed at the wavelength bin centered at 11.2 μm .

The short end of the wavelength range tests, whether the CO band at $\sim 4.7 \mu\text{m}$ can be retrieved and whether including the

$\sim 3.3 \mu\text{m}$ band of CH₄ helps the detection of this molecule. At the long wavelength end the main question is how much of the extended water feature should be included in the analysis. The choice for the spectral resolution range was motivated by earlier studies (e.g., Des Marais et al. 2002).

For the reference planet we again assume the thermal emission spectrum of an Earth-twin in orbit around a G2 star located at a distance of 10 pc from Earth. We consider two different observational cases with slightly different noise properties and observational setup:

- Nominal case: (1) the *LIFE* baselines (physical distance between the four mirrors) were optimized for the detection of habitable zone planets at a wavelength of $\lambda = 15 \mu\text{m}$ (cf. Quanz et al. 2021); (2) the level of exozodiacal dust emission corresponds to 3-times the level of the local zodiacal light.
- Optimized case: (1) the *LIFE* baselines were optimized for the detection of habitable zone planets at the short wavelength end; (2) the level of exozodiacal dust emission corresponds to 0.5-times the level of the local zodiacal light⁶.

Figure 5 visualizes the difference between the nominal and the optimized S/N case by plotting the ratio between the two S/N instances. The full noise terms (including stellar leakage, local zodi and exozodi emission, and photon noise from the planet) were computed with LIFESIM (see Ottiger et al., subm.). In total, the grid comprised 96 retrieval analyses.

Figure 6 visualizes the highest (R = 100, S/N = 20) and lowest (R = 20, S/N = 5) quality input spectra for the nominal case. For every grid point specified above, we run a retrieval assuming the prior distributions listed in Table 3. Furthermore, we use the same pyMultiNest settings applied in the retrieval validation run (Section 3).

Taking the 3 – 20 μm nominal case input spectra as an example, we plot the posteriors of the planetary parameters (Figure 7),

⁶ According to the brightness distribution of exozodi disks used in recent *LIFE* detection yield estimate (Quanz et al. 2021), which is based on the results from the HOSTS survey (Ertel et al. 2020), $\lesssim 20\%$ of the disks show such low emission.

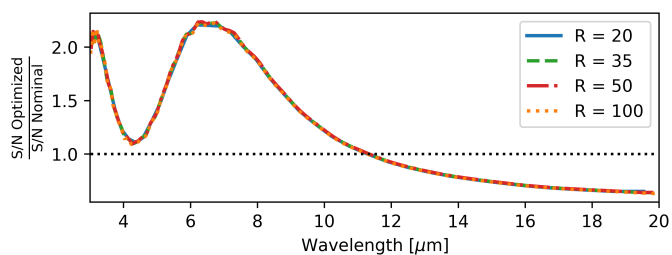


Fig. 5: Ratio between the wavelength dependant S/N of the optimized case and the nominal case. This ratio is independent of the overall S/N and the R of the Spectrum.

as well as those for the absolute (Figure 8) and the relative (Figure 9) abundances. We will use the retrieved posterior probability distributions to underline trends with respect to the wavelength range, R and S/N. For the molecular abundances, we differentiate between four different classes of posterior distributions:

- Constrained (C): The true atmospheric abundance lies above the retrieval’s detection limit. The posterior is described satisfactorily by a Gaussian. Thus, both significantly higher and lower abundances are ruled out.
- Sensitivity limit (SL): The true atmospheric abundance is comparable to the detection limit of the retrieval. We observe a distinct peak in the posterior. However, lower abundances cannot be fully ruled out. The posterior is best described by the convolution of a logistic function with a Gaussian.
- Upper Limit (UL): The true atmospheric abundance lies below the retrieval’s detection limit and could be zero. The posterior is best described by a logistic function discussed in Section 4.1. Abundances above the detection limit can be excluded, all abundances below the limit are equally likely.
- Unconstrained (UC): No information about the atmospheric abundance can be retrieved. The retrieved posterior is best described by a constant function.

For more detailed information about our posterior classification see Appendix B.

Figure 10 summarizes the type of the retrieved posterior distribution for the molecular abundances for all considered R, S/N, wavelength ranges and the two different cases. Tables containing the median as well as the 16th and 84th percentile of the retrieved posteriors for all retrieval runs are provided in the Appendix D (Tables D.1-D.6).

4.3. Retrieved Planetary Parameters

In Figure 7 we provide the retrieval results for the exoplanet parameters M_{pl} , R_{pl} , P_0 , and T_0 (3 – 20 μm input spectra in the nominal case). Our retrieval framework estimates all planetary parameters correctly.

For the planetary mass M_{pl} , the retrieved posterior is centred on the true value and roughly corresponds to the assumed prior distribution. This result indicates that our retrieval framework cannot extract further information from the input spectrum.

In contrast to M_{pl} , we manage to strongly constrain the exoplanet’s radius R_{pl} with respect to the assumed prior distribution. For all S/N ≥ 10 , we retrieve an accurate estimate for R_{pl} ($\Delta R_{\text{pl}} \leq \pm 10\%$).

For all S/N ≥ 10 , our retrievals yield strong constraints for the surface pressure P_0 . The retrieved value lies within maximally ± 0.5 dex (a factor of ≈ 3) depending on the R and S/N

combination. Similarly, the surface temperature T_0 (calculated from the retrieved P-T profile parameters and P_0) is accurately estimated by our retrieval framework for all S/N ≥ 10 . The retrieved values are centred on the correct value for most cases and the 1σ uncertainties are mostly smaller than ± 20 K.

For an S/N of 5, the retrieved parameters T_0 and P_0 exhibit significant offsets with respect to the input value. Furthermore, we find similar offsets for R_{pl} . These deviations indicate that an S/N of 5 is too low for the accurate characterization of an Earth-twin exoplanet’s atmospheric structure as we discuss further in Section 4.4. The same is true for all other wavelength ranges and both the nominal and the optimized cases considered in our work (see Appendix D).

4.4. Retrieved Abundances

The retrieved molecular abundances of the atmospheric trace gases are provided in Figure 8 (3 – 20 μm input spectra for the nominal case). Our results show the following:

- The abundances of CO_2 , H_2O and O_3 are accurately retrieved to a precision of $\leq \pm 1$ dex for all cases where the S/N is ≥ 10 .
- CH_4 only becomes retrievable for high combinations of R and S/N (for S/N = 10 at $R \geq 100$, for S/N = 15 at $R \geq 50$ and for S/N = 20 at $R \geq 35$). For other combinations of R and S/N, we only retrieve upper limits on the CH_4 abundance.
- The CO abundance is not constrained by our retrievals for any S/N ≥ 10 . At an S/N of 5 we retrieve an upper limit on the abundance of CO. This upper limit is a result of the poor overall retrieval performance in the S/N = 5 case as we will motivate below.
- We do not retrieve the N_2O abundance, but find an upper limit for the maximal possible abundance. The position of this upper limit decreases significantly with increasing R and S/N of the input spectrum.
- For all considered R and S/N combinations, the input spectra do not contain sufficient information to constrain the abundances of the bulk constituents N_2 and O_2 (not shown). We retrieve UC-type posteriors and cannot provide any constraint for N_2 and O_2 in our retrievals.
- Adding up the retrieved abundances, we find that there is at least one additional atmospheric gas that has no MIR signature probable by *LIFE* and constitutes $\approx 99\%$ of Earth’s atmospheric mass and has no significant absorption feature in the MIR. We can exclude H/He dominated atmospheres due to the small retrieved radius and CO_2 , CH_4 , or H_2O dominated atmospheres due to our retrieval results. These findings already put strong constraints on the bulk atmospheric composition.

Overall, these findings agree well with the predictions obtained in the sensitivity analysis (Section 4.1), demonstrating that the simplified assumptions used in that analysis are reasonable.

Input spectra with an S/N of 5 do not contain sufficient information to yield accurate retrieval predictions for the absolute abundances of the considered trace gases. This is in accordance with our findings for the planetary parameters. For CO_2 , H_2O and O_3 , we tend to underestimate the true atmospheric abundances. Similarly, the upper limits on the abundances of N_2O retrieved at S/N = 5 are lower than at S/N ≥ 10 and for CO we retrieve upper limits, which are no longer found at higher S/N. The underestimation of abundances at S/N = 5 is coupled with the overestimation of the surface pressure P_0 and temperature T_0 , which are again compensated by an underestimation of the radius R_{pl} . A higher P_0 leads to a higher atmospheric mass and

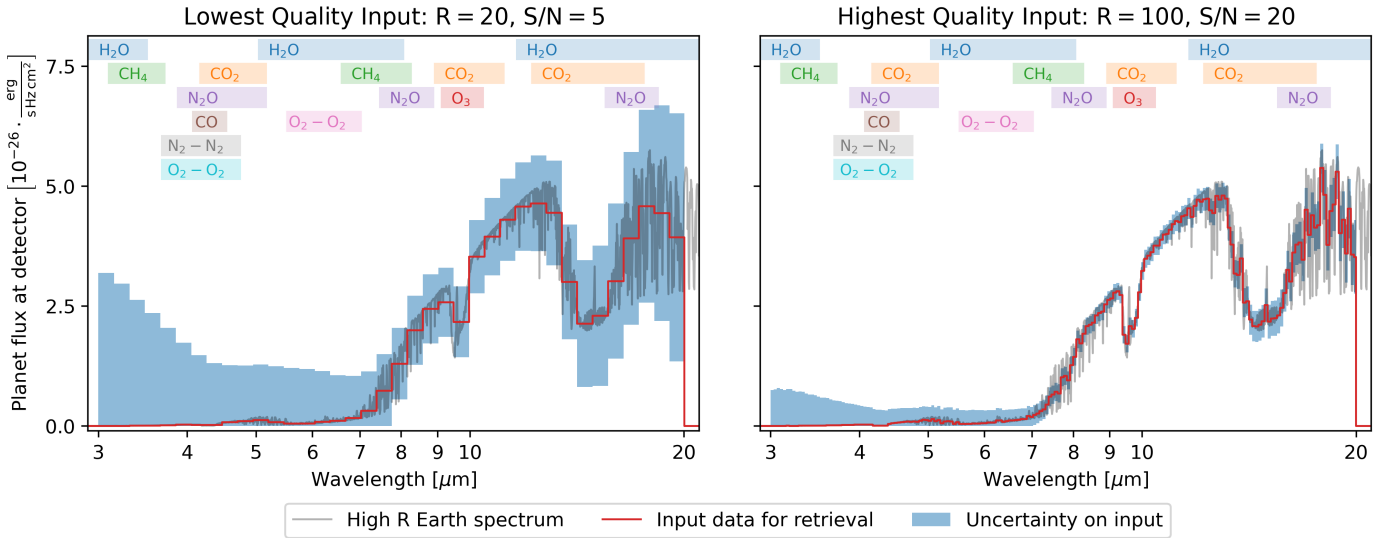


Fig. 6: Examples of input spectra used in the grid retrievals for the nominal case (left: the lowest quality input with $R = 20$, $S/N = 5$; right: the highest quality input with $R = 100$, $S/N = 20$). In gray, we provide the full resolution `petitRADTRANS` Earth spectrum. The red step function represents the wavelength-binning of the input data. Further, the blue shaded region represents the uncertainty for the corresponding bin. We also mark the absorption features of the considered atmospheric gases.

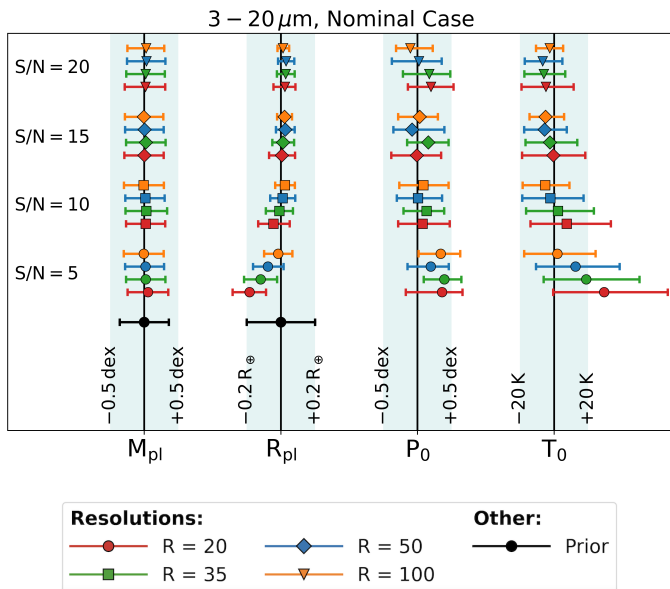


Fig. 7: Retrieved exoplanet parameters for the different grid points for the wavelength range $3 - 20 \mu\text{m}$ in the nominal case. M_{pl} is the mass, R_{pl} the radius, P_0 the surface pressure and T_0 the surface temperature of the exoplanet. The error bars denote the 68% confidence intervals. For M_{pl} and R_{pl} , we also plot the assumed prior distributions. For T_0 and P_0 , we assumed flat, broad priors. The vertical lines mark the true parameter values.

therefore to more absorbing material between the planet surface and the observer which will lead to deeper absorption features at constant molecular abundances; the same line in a MIR emission spectrum would then be produced by a smaller abundance of the atmospheric species. Hence, in this case the retrieved abundances lie below the true ones. By considering the relative abundances we can reduce these offsets (Figure 9 shows the trace gas posteriors relative to the CO_2 posterior for the nominal case,

$3 - 20 \mu\text{m}$ input spectrum). This indicates that the offsets share the same properties for all atmospheric gases, indicating that they are caused by degeneracies between parameters (pressure-abundance and gravity-abundance degeneracies). These degeneracies are larger in the small S/N and R cases since the constraints posed by the input spectrum are smaller. We further observe that the true values still lie within the posterior range (note that the plots only show the 16th, 50th, and 84th percentiles). If the degeneracies are asymmetric (e.g. lower surface pressures and temperatures are easier to exclude than high ones), this would result in the observed asymmetric positioning of the posterior distribution around the truth causing the observed offsets. The offsets diminish at higher R and S/N because the retrieval input provides stronger constraints and thus manages to reduce/break these degeneracies.

For $S/N \geq 10$, the relative abundances of H_2O , O_3 and CH_4 (if retrieved) are centred on the true values and the corresponding uncertainties are significantly smaller than for the absolute abundances ($\leq \pm 0.5 \text{ dex}$). The reduction in uncertainty is due to the elimination of the gravity-abundance degeneracy since this degeneracy affects all retrieved abundances in a comparable manner. Likewise, at $S/N = 5$, the offsets we observed for the retrieved absolute abundances are strongly diminished when considering relative abundances. This allows us to find accurate estimates for the relative abundances of CO_2 , H_2O and O_3 despite the inaccurately retrieved absolute abundances.

These findings demonstrate that considering relative abundances can significantly diminish the effects of degeneracies between trace gas abundances and other atmospheric parameters. This occurs at the cost of losing information on the absolute abundances. However, the relative abundances of trace gases can still contain vital information on planetary conditions and provide potential biosignatures (see Section 3 and, e.g., Lovelock 1965; Lippincott et al. 1967; Meadows et al. 2018).

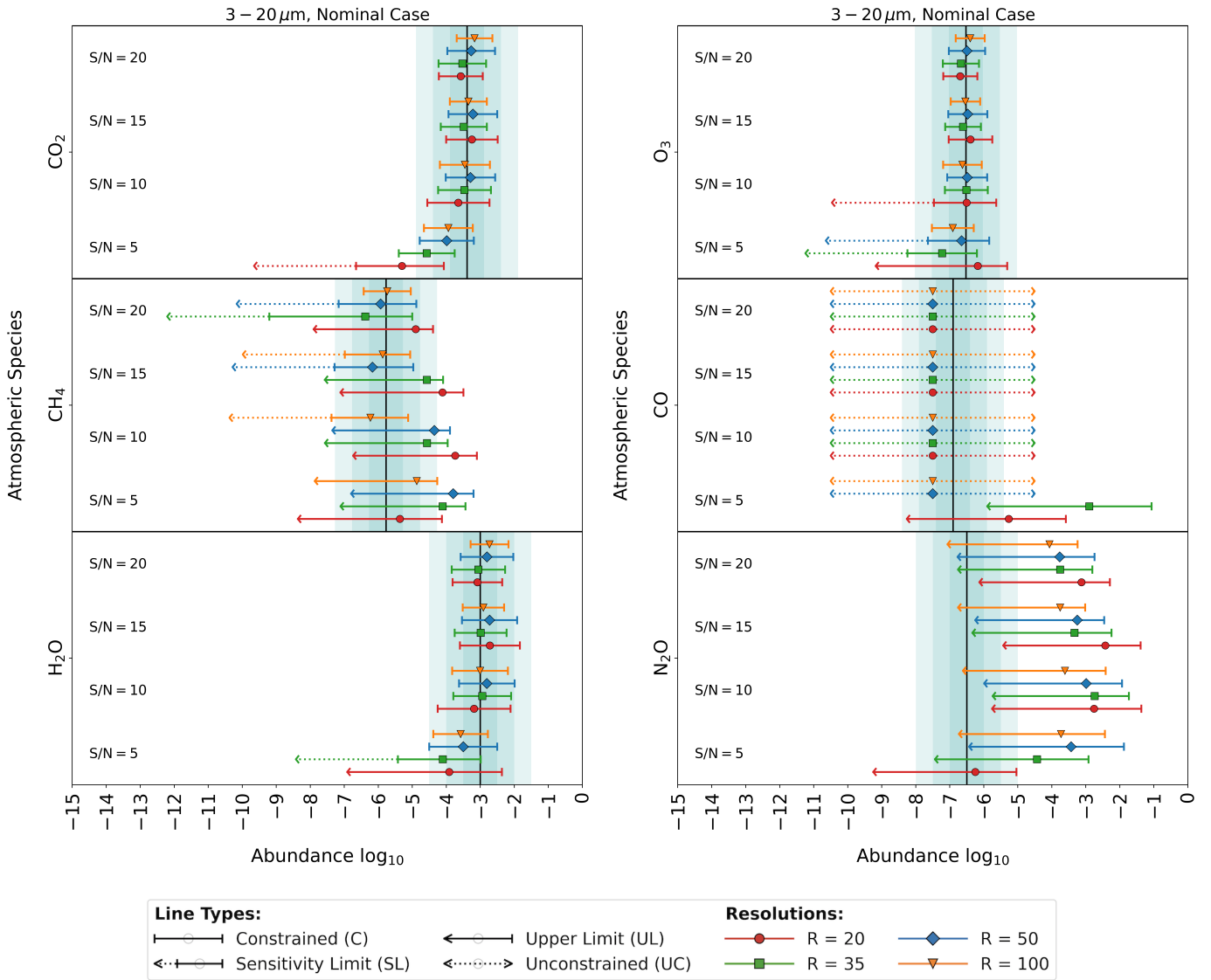


Fig. 8: Retrieved mass mixing abundances of the different trace gases present in Earth’s atmosphere for an input spectrum wavelength range of $3 - 20 \mu\text{m}$ in the nominal case. The vertical lines mark the true abundances whereas the shaded regions mark the ± 0.5 dex, ± 1.0 dex, and ± 1.5 dex regions.

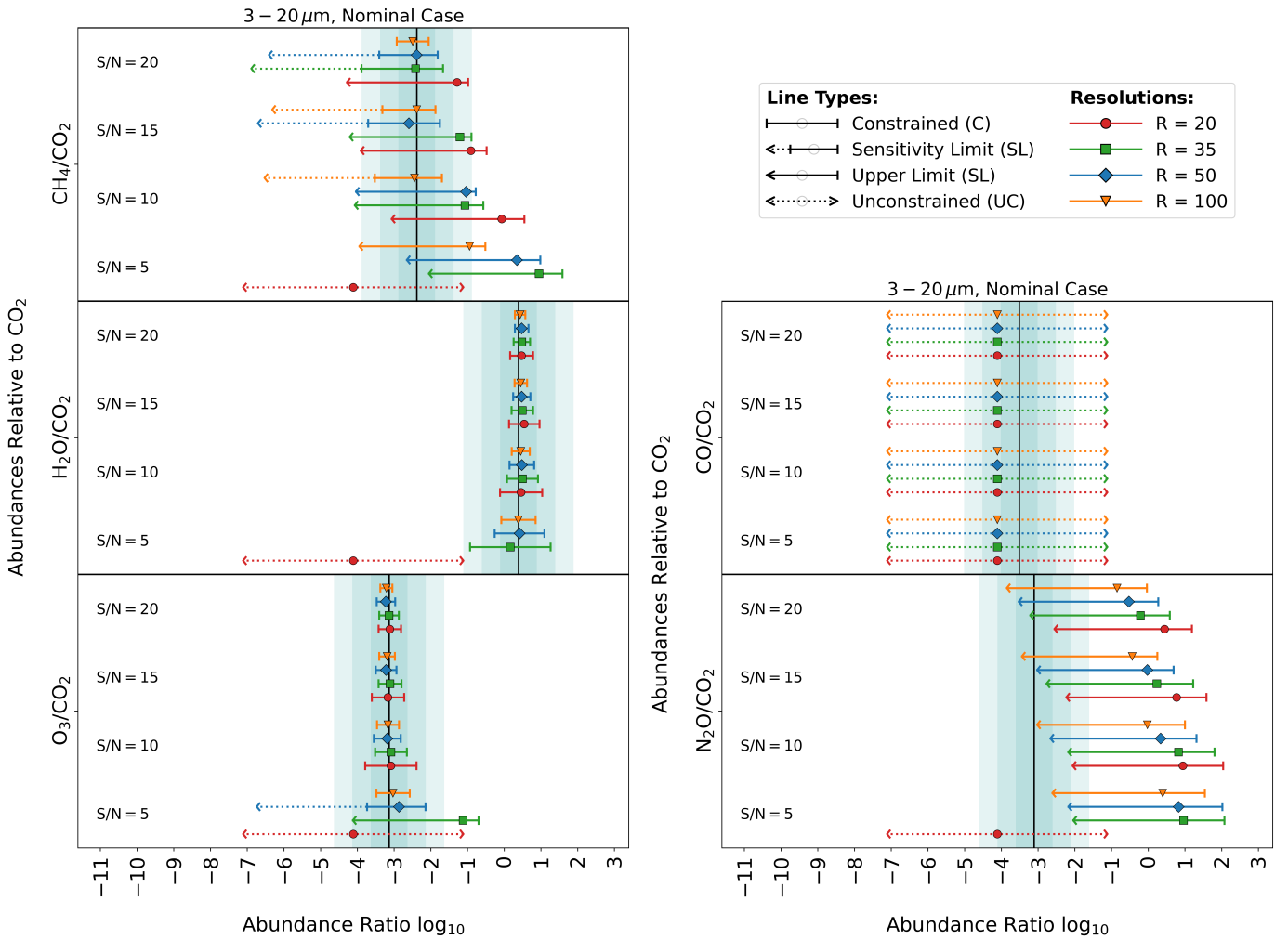
5. Discussion

After having provided an overview of the results we obtained for the nominal case (with an input spectrum covering $3 - 20 \mu\text{m}$), we now compare the retrieval results for different wavelength ranges in the nominal and optimized case. Thereby, we investigate the minimal requirements that the *LIFE* mission needs to fulfill to characterize the atmospheric structure of an Earth-twin exoplanet and detect biosignature gases in the emission spectrum. In Sections 5.1 and 5.2 we derive requirements for the wavelength range, the spectral resolution R , and the S/N . We then quantify the integration times required to reach the desired S/N for a given R and discuss the implications for the *LIFE* design in Section 5.3. In Section 5.4, we compare our work to similar retrieval studies in the literature to underline the unique scientific potential of *LIFE* for atmospheric characterization. The limitations inherent to our work and possible future investigations follow in Section 5.5.

5.1. Wavelength Range Requirement

Figure 10 provides a concise summary of the retrieved posterior types for the trace gas abundances for varying wavelength range, R and S/N for both the nominal and optimized case. We are primarily interested in large systematic differences in the overall retrieval performance between the different wavelength ranges. Small differences (e.g., in the nominal case for H_2O at $R = 35$, $S/N = 5$ or for CH_4 at $R = 35$, $S/N = 10$) are expected to disappear when averaging over multiple retrieval runs. In the following discussion we focus on the results obtained for the nominal case (first row in Figure 10).

We observe that for the trace gases CO_2 , O_3 , CO , and N_2O , considering a broader wavelength range input spectrum will result in slightly smaller uncertainties on the retrieved parameters. This is expected, since more information is passed to the retrieval framework. However, there is no significant difference in performance between the considered wavelength ranges.


 Fig. 9: As for Figure 8 but for retrieved abundances relative to CO_2 .

For the trace gases H_2O and CH_4 the $6\text{--}17\ \mu\text{m}$ case exhibits a considerably lower sensitivity than the $3\text{--}20\ \mu\text{m}$ and $4\text{--}18.5\ \mu\text{m}$ cases. An upper limit at $17\ \mu\text{m}$ excludes the strong H_2O absorption features at $> 17\ \mu\text{m}$ (see Figure 3). The H_2O lines between 8 and $17\ \mu\text{m}$ are either weak or overlap with stronger absorption features of other molecules. Therefore, at low R and S/N , these features cannot constrain the H_2O abundance satisfactorily. Below $\approx 8\ \mu\text{m}$, we observe a strong H_2O band which overlaps with the CH_4 feature at $7.7\ \mu\text{m}$. In addition, at these wavelengths the S/N in the simulated spectra decreases drastically further reducing the constraints on H_2O . Thus, when considering a wavelength range from $6\text{--}17\ \mu\text{m}$, both the H_2O and CH_4 abundance are estimated via their overlapping absorption feature at $\approx 8\ \mu\text{m}$. At low R and S/N this leads to larger uncertainties. If we consider a larger wavelength range, the long-wavelength tail of the emission spectrum provides more robust constraints on the H_2O abundance, which directly leads to an improvement for the CH_4 estimates as well. We therefore can not recommend to limit the wavelength to $6\text{--}17\ \mu\text{m}$ for *LIFE* due to its negative impact on the sensitivity for H_2O and CH_4 .

On the other hand, choosing the largest wavelength range considered in our study ($3\text{--}20\ \mu\text{m}$) provides only a negligible improvement over the $4\text{--}18.5\ \mu\text{m}$ wavelength range. From this we conclude that *LIFE* should opt for a long wavelength cut-off of at least $18.5\ \mu\text{m}$. For the short wavelength limit we suggest a value of $4\ \mu\text{m}$. This boundary would include the CO feature

at $4.67\ \mu\text{m}$, as well as the N_2 collision-induced absorption line at $4.3\ \mu\text{m}$. In the Earth-twin retrievals we present in this work, the abundances of CO and N_2 are not constrainable for any of the considered cases that include these spectral feature. However, making these spectral features accessible to *LIFE* would enable us to potentially constrain the abundances of these important molecules in non Earth-twin atmospheres. More tests to explore this idea are foreseen for future retrieval studies.

For the retrievals performed for the optimized case, we reach similar conclusions and our recommended wavelength range remains unchanged. However, the interfering effects described above are less pronounced due to an improved S/N at short wavelengths (see Figure 10 and tables in Appendix D).

5.2. R and S/N Requirements

For most trace gases, we observe no significant difference between the nominal and optimized case for all $S/N \geq 10$ as can be seen from Figure 10. For an S/N of 5 , the optimized case yields better results for the retrieved abundances. However, due to the generally poor performance at this noise level (as previously seen), an S/N of 5 is not sufficient to characterize the atmospheric structure and composition of an Earth-twin exoplanet satisfactorily.

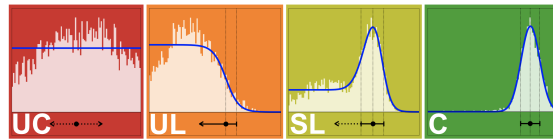
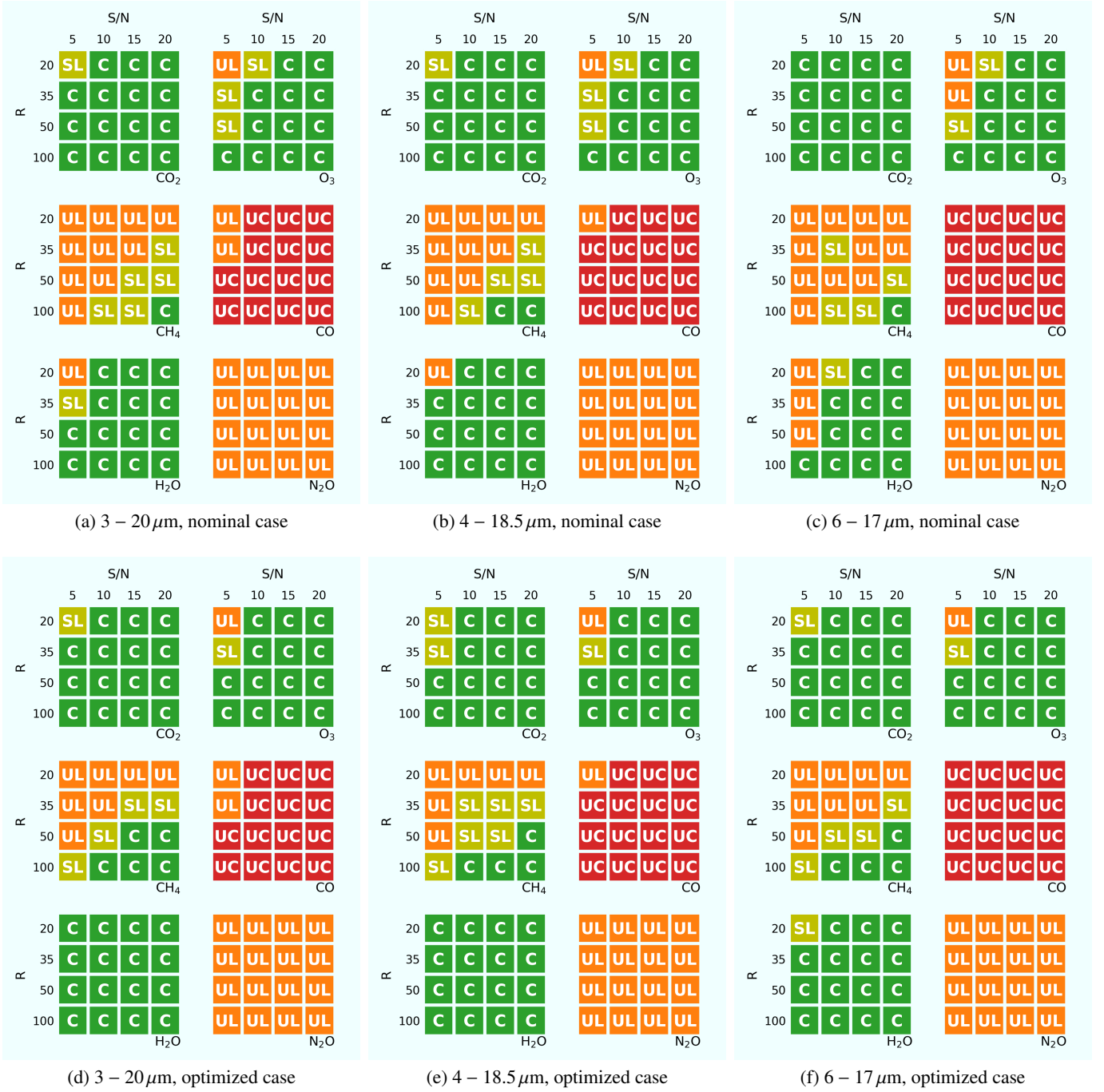


Fig. 10: Wavelength-dependent posterior types retrieved for the different trace gases in the nominal case (a)-(c) and the optimized case (d)-(f). The lowermost panel gives the colour coding for the different posterior types. The abbreviations used for the different posteriors are introduced in Section 4.2. (a),(d): 3 – 20 μm , (b),(e): 4 – 18.5 μm , (c),(f): 6 – 17 μm .

Generally, we observe that CO_2 , H_2O and O_3 are easily retrievable (within ± 1 dex) for an Earth-like atmosphere for all $\text{S/N} \geq 10$. This finding is in accordance with the results presented in Cockell et al. (2009). However, other studies suggest that for a clear O_3 detection a higher R or S/N are necessary (see, e.g., von

Paris et al. 2013; Léger et al. 2019). In contrast, CO is not recoverable for any of the considered cases due to the large astrophysical noise at short wavelengths, which indicates that detecting CO from the MIR emission spectrum of an Earth-twin exoplanet around a Sun-like star is extremely challenging and would re-

quire very high S/N and higher spectral resolution. Similarly, the N₂O abundance present in Earth’s atmosphere is too low to be detected in all cases considered. However, we retrieve upper abundance limits, which indicates that high atmospheric concentrations of N₂O ($\gtrsim 10^{-3}$) would likely be detectable.

In contrast, the retrieval results for CH₄ depend strongly on the considered R and S/N for both the nominal and optimized case (see Figure 10). Generally, our retrieval results for CH₄ improve as we consider higher R and S/N. For both baseline configurations, we retrieve a threshold above which the retrieval framework manages to accurately estimate the CH₄ abundance. This threshold manifests itself as a diagonal in the R-S/N space, which indicates that, e.g., a lower S/N can be compensated with a higher R without impacting the retrieval results significantly. The main difference is that R is intrinsic to the *LIFE* design (dependant on the spectrograph specifications), where as the S/N depends on the design (aperture size) and the integration time.

Generally, we find that in the optimized case the accuracy of the retrieval for CH₄ is improved. Firstly, *LIFE* is configured to optimize the signal at short wavelengths, which directly leads to an improvement in the S/N of the $\sim 7.7\ \mu\text{m}$ CH₄ feature. Secondly, the reduced noise contribution from exozodiacal dust also improves the S/N at short wavelengths. The resulting S/N enhancement at short wavelengths can be seen in Figure 5. These two factors lead to an increase in the retrieval’s overall performance. We observe that, in the optimized case for the 3 – 20 μm range, CH₄ is detectable (at least an SL-type posterior) in an Earth-twin atmosphere with the following combinations:

- S/N = 15 for R = 35,
- S/N = 10 for R = 50,
- S/N = 5 for R = 100.

R = 20 is too low to allow for a meaningful constraint on the CH₄ abundance for all considered cases. But if for technical reasons one would like to keep R as low as possible, we are left with R = 35 and R = 50. The higher resolution case potentially allows for the detection of a C-type posterior when going to higher S/N. In the nominal case, the S/N has to be increased to obtain comparable results at the same R (S/N = 20 for R = 35, or S/N = 15 for R = 50).

Since the detection of CH₄ depends strongly on the combination of R and S/N, it is important to evaluate the significance of the CH₄ detection in the cases R = {35, 50} and S/N = {10, 15, 20}. For every R-S/N pair, we run retrievals with and without CH₄ being included in the forward model. We then compare the log-evidences corresponding to the retrievals for both scenarios via the Bayes’ factor K . The results are summarized in Table 5.

The value of K , which corresponds to the ratio calculated from the Bayesian evidence of the model that considers CH₄ divided by the evidence of the methane-free model, is a measure of which model is better at describing the observed data (see Table 1). A positive $\log_{10}(K)$ indicates that the model including CH₄ (model evidence is denoted $\mathcal{Z}_{\text{CH}_4}$) describes the observed emission spectrum better than the model without CH₄ (model evidence is denoted $\mathcal{Z}_{-\text{CH}_4}$). In contrast, negative values favor the CH₄-free atmospheric model.

For all cases where R = 35, the Bayes’ factor $\log_{10}(K) \approx 0.0$ (within 1- σ) indicating that there is no difference between the models with and without CH₄. Therefore, despite retrieving SL-type posteriors for S/N ≥ 15 , the retrieval framework does not provide unambiguous evidence that CH₄ is indeed present in the

 Table 5: Log-evidence for retrievals with and without CH₄.

		S/N	10	15	20
Nominal Case	R = 35	$\ln(\mathcal{Z}_{\text{CH}_4})$	$-23.6^{\pm 0.2}$	$-27.0^{\pm 0.2}$	$-28.8^{\pm 0.2}$
		$\ln(\mathcal{Z}_{-\text{CH}_4})$	$-23.7^{\pm 0.2}$	$-27.2^{\pm 0.2}$	$-28.8^{\pm 0.2}$
		$\log_{10}(K)$	$0.0^{\pm 0.1}$	$0.1^{\pm 0.1}$	$0.0^{\pm 0.1}$
	R = 50	$\ln(\mathcal{Z}_{\text{CH}_4})$	$-25.1^{\pm 0.2}$	$-27.8^{\pm 0.2}$	$-29.8^{\pm 0.2}$
		$\ln(\mathcal{Z}_{-\text{CH}_4})$	$-25.4^{\pm 0.2}$	$-28.4^{\pm 0.2}$	$-30.6^{\pm 0.2}$
		$\log_{10}(K)$	$0.1^{\pm 0.1}$	$0.3^{\pm 0.1}$	$0.3^{\pm 0.1}$
Optimized Case	R = 35	$\ln(\mathcal{Z}_{\text{CH}_4})$	$-24.8^{\pm 0.2}$	$-27.9^{\pm 0.2}$	$-30.2^{\pm 0.2}$
		$\ln(\mathcal{Z}_{-\text{CH}_4})$	$-24.9^{\pm 0.2}$	$-28.2^{\pm 0.2}$	$-30.1^{\pm 0.2}$
		$\log_{10}(K)$	$0.0^{\pm 0.1}$	$0.1^{\pm 0.1}$	$0.0^{\pm 0.1}$
	R = 50	$\ln(\mathcal{Z}_{\text{CH}_4})$	$-26.7^{\pm 0.2}$	$-29.6^{\pm 0.2}$	$-31.5^{\pm 0.2}$
		$\ln(\mathcal{Z}_{-\text{CH}_4})$	$-28.8^{\pm 0.2}$	$-31.7^{\pm 0.2}$	$-35.1^{\pm 0.2}$
		$\log_{10}(K)$	$0.8^{\pm 0.1}$	$0.9^{\pm 0.1}$	$1.6^{\pm 0.1}$

Notes. With CH₄: $\ln(\mathcal{Z}_{\text{CH}_4})$; Without CH₄: $\ln(\mathcal{Z}_{-\text{CH}_4})$. The results are for input spectra covering the 3 – 20 μm wavelength range. The last row for a given R lists $\log_{10}(K)$ of the Bayes’ factor K , which we calculate via: $\log_{10}(K) = (\ln(\mathcal{Z}_{\text{CH}_4}) - \ln(\mathcal{Z}_{-\text{CH}_4})) / \ln(10)$ (derived from Eq. 5). We compare the performance of the models with and without CH₄ to each other using Jeffrey’s scale (Jeffreys 1998) (see Table 1). The ‘ \pm ’ indicates the 68% confidence interval $\log_{10}(K)$.

Table 6: Required observation time in days.

		Observation Time [days]					
		Nominal Case			Optimized Case		
R	S/N	1 m	2 m	3.5 m	1 m	2 m	3.5 m
35	15	771	74	15	922	64	9
50	10	490	47	10	589	41	6

Notes. Observation times for an Earth-twin at 10 pc for the two combinations of R and S/N discussed in Section 5.2 and three different aperture diameters (1m, 2m, and 3.5m).

observed atmosphere. This finding underlines the nature of SL-type posteriors, where the long tail towards low abundances indicates that the retrieval can do without CH₄. For R = 50, we generally observe larger $\log_{10}(K)$. In the nominal case, we find weak support for the model including CH₄. In the optimized case, we find substantial to strong evidence for the presence of CH₄ as is indicated by $0.5 < \log_{10}(K) < 2.0$.

These findings suggest that *LIFE* requires a minimal R of 50 to confidently rule out the CH₄-free atmospheric model in retrievals of Earth-twin MIR emission spectra.

5.3. Observation Time Estimates

It is crucial to derive estimates for the integration time required to reach a certain S/N. The integration time does, however, not only depend on R and S/N, but also on the aperture diameter of the *LIFE* collector spacecraft. Hence, our analyses can provide some first order requirements for the aperture size. We summarize the integration time estimates for the above-mentioned combinations of R and S/N in Table 6 and give a more exhaustive list containing observation time estimates for all retrieved input spectra in Appendix E.

We find that with $4 \times 1\text{m}$ apertures *LIFE* will not be able to characterize terrestrial exoplanet atmospheres at a distance of 10 pc because unrealistic integration times > 1 year would be required. While Bryson et al. (2021) used the results from NASA’s *Kepler* mission to estimate with 95% confidence that the nearest

terrestrial exoplanet orbiting with the habitable zone around a G or K dwarfs is only ≈ 6 pc away, they also estimate that there are only ≈ 4 such objects within 10 pc. Hence, a $4 \times 1\text{m}$ configuration will not allow us to probe a somewhat sizable sample of temperate terrestrial exoplanets.

For the other two setups ($4 \times 2\text{m}$ and $4 \times 3.5\text{m}$), the observation times are more feasible and would allow for the characterization of up to a few tens of terrestrial exoplanet atmospheres within *LIFE*'s characterization phase. Specifically, for both the nominal and optimized case, and assuming the $4 \times 2\text{m}$ setup, having $R = 50$ and $S/N = 10$ would require less time (47 days for the nominal case, 41 days for the baseline optimized case) compared to $R = 35$ and $S/N = 15$ (74 and 64 days, respectively). This again underlines that a resolution of $R = 50$ is more suitable. The saved integration time could be used to characterize the atmospheres of additional exoplanets or to measure higher S/N spectra for the most promising objects. Similar conclusions hold for the $4 \times 3.5\text{m}$ case. However, the required observation times required would be significantly smaller.

5.4. Comparison to Other Studies

In order to demonstrate the validity and understand the full implications of our retrieval results, we compare the results to previous studies in the literature. In Section 5.4.1, we compare our work to previously published work on MIR thermal emission retrievals. In Section 5.4.2, we consider findings from a comparable retrieval study for the NIR/VIS wavelength range and demonstrate the unique scientific potential of MIR observations with *LIFE*.

5.4.1. MIR Thermal Emission Studies

In the white paper by [Quanz et al. \(2018\)](#), a similar retrieval study was performed for an Earth-twin exoplanet. The study assumed $R = 100$, $S/N = 20$, covered a larger wavelength range ($3 - 30\mu\text{m}$), and considered only photon noise of the planet on the input spectrum neglecting any additional noise terms. We compare their findings to our results for the $3 - 20\mu\text{m}$ wavelength range, $R = 100$, $S/N = 20$ for the nominal case.

Our study reaches a comparable accuracy (± 0.5 dex) for the atmospheric trace gases CO_2 , H_2O , O_3 , and CH_4 . This is achieved despite our usage of the more realistic *LIFEsim* noise model, which features additional noise sources that lead to considerably larger errors especially at short wavelengths ($\lambda \lesssim 8\mu\text{m}$), where the *LIFEsim* noise is dominated by the contributions from stellar leakage. The performance of our retrieval suite is likely a result of our prior assumption for the exoplanet mass, which was not made in the [Quanz et al. \(2018\)](#) study. The width of the retrieved abundance posteriors is limited by the exoplanet's mass posterior due to the degeneracy between trace gas abundances and the surface gravity. The Gaussian prior we assumed for the exoplanet's mass limits the range of allowed masses. Thereby, also the surface gravity is constrained, limiting the range of possible abundances. We note, however, that our mass and radius prior are informed by empirical measurements.

In contrast to [Quanz et al. \(2018\)](#), we do not succeed in constraining the CO and N_2O abundances in our retrievals. Both atmospheric trace gases have their main absorption features at wavelengths $\lambda \lesssim 8\mu\text{m}$ (see Figure 3), where the observational *LIFEsim*-noise dominates over the absorption features of interest. Furthermore, the retrievals performed in [Quanz et al. \(2018\)](#) find significantly stronger constraints for the shape of the P-T

profile and the planetary parameters P_0 and T_0 . This is likely a combined result of the more heavily constrained P-T profile model and the more optimistic noise estimates they used in their retrieval analysis.

Finally, the Earth-twin's radius is retrieved to an extremely high precision in both studies. This underlines the scientific potential of observations probing the thermal emission of planets in the MIR wavelength range. Determining the radius in NIR/VIS reflected light spectra is not robust (e.g., [Feng et al. 2018](#)) due to a degeneracy between the planet's albedo and its radius (a large surface area and low albedo can lead to the same flux as a smaller area and higher albedo).

A similar study, albeit for lower resolutions ($R = 5, 20$) and a less complete noise model, has been performed by [von Paris et al. \(2013\)](#) for the former *Darwin* mission concept. They found, that at $R = 20$, a MIR nulling interferometer would be capable of constraining the surface conditions (P_0 to $\pm 0.5\text{dex}$, T_0 to $\pm 10\text{K}$) and planetary parameters (R_{pl} to $\pm 10\%$, M_{pl} to $\pm 0.3\text{dex}$) of a cloud-free exoplanet, which agrees well with the results presented here. Further, they manage to retrieve comparable constraints for the abundances of CO_2 and O_3 at 1σ confidence levels. However, they also discuss, that for a 5σ detection of CO_2 and O_3 , higher resolutions are mandatory. Similar results are presented in [Léger et al. \(2019\)](#), where resolution limit of $R = 40$ is derived for a robust detection of CO_2 , H_2O and O_3 in the atmospheres of Earth-similar planets around M- and K-Type stars.

5.4.2. NIR/VIS Reflected Light Studies

[Feng et al. \(2018\)](#) presented results for a similar retrieval study using reflected light input spectra in the wavelength range $0.4 - 1.0\mu\text{m}$. These results are similar to the findings presented in [Brandt & Spiegel \(2014\)](#). We consider their results for the $R = 70$, $S/N = \{10, 15\}$ cases and compare them with our findings for the $R = 50$, $S/N = 10$ and $R = 35$, $S/N = 15$ optimized case. In Figure 11, we show the results for all parameters of interest that are retrievable with at least one of the two approaches.

This comparison demonstrates that NIR/VIS and MIR wavelength studies yield partially complementary results. The MIR range enables us to search for signatures of the important trace gases CO_2 and CH_4 . Both these gases are not accessible through reflected NIR/VIS light observations at Earth's mixing ratios. Additionally, studying the MIR thermal emission spectra of exoplanets enables us to pose significant constraints on the important planetary parameters T_0 , P_0 and R_{pl} . These three parameters are not easily accessible via reflected light observations in the NIR/VIS wavelength range ([Quanz et al. 2018](#); [Feng et al. 2018](#); [Carrión-González et al. 2020](#)).

However, studies in the NIR/VIS wavelength range provide a direct probe for the O_2 abundance, whereas MIR observations can only probe the O_3 abundance, a photo-chemical byproduct of O_2 in our atmosphere. Additionally, the NIR/VIS wavelength range may allow us to characterize the surface composition of an exoplanet (e.g., [Brandt & Spiegel 2014](#)) via the wavelength-dependent surface scattering albedo. Such NIR/VIS observations could potentially allow for a detection of liquid surface water via the ocean glint as suggested in [Robinson et al. \(2010\)](#) or a detection of the vegetation red edge, which is an increased reflectivity in the NIR due to photosynthetic life and therefore a surface biosignature (see, e.g., [Seager et al. 2005](#); [Schwieterman 2018](#)). A planet accessible to both techniques would be a prime target for atmospheric characterization

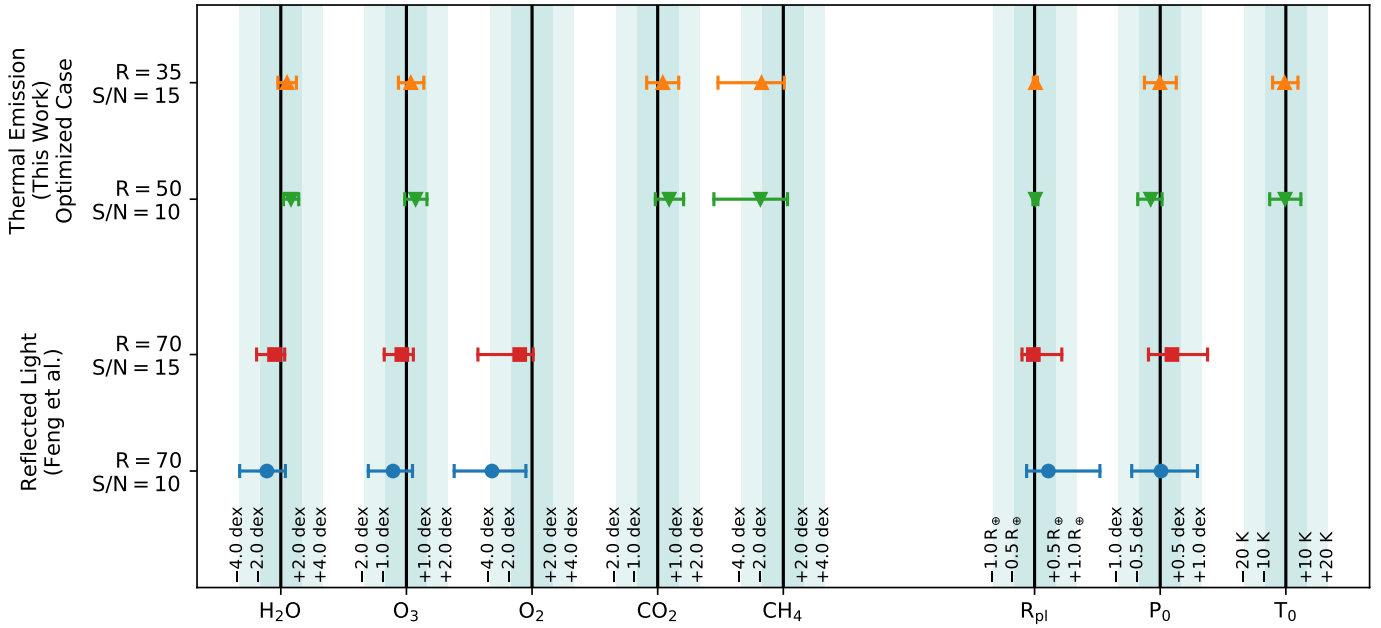


Fig. 11: Performance comparison between different retrieval studies. The error bars correspond to the 68% confidence intervals of the retrieved posterior distributions. The emitted light study from this work for ($R = 50$, $S/N = 10$ (green downward triangle) and $R = 35$, $S/N = 15$ (orange upward triangle), $3 - 20 \mu\text{m}$ in the optimized case); the reflected light study by Feng et al. (2018) ($R = 70$, $S/N = 10$ (blue dot), 15 (red square), $0.4 - 1.0 \mu\text{m}$).

5.5. Limitations and Future Work

Even though we have achieved our main goal of deriving first-order quantitative requirements for *LIFE*, the results have to be interpreted with care since there are fundamental limitations inherent to our approach:

- The input spectra for our retrievals are generated using a 1D radiative transfer model and a fully mixed atmosphere, which is a simplification of reality. Additionally, we did not account for the effect of partial, full, or varying cloud coverage on the MIR Earth-twin emission spectrum. Retrieval analyses based on more complex forward models are foreseen in the future to investigate the effects of these simplifying assumptions.
- We do not retrieve for additional molecules that are not present in the input spectrum. However, when analyzing spectra from observations, we do not know what species are present in the atmosphere. Not retrieving for additional molecules that are not present might lead to overly confident estimates for *LIFE*'s technical requirements. We provide a first test for the robustness of our results with respect to additional species in Appendix C and plan further investigations for future work.
- The input spectrum is static and represents the “average” emission spectrum of the Earth, but the real emission spectrum varies over time (day vs. night and summer vs. winter) and it also depends on the viewing geometry (pole-on vs. equator-on) (e.g., Mettler et al. 2020).
- The presence of a moon can have an influence on the integrated thermal emission spectrum of the planet-moon system, in particular if the moon is as large as the Earth's moon and features dayside temperatures higher than that of the planet (Robinson 2011). The quantitative impact a moon has on the retrieval results will be investigated in future work.
- We used `petitRADTRANS` both to generate the simulated input spectra and as atmospheric forward model for the retrieval framework. As demonstrated in Barstow et al. (2020),

retrieving the same input spectrum with different forward models can lead to inconsistencies between the retrieved parameter values due to differences in the forward models. Similar problems will likely arise when retrieving model parameters from an experimentally measured spectrum, since the forward model does not capture the full physics (and/or chemistry) of the observed atmosphere. Our results could therefore be overly-optimistic. Estimating the magnitude of this bias is the subject of future work.

- We added the `LIFESIM-noise` as uncertainty to the theoretically simulated theoretical flux without randomizing the value of the individual spectral points. This may lead to over-optimistic retrieval results, in particular for the small S/N cases. This is especially true for CH_4 , whose Earth's abundance is close to the detection limit of *LIFE*. A discussion on the potential impact of this simplification is provided in Appendix C.
- Currently, `LIFESIM` only features dominant astrophysical noise terms (Quanz et al. 2021, Ottiger et al., *subm.*). However, systematic instrumental effects will also impact the observations, even though, ideally, the instrument will only contribute to the noise, but not dominate the noise budget. Still, the required integration times should be considered a lower limit until the optical, thermal and detector designs of *LIFE* have further matured and `LIFESIM` is updated accordingly.
- Finally, the study of an Earth-twin exoplanet is clearly a simplification. The known diversity of terrestrial exoplanets demonstrates that future studies will have to look beyond the Earth-twin case and consider a wider range of worlds. In order to obtain more rigorous constraints on the requirements for *LIFE*, we will perform similar retrieval studies on a variety of different exoplanet types.

6. Summary and Conclusions

Using an atmospheric retrieval framework, we have derived the minimal requirements for the spectral resolution R , the wavelength coverage and the S/N that need to be met by a space-based MIR nulling interferometer like *LIFE* to characterize the atmospheres of Earth-twin exoplanets orbiting nearby solar-type stars.

In our atmospheric model, we describe the atmospheric P-T structure of an Earth-twin using a 4th order polynomial with surface-pressure P_0 and surface temperature T_0 . We assume constant, modern Earth abundances of N_2 , O_2 , CO_2 , H_2O , O_3 , CH_4 and N_2O throughout the vertical extent of the atmosphere; clouds are not included. We generate the thermal emission spectrum corresponding to this Earth-twin atmosphere using the 1D radiative transfer model *petitRADTRANS* (Mollière et al. 2019), assuming an exoplanet mass $M_{pl} = 1M_{\oplus}$ and a radius $R_{pl} = 1R_{\oplus}$. We used the *LIFEsim* tool (Ottiger et al., *subm.*) to estimate the wavelength-dependant observational noise (incl. noise from stellar leakage, and from local and exozodiacal dust emission) for different wavelength ranges, and combinations of R and S/N.

We created a Bayesian retrieval framework coupling *petitRADTRANS* and *pyMultiNest* (Buchner et al. 2014) (python access of the FORTRAN *MultiNest* (Feroz et al. 2009) implementation of the Nested Sampling algorithm (Skilling 2006)) to extract information about the atmospheric structure and composition of the Earth-twin exoplanet from the input spectra. These retrievals were performed considering different wavelength ranges (3 – 20 μm , 4 – 18.5 μm , 6 – 17 μm), spectral resolutions R (20, 35, 50, 100) and signal to noise ratios S/N (5, 10, 15, 20) at a wavelength of 11.2 μm (the corresponding noise at other wavelengths is derived via *LIFEsim*).

The performed retrieval analyses suggest that MIR observations with *LIFE* at an S/N ≥ 10 can robustly constrain the radius (uncertainty $\leq \pm 10\%$), surface pressure P_0 (uncertainty $\leq \pm 0.5$ dex) and surface temperature T_0 (uncertainty $\leq \pm 20$ K) of an Earth-twin exoplanet. These parameters cannot be probed accurately via reflected light observations of an Earth-twin at NIR/VIS wavelengths. Furthermore, we predict CO_2 , H_2O and O_3 to be detectable by *LIFE* (error $\leq \pm 1.0$ dex) given an input spectrum with an S/N ≥ 10 for all of the considered wavelength ranges and R . In contrast, the potential biosignature N_2O and the potential anti-biosignature CO are not detectable for any of the considered *LIFE* configurations. For N_2O we find an upper limit on the abundance, indicating that high abundances ($\gtrsim 10^{-3}$ in mass fraction) are potentially detectable in MIR observations. For CO , we do not retrieve any constraint.

Concerning the potential biosignature CH_4 , our retrieval results strongly depend on the properties of the input spectrum. If we aim to detect CH_4 at Earth-like abundances ($\approx 10^{-6}$ in mass fraction) in exoplanet atmospheres, we estimate a minimal requirement of $R = 50$ and S/N = 10. Furthermore, we observe a performance drop for CH_4 for the 6 – 17 μm wavelength range, which is a result of cutting off the H_2O absorption bands at wavelengths $\geq 17 \mu m$. Including H_2O bands at wavelengths $> 17 \mu m$ improves the accuracy of the H_2O abundance estimate which in turn helps disentangling contributions from species overlapping at shorter wavelengths. Between the 3 – 20 μm and 4 – 18.5 μm wavelength range, we do not observe significant differences in the performance of the retrieval framework. Therefore, a wavelength coverage of at least 4 – 18.5 μm is desirable.

Turning the S/N requirement into estimates for integration times and considering recent estimates for the number of temperate terrestrial exoplanets around Solar-type stars within 10

pc, we find that *LIFE* should feature at least 4x2 m apertures to be able to investigate a somewhat sizeable sample of these objects. With 4x1 m apertures the integration time to study an Earth-twin located at 10 pc will be prohibitively long (> 1 year).

By comparing our results with those obtained in similar studies focusing on reflected light observations of Earth-twin exoplanets (e.g., Feng et al. 2018), we find that both approaches complement each other. However, MIR emission spectra of terrestrial exoplanets can provide access to surface conditions and accurately constrain the radii of the objects, parameters that are challenging for reflected light observations. In addition, we have shown that MIR spectra will allow us to probe for the simultaneous presence of O_3 and CH_4 , a strong combinatory biosignature with no currently known false positives, underlining again the large and unique opportunity that MIR observations provide.

Overall, our results suggest that pursuing a concept for a space-based MIR nulling interferometer, like *LIFE*, in addition to the proposed NIR/VIS mission concepts, currently under consideration by NASA, will be a key element for the future of exoplanet characterization. In particular the combination of results from both approaches would vastly expand our knowledge about worlds outside the Solar System.

Acknowledgements. This work has been carried out within the framework of the National Centre of Competence in Research PlanetS supported by the Swiss National Science Foundation. S.P.Q. and E.A. acknowledge the financial support from the SNSF. This work benefited from the 2019 Exoplanet Summer Program in the Other Worlds Laboratory (OWL) at the University of California, Santa Cruz, a program funded by the Heising-Simons Foundation. Further, we would like to thank Michael Line for useful discussions and analyses from which the project benefited. P.M. acknowledges support from the European Research Council under the European Union’s Horizon 2020 research and innovation program under grant agreement No. 832428. J.L.G. thanks ISSI Team 464 for useful discussions.

Author contributions. BSK carried out the analyses, created the figures and wrote the bulk part of the manuscript. SPQ initiated the project. SPQ and EA guided the project and wrote part of the manuscript. All authors discussed the results and commented on the manuscript.

References

- Arney, G. N., Domagal-Goldman, S. D., & Meadows, V. S. 2018, *AsBio*, 18, 311
 Barstow, J. K., Changeat, Q., Garland, R., et al. 2020, *Monthly Notices of the Royal Astronomical Society*, 493, 4884–4909
 Barstow, J. K. & Heng, K. 2020, *SSR*, 216, 82
 Brandt, T. D. & Spiegel, D. S. 2014, *Proceedings of the National Academy of Sciences*, 111, 13278
 Bryson, S., Kunimoto, M., Kopparapu, R. K., et al. 2021, *AJ*, 161, 36
 Buchner, J., Georgakakis, A., Nandra, K., et al. 2014, *Astronomy & Astrophysics*, 564, A125
 Carnall, A. C. 2017, arXiv e-prints, arXiv:1705.05165
 Carrión-González, Ó., García Muñoz, A., Cabrera, J., et al. 2020, *A&A*, 640, A136
 Catling, D. C., Krissansen-Totton, J., Kiang, N. Y., et al. 2018, *Astrobiology*, 18, 709
 Chen, J. & Kipping, D. 2016, *ApJ*, 834, 17
 Chubb, K. L., Rocchetto, M., Yurchenko, S. N., et al. 2021, *A&A*, 646, A21
 Cockell, C., Léger, A., Fridlund, M., et al. 2009, *Astrobiology*, 9, 1, pMID: 19203238
 Deming, D., Louie, D., & Sheets, H. 2018, *PASP*, 131, 013001
 Des Marais, D. J., Harwit, M. O., Jucks, K. W., et al. 2002, *Astrobiology*, 2, 153
 Ertel, S., Defrère, D., Hinz, P., et al. 2020, *AJ*, 159, 177
 Fauchez, T. J., Turbet, M., Villanueva, G. L., et al. 2019, *ApJ*, 887, 194
 Feng, Y. K., Line, M. R., Fortney, J. J., et al. 2016, *The Astrophysical Journal*, 829, 52
 Feng, Y. K., Robinson, T. D., Fortney, J. J., et al. 2018, *AJ*, 155, 200
 Feroz, F., Hobson, M., Cameron, E., & Pettitt, A. 2013, *The Open Journal of Astrophysics*, 2
 Feroz, F., Hobson, M. P., & Bridges, M. 2009, *Monthly Notices of the Royal Astronomical Society*, 398, 1601–1614
 Fu, Q. & Liou, K. N. 1992, *Journal of the Atmospheric Sciences*, 49, 2139

- Gaudi, B. S., Seager, S., Mennesson, B., et al. 2020, arXiv e-prints, arXiv:2001.06683
- Goody, R., West, R., Chen, L., & Crisp, D. 1989, *Journal of Quantitative Spectroscopy and Radiative Transfer*, 42, 539
- Guillot, T. 2010, *Astronomy and Astrophysics*, 520, A27
- Harman, C. E. & Domagal-Goldman, S. 2018, *Biosignature False Positives*, ed. H. J. Deeg & J. A. Belmonte, 71
- Hastings, W. K. 1970, *Biometrika*, 57, 97
- Hatzes, A. P. & Rauer, H. 2015, *The Astrophysical Journal*, 810, L25
- Jeffreys, H. 1998, *The Theory of Probability*, Oxford Classic Texts in the Physical Sciences (OUP Oxford), 432–441
- Kawashima, Y. & Rugheimer, S. 2019, *The Astronomical Journal*, 157, 213
- Kitzmann, D., Patzer, A. B. C., von Paris, P., Godolt, M., & Rauer, H. 2011, *A&A*, 531, A62
- Komacek, T. D., Fauchez, T. J., Wolf, E. T., & Abbot, D. S. 2020, *ApJ*, 888, L20
- Lacis, A. A. & Oinas, V. 1991, *Journal of Geophysical Research: Atmospheres*, 96, 9027
- Lavvas, P., Koskinen, T., Steinrueck, M. E., Muñoz, A. G., & Showman, A. P. 2019, *ApJ*, 878, 118
- Lederberg, J. 1965, *Nature*, 207, 9
- Léger, A., Defrère, D., García Muñoz, A., et al. 2019, *Astrobiology*, 19, 797
- Léger, A., Mariotti, J. M., Mennesson, B., et al. 1996, *Icarus*, 123, 249
- Line, M., Quanz, S. P., Schwieterman, E. W., et al. 2019, *BAAS*, 51, 271
- Lippincott, E. R., Eck, R. V., Dayhoff, M. O., & Sagan, C. 1967, *The Astrophysical Journal*, 147, 753
- Lovelock, J. E. 1965, *Nature*, 207, 568
- Madhusudhan, N. 2018, *Handbook of Exoplanets*, 2153–2182
- Madhusudhan, N. & Seager, S. 2009, *ApJ*, 707, 24
- Mayor, M. & Queloz, D. 1995, *Nature*, 378, 355
- Meadows, V. S., Reinhard, C. T., Arney, G. N., et al. 2018, *Astrobiology*, 18, 630, pMID: 29746149
- Metropolis, N., Rosenbluth, A. W., Rosenbluth, M. N., Teller, A. H., & Teller, E. 1953, *The Journal of Chemical Physics*, 21, 1087
- Mettler, J.-N., Quanz, S. P., & Helled, R. 2020, *AJ*, 160, 246
- Mollière, P., Stolker, T., Lacour, S., et al. 2020, *A&A*, 640, A131
- Mollière, P., Wardenier, J. P., van Boekel, R., et al. 2019, *A&A*, 627, A67
- Mollière, P., Boekel, R. v., Dullemond, C., Henning, T., & Mordasini, C. 2015, *ApJ*, 813, 47
- Mueller-Wodarg, I. C. F., Strobel, D. F., Moses, J. I., et al. 2008, *Neutral Atmospheres*, ed. A. F. Nagy, A. Balogh, T. E. Cravens, M. Mendillo, & I. Mueller-Wodarg (New York, NY: Springer New York), 191–234
- Otegi, J. F., Bouchy, F., & Helled, R. 2020, *A&A*, 634, A43
- Peterson, B. M., Fischer, D., & LUVVOIR Science and Technology Definition Team. 2017, in *American Astronomical Society Meeting Abstracts*, Vol. 229, American Astronomical Society Meeting Abstracts #229, 405.04
- Quanz, S. P., Absil, O., Angerhausen, D., et al. 2019, arXiv e-prints, arXiv:1908.01316
- Quanz, S. P., Kammerer, J., Defrère, D., et al. 2018, in *Society of Photo-Optical Instrumentation Engineers (SPIE) Conference Series*, Vol. 10701, Proceedings of the SPIE, 107011I
- Quanz, S. P., Ottiger, M., Fontanet, E., et al. 2021, arXiv e-prints, arXiv:2101.07500
- Robinson, T. D. 2011, *ApJ*, 741, 51
- Robinson, T. D., Meadows, V. S., & Crisp, D. 2010, *ApJ*, 721, L67
- Rothman, L., Gordon, I., Barber, R., et al. 2010, *Journal of Quantitative Spectroscopy and Radiative Transfer*, 111, 2139, xVIth Symposium on High Resolution Molecular Spectroscopy (HighRes-2009)
- Rothman, L. S., Gordon, I. E., Babikov, Y., et al. 2013, *J. Quant. Spectr. Rad. Transf.*, 130, 4
- Rothman, L. S., Wattson, R. B., Gamache, R., Schroeder, J. W., & McCann, A. 1995, in *Atmospheric Propagation and Remote Sensing IV*, ed. J. C. Dainty, Vol. 2471, International Society for Optics and Photonics (SPIE), 105 – 111
- Rugheimer, S., Kaltenegger, L., Zsom, A., Segura, A., & Sasselov, D. 2013, *Astrobiology*, 13, 251
- Rugheimer, S., Segura, A., Kaltenegger, L., & Sasselov, D. 2015, *The Astrophysical Journal*, 806, 137
- Schwieterman, E. W. 2018, *Handbook of Exoplanets*, 3173–3201
- Schwieterman, E. W., Kiang, N. Y., Parenteau, M. N., et al. 2018, *Astrobiology*, 18, 663
- Schwieterman, E. W., Robinson, T. D., Meadows, V. S., Misra, A., & Domagal-Goldman, S. 2015, *ApJ*, 810, 57
- Seager, S., Bains, W., & Petkowski, J. 2016, *Astrobiology*, 16, 465, pMID: 27096351
- Seager, S., Turner, E., Schafer, J., & Ford, E. 2005, *Astrobiology*, 5, 372–390
- Selsis, F., Despois, D., & Parisot, J. P. 2002, *A&A*, 388, 985
- Sing, D. K., Fortney, J. J., Nikolov, N., et al. 2016, *Nature*, 529, 59
- Skilling, J. 2006, *Bayesian Anal.*, 1, 833
- Tennyson, J., Yurchenko, S. N., Al-Refaie, A. F., et al. 2016, *Journal of Molecular Spectroscopy*, 327, 73, new Visions of Spectroscopic Databases, Volume II
- Trotta, R. 2017, *Bayesian Methods in Cosmology*
- van de Schoot, R., Depaoli, S., King, R., et al. 2021, *Nature Reviews Methods Primers*, 1, 3
- von Paris, P., Hedelt, P., Selsis, F., Schreier, F., & Trautmann, T. 2013, *A&A*, 551, A120
- von Paris, P., Hedelt, P., Selsis, F., Schreier, F., & Trautmann, T. 2013, *Astronomy & Astrophysics*, 551, A120
- Wolfgang, A., Rogers, L. A., & Ford, E. B. 2016, *The Astrophysical Journal*, 825, 19
- Wunderlich, F., Scheucher, M., Grenfell, J. L., et al. 2021, *A&A*, 647, A48
- Yurchenko, S. N., Mellor, T. M., Freedman, R. S., & Tennyson, J. 2020, *Monthly Notices of the Royal Astronomical Society*, 496, 5282
- Zahnle, K., Haberle, R. M., Catling, D. C., & Kasting, J. F. 2008, *Journal of Geophysical Research: Planets*, 113
- Zeng, L., Sasselov, D. D., & Jacobsen, S. B. 2016, *The Astrophysical Journal*, 819, 127

Appendix A: Selection of P-T Profile Model

In the following, we analyze the performance of different parametric models in describing the atmospheric P-T structure of different terrestrial planets in our Solar System and assess their applicability in our retrieval framework.

Appendix A.1: Considered P-T Models

For our P-T model selection we consider the following four P-T models:

- Polynomial P-T parametrization: The P-T structure of an atmosphere is modelled via a n^{th} order polynomial:

$$T(P) = \sum_{i=0}^n a_i P^i \quad (\text{A.1})$$

The $n + 1$ constants a_i are the model parameters. In our P-T model selection we consider polynomials up to order $n = 9$.

- P-T parametrization proposed by [Madhusudhan & Seager \(2009\)](#): This is a P-T model for terrestrial planets. It is based on the P-T profiles of atmospheres of rocky Solar System objects and 1D self-consistent exoplanet P-T profiles generated via model atmosphere calculations. It is defined by the following equations:

$$P_0 < P < P_1 : \quad P = P_0 e^{\alpha_1 (T - T_0)^{\beta_1}} \quad (\text{A.2})$$

$$P_1 < P < P_3 : \quad P = P_2 e^{\alpha_2 (T - T_2)^{\beta_2}} \quad (\text{A.3})$$

$$P > P_3 : \quad T = T_3. \quad (\text{A.4})$$

The middle pressure layer (Eq. A.3) allows for thermal inversion, the deepest layer (Eq. A.4) is set to be isothermal due to its large optical depth. Parameters β_1 and β_2 are set to 0.5. P_0 is the pressure at the top of the atmosphere, which we fix to 10^{-6} bars. The remaining tunable parameters are: T_0 , α_1 , α_2 , P_1 , P_2 , P_3 , T_2 and T_3 . By requiring continuity between the three layers, the number of model parameters can be reduced to six by setting:

$$T_3 = T_2 + \left(\frac{\log(P_3/P_2)}{\alpha_2} \right)^2 \quad (\text{A.5})$$

$$T_2 = T_0 + \left(\frac{\log(P_1/P_0)}{\alpha_1} \right)^2 - \left(\frac{\log(P_3/P_2)}{\alpha_2} \right)^2. \quad (\text{A.6})$$

- P-T parametrization proposed by [Guillot \(2010\)](#): This model calculates the P-T structure of an atmosphere assuming a radiative equilibrium for each atmospheric layer. The model is described by the following equation:

$$T_{\text{Guillot}}(P) = \frac{3T_{\text{int}}^4}{4} \left(\frac{2}{3} + \frac{\kappa_{\text{IR}}}{g_{\text{pl}}} P \right) + \frac{3T_{\text{equ}}^4}{4} \left[\frac{2}{3} + \frac{1}{\gamma \sqrt{3}} + \left(\frac{\gamma}{\sqrt{3}} - \frac{1}{\gamma \sqrt{3}} \right) e^{-\gamma \sqrt{3} \frac{\kappa_{\text{IR}}}{g_{\text{pl}}} P} \right]. \quad (\text{A.7})$$

The factor $(\kappa_{\text{IR}} P / g_{\text{pl}})$ is the atmosphere's optical depth τ . The model assumes that the IR opacity can be approximated by a constant κ_{IR} . Further, the opacity in the visible, κ_{VIS} , is assumed to be constant and linked to κ_{IR} via γ : $\kappa_{\text{VIS}} = \gamma \kappa_{\text{IR}}$.

Table A.1: Priors used in the P-T profile retrievals.

Model	Model Parameter	Prior
Polynomial	a_i	$\mathcal{U}(-1000, 1000)$
Madhusudhan & Seager	$\log_{10}(P_i)$	$\mathcal{U}(-10, 4)$
	T_0	$\mathcal{U}(0, 1000)$
	α_1, α_2	$\mathcal{U}(0, 100)$
Guillot	$T_{\text{equ}}, T_{\text{int}}$	$\mathcal{U}(0, 1000)$
	κ_{IR}	$\mathcal{U}(0, 1)$
	γ	$\mathcal{U}(0, 100)$
Addition for Modified Guillot	$\log_{10}(P_{\text{Trans}})$	$\mathcal{U}(-10, 4)$
	α	$\mathcal{U}(-1, 1)$

Notes. $\mathcal{U}(x, y)$: boxcar prior with lower limit x and upper limit y .

g_{pl} is the planet's surface gravity; T_{int} the planet's internal temperature (remaining heat from planet's gravitational collapse or energy from radioactive decay of elements). T_{equ} is the planet's equilibrium temperature, which is the temperature the planet would have, if it were a black-body heated only by the radiation coming from its host star:

$$T_{\text{equ}} = T_* \sqrt{\frac{R_*}{2d}} (1 - A_B)^{1/4}. \quad (\text{A.8})$$

T_* is the host star's effective temperature, R_* its radius, d the separation between the planet and its host and A_B the planet's Bond albedo.

Overall, the [Guillot \(2010\)](#) P-T model requires four model parameters (T_{int} , T_{equ} , κ_{IR} and γ ; g_{pl} is already a parameter of the retrieval).

- P-T parametrization proposed by [Mollière et al. \(2019\)](#): The [Guillot \(2010\)](#) model does not allow for a non-isothermal structure in the upper atmosphere. The small modification proposed by [Mollière et al. \(2019\)](#) allows for a non-isothermal upper atmosphere:

$$T(P) = T_{\text{Guillot}}(P) \cdot \left(1 - \frac{\alpha}{1 + P/P_{\text{Trans}}} \right) \quad (\text{A.9})$$

$T_{\text{Guillot}}(P)$ is the [Guillot \(2010\)](#) P-T model (Eq. (A.7)). This modification adds two parameters, α and P_{Trans} , to the [Guillot \(2010\)](#) model, resulting in six model parameters.

Appendix A.2: Choice of P-T Model via Retrievals

We use a Bayesian retrieval framework to assess the performance of the different P-T models in describing the P-T structure of the Solar System planets Venus, Earth and Mars. We include Venus and Mars to prevent the selected P-T model from being biased towards Earth-like P-T profiles. In the retrievals, the P-T models introduced in Appendix A.1 are used as forward models. Further, we use the MultiNest algorithm ([Feroz et al. 2009](#)) for parameter estimation, via pyMultiNest ([Buchner et al. 2014](#)). We use 400 live points and a sampling efficiency of 0.8 as suggested for model comparison by the pyMultiNest documentation. The prior distributions assumed for the different model parameters are summarized in Table A.1. The P-T model we choose should provide an optimal combination of the following properties:

- Maximal model evidence \mathcal{Z}_M : A large \mathcal{Z}_M implies a good fit of the P-T model (see Section 2.2).

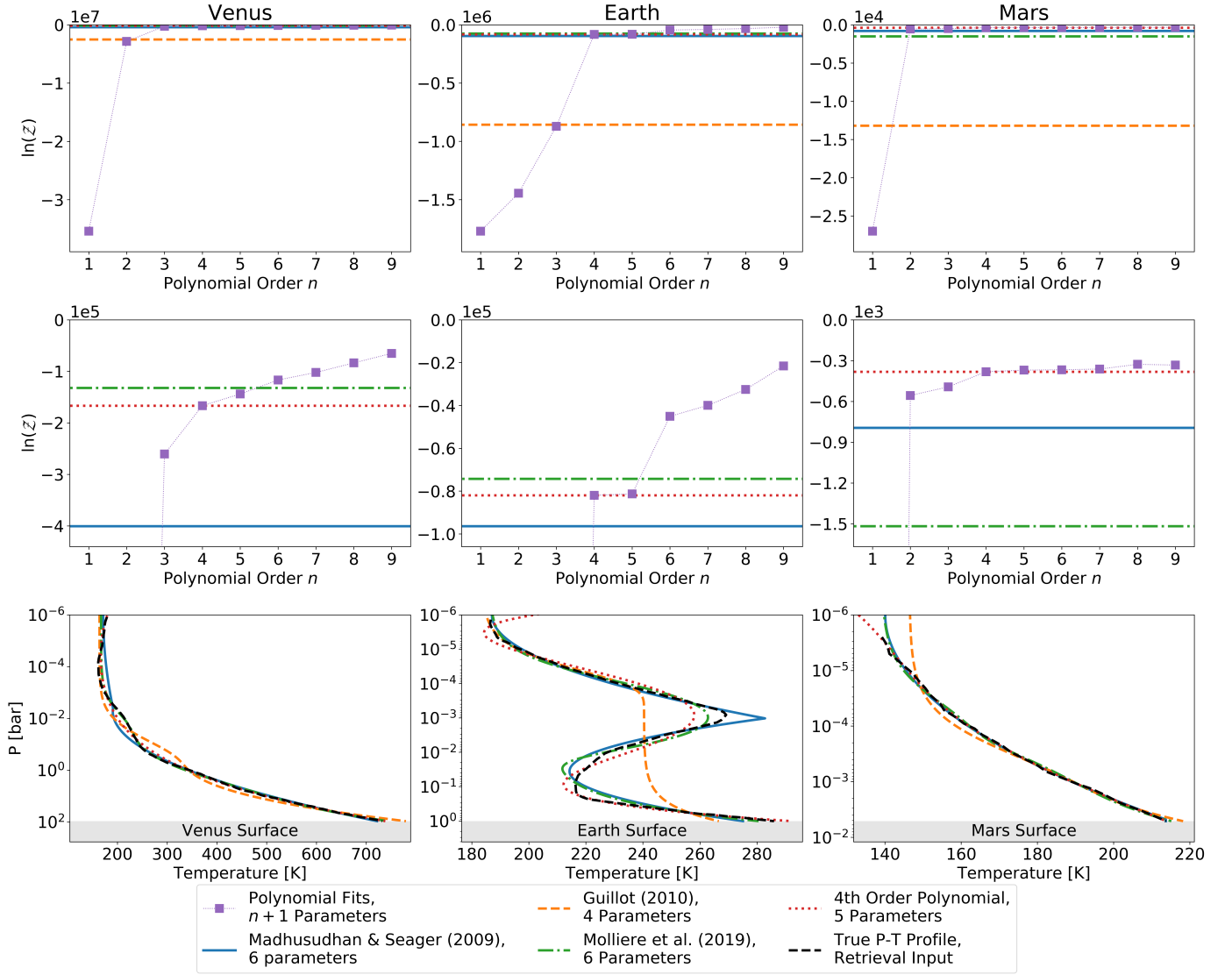


Fig. A.1: Results from the P-T model retrievals. The first row displays the log-evidence $\ln(\mathcal{Z})$ of the different models. The second row shows a zoomed in view of the high log-evidence region of the first row to allow for better comparison. The bottom row displays the retrieved best fit P-T profiles for the 4th order polynomial, the [Madhusudhan & Seager \(2009\)](#) model and the two [Guillot \(2010\)](#) models ([Guillot 2010](#); [Mollière et al. 2019](#)). The data for the true P-T profiles is taken from Figure 1 in [Mueller-Wodarg et al. \(2008\)](#).

- Minimal parameter number: Since additional model parameters increase the computational cost significantly, we aim to keep the parameter number as low as possible.

In the first two rows of Figure A.1, we plot the log-evidence $\ln(\mathcal{Z})$ corresponding to the retrieval results for the considered polynomial P-T models. Additionally, we indicate the $\ln(\mathcal{Z})$ corresponding to the non-polynomial P-T models as horizontal lines. For all considered atmospheres, we observe a continuous increase in $\ln(\mathcal{Z})$ with rising order of the polynomial P-T model. This indicates that higher-order polynomials provide a better fit to the atmosphere’s P-T profile. However, we observe a distinct flattening in the increase of $\ln(\mathcal{Z})$ with increasing polynomial order for considered atmospheres. This flattening occurs at a 3rd order polynomial for Venus, a 4th order polynomial for Earth and a 2nd order polynomial for Mars. Increasing the polynomial order beyond these thresholds does not lead to a significant improvement in the polynomial fit.

The last row in Figure A.1 indicates that the [Guillot \(2010\)](#) model fails fit the inversion in Earth’s P-T profile. This further manifests itself in the corresponding $\ln(\mathcal{Z})$, which is an order of magnitude smaller than the $\ln(\mathcal{Z})$ associated with most of the other models considered (order ≥ 4 for the polynomial model).

The [Madhusudhan & Seager \(2009\)](#) profile accurately models the P-T structure of all considered atmospheres. However, when comparing $\ln(\mathcal{Z})$ to the other models via the Bayes’ factor, we find that for Venus and Earth $\log_{10}(K)$ exceeds 2. This suggests that both polynomials of order ≥ 4 and the [Mollière et al. \(2019\)](#) model provide a significantly better P-T fit (see Table 1). For the Martian atmosphere, the [Madhusudhan & Seager \(2009\)](#) outperforms the [Mollière et al. \(2019\)](#) model, but still underperforms compared to all polynomials of order ≥ 2 .

The [Mollière et al. \(2019\)](#) accurately fits all three considered P-T structures. For Venus and Earth, the model provides a better fit than all polynomials of order ≤ 6 . However, compared to the 4th order polynomial, one additional parameter is required. For Earth, the main difference between the [Mollière et al. \(2019\)](#)

model and the 4th polynomial occurs at the inversions at 10^{-1} and 10^{-3} bar, where both models struggle to describe the true P-T structure accurately. For Mars, all polynomials of order ≥ 2 outperform the modified Guillot model, as is indicated by the significantly larger $\ln(\mathcal{Z})$.

For our purposes, we choose the 4th order polynomial P-T model, since it adds less parameters to our retrievals. Despite relying on less parameter, it manages to yield a comparable fit and describes all three considered P-T structures satisfactorily. The saved parameter allows us to retrieve for one additional atmospheric parameter of interest.

Appendix B: Posterior Classification

For the presentation of the grid retrieval results, we chose to classify the retrieved posterior distributions for the different parameters into four main classes based on their visual appearance. Figure B.1 gives illustrative examples for each of the four different posterior shapes. We define:

- Unconstrained Posterior (UC): The retrieved posterior distribution does not pose a strong constraint on the parameter of interest for the assumed prior distribution. In this case, we describe the posterior distribution as a constant throughout the entire prior range (Figure B.1a).
- Upper Limit Posterior (UL): The retrieval yields the detection (upper) limit for the retrieved parameter. For the abundance of a molecule, this implies that the retrieval rules out any concentration above the found threshold value. Below this threshold, all abundances are equally likely and cannot be ruled out. We describe such a posterior via the Logistic function:

$$f(x) = \frac{c}{1 + e^{a \cdot x + b}}. \quad (\text{B.1})$$

The constants a , b , and c are unique for each posterior. In the data analysis, we mark the half-maximum as well as the 16th percentile of the logistic function (Figure B.1b).

- Sensitivity Limit Posterior (SL): Similar to a UL posterior, the retrieval is capable of excluding the high but not the low molecular abundances. However, the posterior also shows a distinct peak at the boundary between these two regimes, which roughly corresponds to the true abundance. We convolute the Logistic function (Eq. (B.1)) with a Gaussian distribution to describe this posterior type:

$$f(x) = \frac{c + d \cdot e^{-(x+\mu)^2/\sigma^2} / (\sqrt{2\pi}\sigma)}{1 + e^{a \cdot x + b}}. \quad (\text{B.2})$$

The constants a , b , c , d , μ and σ are unique for each posterior. μ corresponds to the mean, σ to the standard deviation of the Gaussian. In our analysis, we mark the maximum value of the distribution and the position of the half maximum to the left and the right of it (Figure B.1c).

- Constrained Posterior (C): Such a posterior distribution strongly constrains the prior range and can be approximated via a Gaussian distribution:

$$f(x) = \frac{d \cdot e^{-(x+\mu)^2/\sigma^2}}{\sqrt{2\pi}\sigma}. \quad (\text{B.3})$$

The constants d , μ and σ are unique for each posterior. μ corresponds to the mean and σ to the standard deviation of the Gaussian. In the analysis we mark the 50th, 16th and 84th percentile which corresponds to the 1σ range (Figure B.1d).

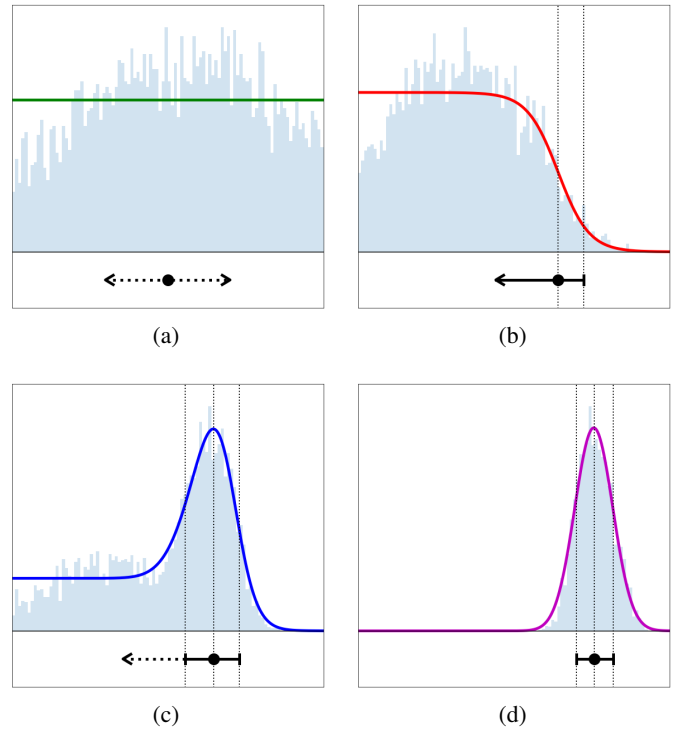


Fig. B.1: Classifications used for the retrieved posterior distributions. The histogram gives the posterior distribution as found by the retrieval framework. The colored lines represent the best fit model for the posterior distribution, the black symbols below show how such a posterior will be represented in our data analysis plots. (a): unconstrained posterior (UC), (b): upper limit posterior (UL), (c): sensitivity limit posterior (SL), (d): constrained posterior (C).

We determine the best fit model for each of the retrieved posterior distributions by fitting all four models. Thereafter, we use the log-likelihood function (Eq. (3), Section 2.2) to determine which model best describes the retrieved posterior distribution. For the SL case, we require the maximum value of the fitted function to be at least 1.3 times and maximally 10 times larger than the continuum probability at low abundances. If the peak probability is less than 1.3 times the continuum value, we assume an UL model for the posterior. If the peak abundance is at least 10 times more probable than the low abundance continuum, we choose a C-type posterior distribution. These cutoff-values are chosen empirically to match what we would obtain in a manual classification.

Appendix C: Impact of Randomized Noise and Additional Species on Retrieval Results

As discussed in Section 2.3.1, we rely on two major assumptions in order to render our retrieval study computationally feasible and bias-free. Firstly, we did not randomize the placement of the individual spectral points. Instead, we ran retrievals for the non-randomized spectral points and treated the LIFE_{SM} noise as uncertainty on the spectrum. Secondly, our retrieval model did not allow for any additional gas species in the atmosphere. However, in real observations, we will not know what species are present. Therefore, it is important to investigate how robust these retrievals are with respect to false positive detections of

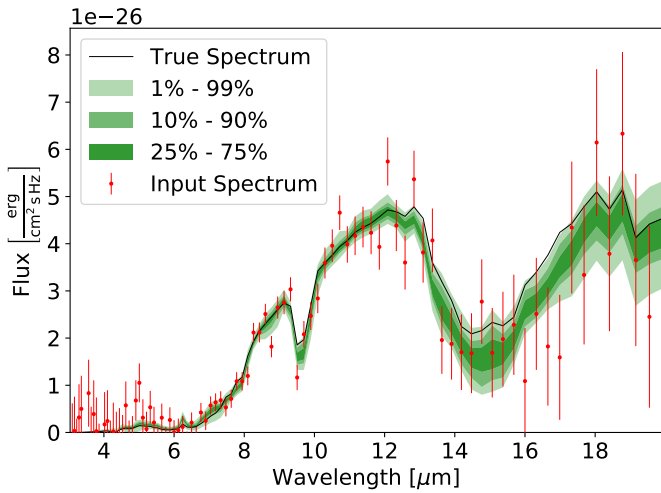


Fig. C.1: Fitted MIR emission spectra to a randomized input spectrum. The non-randomized spectrum is marked by the black line, the randomized input for the retrieval are represented by red data points and errorbars. The green shaded regions mark percentiles of the MIR spectra corresponding to the retrieved posteriors of the model parameters.

molecules. There could be a finite probability of false positive detections, especially if combined with the randomized placement of the spectral points.

In this Section, we investigate how randomizing spectral points and adding more species to the forward model impacts the performance of our retrieval routine at the proposed instrument requirements for *LIFE* ($R = 50$, $S/N = 10$, optimized noise scenario). To this purpose, we generate 20 different noise realizations of the spectrum at these requirements. We randomize the placement of each individual spectral point by randomly sampling a Gaussian distribution, where the standard deviation is determined by the wavelength dependant *LIFE_{SM}* noise. Next, we run a retrieval for every noise realization using the *pyMultiNest* settings outlined in Section 3. In addition to the molecules present in the input spectrum, we also retrieve for traces of NH_3 , PH_3 , and SO_2 . The resulting posteriors are then analyzed and classified using the method outlined in Appendix B.

We summarize our results in Figures C.1, C.2, and C.3. Figure C.1 compares the MIR spectra corresponding to the posteriors retrieved from a single noise realization to the true spectrum. In Figure C.2, we summarize all retrieved posterior types for the considered atmospheric gases. The "Centred" column provides the retrieval findings for the non-randomized input. Columns 1 – 20 list the results for the randomized input spectra. The "Accuracy" column gives the percentage of retrievals on the randomized input that yield the same posterior type as the non-randomized retrieval. The last row provides the log-evidences $\ln(\mathcal{Z})$ for each retrieval run. In Figure C.3, we show all retrieved posterior distributions as histograms and overlay them. Further, we plot the bin-wise mean and median of the posteriors obtained in the randomized retrievals and the posteriors found in the non-randomized retrieval.

Appendix C.1: Truth Versus Spectra from Noisy Retrievals

As can be seen from Figure C.1, our retrieval framework shows robust behaviour even for randomized input spectra. The spec-

tra corresponding to the retrieved posteriors roughly follow the true spectrum and generally do not significantly overfit to the noise. This observation holds for all noise realizations and is reinforced by the finding that the $\ln(\mathcal{Z})$ corresponding to the randomized retrievals are significantly smaller than in the non-randomized case (see Figure C.2). When overfitting, the retrieval models noise induced features accurately and thus the difference between the fitted spectrum and the input spectrum is small. This results in a $\ln(\mathcal{Z})$ value similar to the one obtained in retrievals of non-randomized spectra. In our case, we are not fitting to the noise induced features. Thus, there is a larger difference between the fitted and input spectrum than in the non-randomized case, which results in a smaller $\ln(\mathcal{Z})$.

Despite the good overall fit, a systematic offset between the true and the retrieved spectra starts to emerge above $10 \mu\text{m}$. This offset becomes more pronounced at the longer wavelengths and results from the decreasing density of spectral points and increasing *LIFE_{SM}* noise in this wavelength range. Between 10 and $12 \mu\text{m}$, the molecules we consider have no strong absorption features and thus this range probes the planetary surface conditions. Offsets in this range will manifest themselves as shifts in the retrieved posteriors of P_0 , T_0 , and R_{pl} . Above $12 \mu\text{m}$ the shape of the MIR spectrum is dominated first by CO_2 (up to $\approx 17 \mu\text{m}$) and then by H_2O features. Offsets from the truth in this range correspond to shifts in the retrieved abundance posteriors of these molecules. The described offsets are unique to each of the considered noise realizations and are diminished when averaging the retrieval results obtained from multiple noise realizations (see Section C.3 for a detailed discussion).

Appendix C.2: Robustness of the Retrieved Abundance Posterior Types

In this section we take a closer look at the retrieved abundance posterior types to understand how robust different types are with respect to the noise randomization of the input spectrum. There are two underlying questions. Firstly, how does randomization affect the results for molecules that are present in the atmosphere? Secondly, does randomization trigger false positive detections of molecules not present in the atmosphere?

From Figure C.2, we see that the C-type posterior is robust under randomization. This means that, if retrieving the non-randomized spectrum yields a C-type posterior, retrievals on noise realizations will mostly also yield C-type posteriors. This also shows in the high accuracy percentage. For our study, this observation implies that, at the determined *LIFE* requirements, we can expect to be capable of detecting CO_2 , H_2O , and O_3 in an Earth-twin atmosphere. We observe a similarly strong robustness for the UC-type posterior. From this we can conclude that retrieval behaviour for N_2 , O_2 , and CO is accurately predicted via the non-randomized retrievals presented in our study.

Also the UL-Type posterior shows robust behavior with respect to noise randomization. Here we have to differentiate between two different scenarios:

- N_2O , which is present in the input atmosphere,
- NH_3 , PH_3 , and SO_2 , which are not present.

For N_2O , the high robustness of the UL-type posterior reassures our finding that N_2O is likely not detectable in an Earth-twin at the proposed *LIFE* requirements. However, we do observe rare exceptions where a SL- or even C-Type posterior is retrieved. These exceptions correspond to cases where the randomization of the input spectrum results in a perceived amplification of the N_2O absorption feature. This results in a detection

Centred	Noise Realization																				Accuracy	
	1	2	3	4	5	6	7	8	9	10	11	12	13	14	15	16	17	18	19	20		
N ₂	UC	UC	UC	UC	UC	UC	UC	UC	UC	UC	UC	UC	UC	UC	UC	UC	UC	UL	UC	UC	UC	95 %
O ₂	UC	UC	UC	UC	UC	UC	UC	UC	UC	UC	UC	UC	UC	UC	UC	UC	UC	C	UC	UC	UC	95 %
CO ₂	C	C	C	C	C	C	C	C	C	C	C	C	C	C	C	C	C	SL	C	C	C	95 %
CH ₄	SL	SL	SL	C	UL	C	UL	C	UL	SL	UL	UL	SL	SL	UL	UL	SL	C	UL	SL	UL	35 %
H ₂ O	C	C	C	C	C	C	C	C	C	C	C	C	C	C	C	C	C	C	C	C	C	100 %
O ₃	C	C	C	C	C	C	C	C	C	C	C	C	C	C	C	C	C	C	C	C	C	100 %
CO	UC	UC	UC	UL	UC	UC	UC	UC	UC	UC	UC	UC	UC	UC	UC	UC	UC	UL	UC	UC	UC	90 %
N ₂ O	UL	C	UL	UL	UL	UL	SL	UL	UL	UL	UL	UL	UL	UL	UL	UL	UL	UL	UL	UL	SL	80 %
NH ₃	UL	UL	UL	UL	UL	UL	UL	UL	UL	UL	UL	UL	UL	UL	UL	UL	UL	UL	UL	UL	UL	100 %
PH ₃	UL	UL	UL	UL	UL	UL	UL	UL	UL	UL	UL	UL	UL	UL	UL	UL	UL	UL	UL	UL	UL	100 %
SO ₂	UL	UL	UL	UL	UL	UL	UL	UL	UL	UL	UL	UL	UL	UL	UL	UL	UL	UL	UL	UL	UL	100 %
ln(Z)	-35	-65	-72	-79	-65	-79	-73	-85	-78	-85	-69	-73	-72	-85	-78	-69	-80	-95	-77	-71	-76	

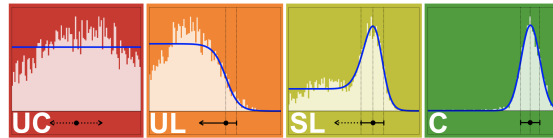


Fig. C.2: Retrieved posterior types for atmospheric gases for the non-randomized case (first column) and the 20 different noise realizations (columns 1 – 20). For posterior classification, we used the method outlined in Appendix B. The last row lists the Bayesian log-evidence $\ln(Z)$, the last column provides the retrieval accuracy (percentage of noise realizations resulting in the same posterior type as the centered case).

of N₂O. Naturally, the occurrence of a N₂O detection is characterized by a strong overestimation of the retrieved N₂O abundance. This can be seen from the retrieved posteriors of N₂O displayed in Figure C.3.

For NH₃, PH₃, and SO₂, we retrieve UL-type posteriors in all cases, which yields upper limits on the abundances of these molecules. We emphasize that retrieving a UL-type posterior is not a false positive detection. A UL-type posterior indicates that molecular abundances below the corresponding upper limit do not lead to an observable signature in the spectrum and therefore cannot be ruled out. The invariance of the retrieved UL-type posterior with respect to the different noise realizations indicates that at *LIFE* requirements we are robust to false positive detections of these molecules. We are aware that this analysis does not generally rule out false positive detections of arbitrary molecules. However, the fact that there was no false positive suggests that we are likely robust with respect to a large variety of false positives.

The most interesting case in this study is CH₄. When not randomizing the input spectrum, we retrieve a SL-type posterior, which indicates that CH₄ lies at the sensitivity limit (for the considered input data). When using the randomized spectra as input, the retrieved posterior types for CH₄ vary between UL,

SL and C. Therefore, SL-type posteriors are not robust with respect to spectrum randomization. The observed variance in retrieved posterior type originates because the randomization of input spectra can lead to an amplification or a reduction of the CH₄ feature (similar as for N₂O). Since the true CH₄ abundance is close to the sensitivity limit, already small differences in the input spectrum can lead to differences in the retrieved posterior type. However, in contrast to N₂O, the peaks of the retrieved SL- and U-type posteriors lie roughly within ± 1 dex of the true CH₄ abundance and do not have a tendency to overestimate it (see Figure C.3). Still, the fact that the posterior type for CH₄ depends on the noise realization leads us to the question of how we should interpret an SL-type posterior in a non-randomized retrieval.

Appendix C.3: Interpretation of Retrievals Results for Unrandomized Spectra

As we discussed in the previous section, SL-type posteriors do not show robust behaviour with respect to noise randomization. This observation raises the question of how to correctly interpret results obtained in retrievals of unrandomized input spectra. In

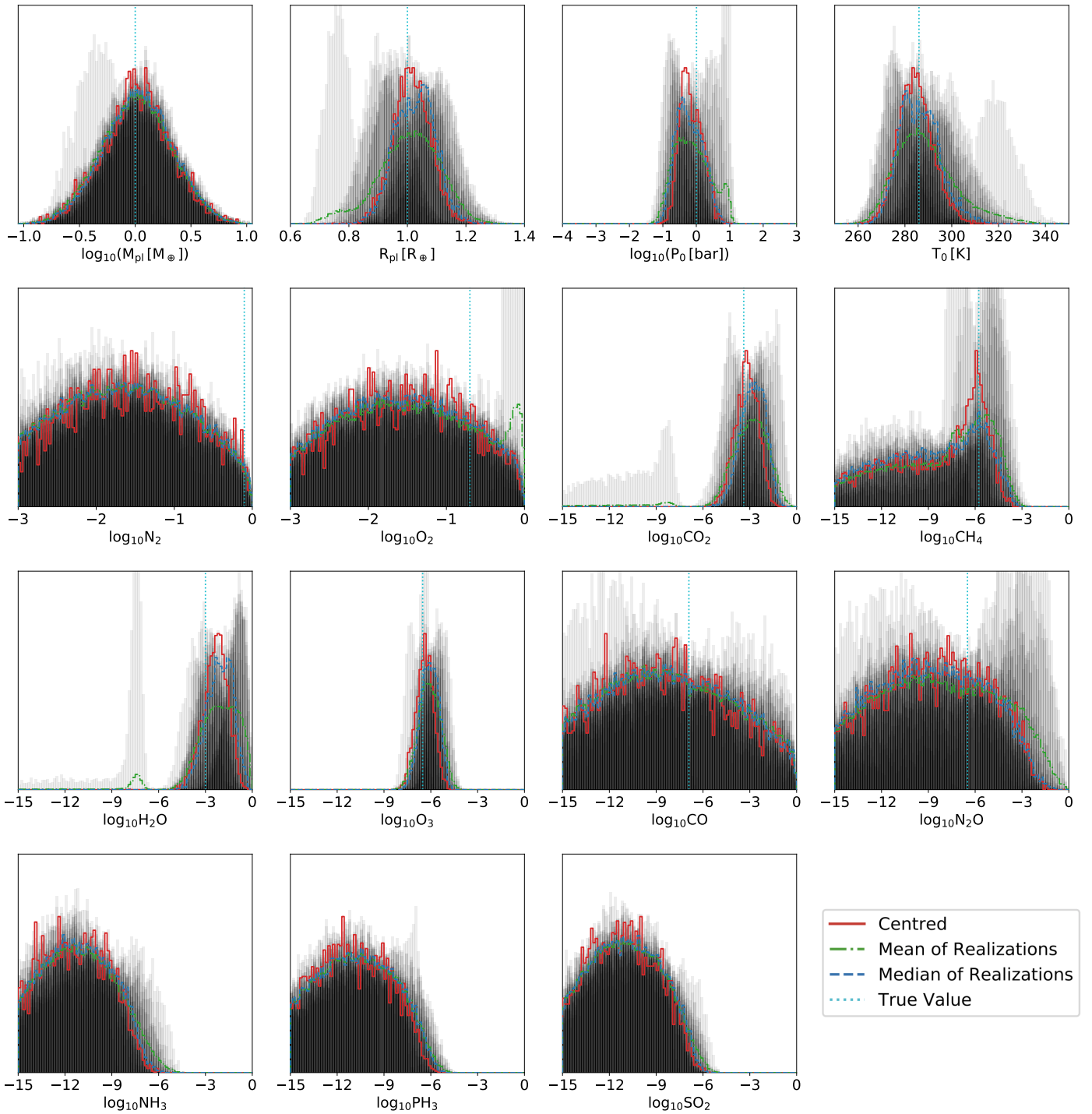


Fig. C.3: Retrieved normalized posterior distributions of some model parameters for the 20 noise realizations. The posteriors of the individual noise realizations are plotted in light grey. The more posteriors overlap, the darker the grey becomes. The green dash-dotted line marks the mean, the blue dashed line the median of the posteriors for the different noise realizations. The posteriors found in the retrieval on the non-randomized spectrum are plotted in solid red. The dotted line marks the true value for the Earth-twin atmosphere. Absence of the dotted line indicates that the species were not present in the atmosphere used to generate the input spectrum.

Figure C.3, we illustrate one possible answer to this question, which we further motivate in this section.

When considering the posteriors from the individual retrieval runs on randomized input spectra (gray shaded areas), we observe that in some cases there are non-neglectable differences between the different results. For the UC-type posteriors (N_2 ,

O_2 , and CO) we observe only small differences between the individual retrieval runs. This underlines the robustness of this posterior type with respect to noise randomization. Similarly, for NH_3 , PH_3 , and SO_2 , we only observe little variance in the retrieved UL-type posteriors, which emphasises the retrievals robustness with respect to false positive detections. Small differ-

ences between the different posteriors correspond to small biases in the retrieved upper abundance limits of these molecules. Similar conclusions can be drawn for N_2O , where most of the retrieved posteriors are of the UL-type. The few deviances from the norm correspond to the previously described cases where an SL-type posterior that overestimates the abundance is retrieved.

The interpretation of posteriors is more subtle when considering C-Type (M_{pl} , R_{pl} , P_0 , T_0 , CO_2 , H_2O , and O_3) or SL-type (CH_4) posteriors. Here we observe a considerable variance in both the shape and the position of the individual posteriors. This observed variance in the posteriors is a bias which is evoked by the noise randomization of the input spectra. We further find that the variation occurs around the true value and its magnitude is comparable to the standard deviation of the posteriors obtained in the non-randomized retrievals. Furthermore, we observe that the regions where many posteriors overlap (the dark regions) are similar in shape and position to the posteriors found in the unrandomized retrieval. In other words, the regions of parameter space that most retrievals agree on corresponds to the retrieval result obtained in the unrandomized retrieval.

Given the observations outlined above, the straightforward interpretation for retrieval results from unrandomized spectra is the following: the retrieved posterior distributions provide an estimate for the average retrieval behaviour. Thus, if we take the average over the results from retrievals on several different noise instances, it will converge towards the posterior distributions found in a retrieval on the unrandomized spectrum. To further motivate this interpretation, we plot the bin-wise mean and median of the posteriors retrieved from the 20 noise realizations in Figure C.3. We find that already for 20 noise realizations, both mean and median are similar in shape and position to the posteriors from the unrandomized retrieval. For all cases the median resembles the unrandomized case more closely because it is less sensitive to outliers.

In conclusion, this study suggests that retrieving on an unrandomized input spectrum eliminates biases that arise from noise randomization and will provide reliable estimates for the average behaviour of the retrieval on randomized spectra. Generally, UC, UL and C-type posteriors show robust behaviour with respect to noise randomization. In contrast, SL-type posteriors are less robust and vary between C-, SL-, and UL-type in retrievals of randomized spectra. This variance in posterior type is closely linked to the fact that SL-type posteriors signify that an abundance is at the sensitivity limit of the retrieval for the studied spectral input.

Appendix D: Retrieved Parameter Values for the Grid Retrievals

See Tables D.1-D.6.

Appendix E: Observation Time Estimates

See Table E.1.

Table D.1: Retrieval results for the 3 – 20 μm wavelength range for the nominal case.

Parameter	Input	R=20				R=35			
		S/N=5	S/N=10	S/N=15	S/N=20	S/N=5	S/N=10	S/N=15	S/N=20
$\sqrt[4]{a_4}$	1.14	1.2 ^{+0.3} _{-0.3}	1.1 ^{+0.2} _{-0.2}	1.0 ^{+0.2} _{-0.2}	1.0 ^{+0.2} _{-0.2}	1.3 ^{+0.3} _{-0.3}	1.1 ^{+0.2} _{-0.2}	1.1 ^{+0.2} _{-0.2}	1.0 ^{+0.2} _{-0.2}
a_3	23.12	34.3 ^{+29.5} _{-19.4}	15.8 ^{+13.0} _{-8.0}	13.2 ^{+9.3} _{-6.6}	13.3 ^{+11.2} _{-6.7}	26.7 ^{+21.3} _{-14.2}	14.7 ^{+11.2} _{-7.2}	14.2 ^{+11.6} _{-7.0}	13.7 ^{+10.1} _{-6.2}
a_2	99.70	163.8 ^{+114.4} _{-80.0}	65.0 ^{+49.7} _{-33.3}	56.0 ^{+38.9} _{-30.0}	52.4 ^{+37.2} _{-25.7}	102.3 ^{+63.0} _{-48.4}	57.2 ^{+35.5} _{-27.4}	57.4 ^{+33.5} _{-24.9}	57.8 ^{+29.9} _{-21.7}
a_1	146.63	147.5 ^{+125.6} _{-76.7}	104.1 ^{+71.1} _{-44.5}	99.2 ^{+68.4} _{-38.5}	80.3 ^{+62.4} _{-31.3}	108.0 ^{+68.6} _{-50.5}	90.3 ^{+47.1} _{-28.8}	87.6 ^{+46.5} _{-31.1}	88.3 ^{+56.0} _{-32.5}
a_0	285.22	234.2 ^{+94.6} _{-93.5}	281.4 ^{+45.3} _{-42.3}	288.1 ^{+45.7} _{-34.3}	266.5 ^{+34.6} _{-26.2}	240.1 ^{+42.8} _{-54.8}	276.3 ^{+34.1} _{-29.7}	269.8 ^{+33.0} _{-27.2}	266.6 ^{+43.3} _{-26.1}
$L(P_0 [\text{bar}])$	0.006	0.4 ^{+0.3} _{-0.5}	0.1 ^{+0.4} _{-0.4}	-0.0 ^{+0.4} _{-0.4}	0.2 ^{+0.3} _{-0.3}	0.4 ^{+0.2} _{-0.3}	0.1 ^{+0.3} _{-0.3}	0.2 ^{+0.3} _{-0.3}	0.2 ^{+0.3} _{-0.4}
$R [R_\oplus]$	1.0	0.82 ^{+0.1} _{-0.1}	0.96 ^{+0.09} _{-0.09}	1.01 ^{+0.08} _{-0.08}	1.02 ^{+0.06} _{-0.07}	0.88 ^{+0.10} _{-0.10}	0.99 ^{+0.08} _{-0.08}	1.01 ^{+0.06} _{-0.06}	1.03 ^{+0.05} _{-0.05}
$L(M [M_\oplus])$	0.0	0.1 ^{+0.3} _{-0.3}	0.0 ^{+0.3} _{-0.3}	0.0 ^{+0.3} _{-0.3}	0.0 ^{+0.3} _{-0.3}	0.0 ^{+0.3} _{-0.3}	0.0 ^{+0.3} _{-0.3}	0.0 ^{+0.3} _{-0.3}	0.0 ^{+0.3} _{-0.3}
$L(\text{N}_2)$	-0.107	-7.3 ^{+4.1} _{-4.4}	-7.8 ^{+4.6} _{-4.2}	-7.6 ^{+4.6} _{-4.5}	-7.6 ^{+4.5} _{-4.5}	-7.5 ^{+4.4} _{-4.3}	-7.4 ^{+4.4} _{-4.4}	-7.7 ^{+4.6} _{-4.4}	-7.8 ^{+4.7} _{-4.4}
$L(\text{O}_2)$	-0.679	-7.0 ^{+4.2} _{-4.6}	-7.1 ^{+4.4} _{-4.6}	-7.4 ^{+4.5} _{-4.5}	-7.5 ^{+4.6} _{-4.7}	-7.7 ^{+4.5} _{-4.3}	-7.4 ^{+4.3} _{-4.6}	-7.6 ^{+4.5} _{-4.5}	-7.5 ^{+4.7} _{-4.8}
$L(\text{H}_2\text{O})$	-3.000	-9.4 ^{+3.8} _{-3.4}	-3.2 ^{+1.1} _{-1.1}	-2.7 ^{+0.9} _{-0.8}	-3.1 ^{+0.7} _{-0.7}	-5.3 ^{+1.7} _{-5.2}	-2.9 ^{+0.8} _{-0.8}	-3.0 ^{+0.7} _{-0.7}	-3.0 ^{+0.8} _{-0.7}
$L(\text{CO}_2)$	-3.387	-6.6 ^{+1.9} _{-4.8}	-3.6 ^{+0.9} _{-0.8}	-3.2 ^{+0.7} _{-0.7}	-3.6 ^{+0.7} _{-0.6}	-4.6 ^{+0.8} _{-1.0}	-3.4 ^{+0.8} _{-0.7}	-3.5 ^{+0.7} _{-0.6}	-3.5 ^{+0.7} _{-0.6}
$L(\text{CH}_4)$	-5.770	-9.9 ^{+3.1} _{-3.0}	-8.7 ^{+3.2} _{-3.8}	-9.2 ^{+3.4} _{-3.6}	-9.6 ^{+3.3} _{-3.2}	-9.2 ^{+3.4} _{-3.3}	-9.7 ^{+3.6} _{-3.2}	-9.3 ^{+3.2} _{-3.3}	-9.0 ^{+2.8} _{-3.8}
$L(\text{O}_3)$	-6.523	-10.3 ^{+2.7} _{-2.8}	-6.8 ^{+0.9} _{-2.2}	-6.4 ^{+0.6} _{-0.6}	-6.7 ^{+0.5} _{-0.5}	-9.6 ^{+2.5} _{-3.3}	-6.5 ^{+0.6} _{-0.6}	-6.6 ^{+0.5} _{-0.5}	-6.7 ^{+0.6} _{-0.5}
$L(\text{CO})$	-6.903	-9.8 ^{+3.3} _{-3.0}	-7.8 ^{+4.3} _{-4.3}	-7.5 ^{+4.3} _{-4.5}	-7.7 ^{+4.5} _{-4.3}	-8.7 ^{+4.0} _{-3.7}	-7.7 ^{+4.3} _{-4.2}	-7.7 ^{+4.4} _{-4.4}	-7.7 ^{+4.3} _{-4.5}
$L(\text{N}_2\text{O})$	-6.495	-10.3 ^{+2.8} _{-2.6}	-8.5 ^{+3.8} _{-3.9}	-8.1 ^{+3.7} _{-3.9}	-8.5 ^{+3.6} _{-4.0}	-9.4 ^{+3.5} _{-3.2}	-8.3 ^{+3.6} _{-3.9}	-8.7 ^{+3.6} _{-3.9}	-8.9 ^{+3.4} _{-3.7}

Parameter	Input	R=50				R=100			
		S/N=5	S/N=10	S/N=15	S/N=20	S/N=5	S/N=10	S/N=15	S/N=20
$\sqrt[4]{a_4}$	1.14	1.2 ^{+0.3} _{-0.2}	1.0 ^{+0.2} _{-0.2}	1.1 ^{+0.3} _{-0.2}	1.0 ^{+0.2} _{-0.2}	1.1 ^{+0.2} _{-0.2}	1.0 ^{+0.2} _{-0.2}	1.0 ^{+0.2} _{-0.2}	1.1 ^{+0.2} _{-0.2}
a_3	23.12	22.2 ^{+29.6} _{-10.6}	14.4 ^{+11.8} _{-7.4}	18.0 ^{+20.9} _{-8.4}	15.3 ^{+11.2} _{-6.3}	12.9 ^{+10.0} _{-6.6}	14.1 ^{+11.4} _{-6.2}	16.2 ^{+12.1} _{-6.6}	19.3 ^{+16.8} _{-8.4}
a_2	99.70	94.0 ^{+69.0} _{-41.9}	61.6 ^{+43.5} _{-29.0}	76.6 ^{+69.7} _{-33.1}	71.8 ^{+34.7} _{-26.9}	47.8 ^{+26.9} _{-21.8}	62.6 ^{+35.2} _{-24.5}	73.5 ^{+34.7} _{-22.7}	88.6 ^{+56.3} _{-30.0}
a_1	146.63	120.6 ^{+72.6} _{-47.8}	102.0 ^{+70.2} _{-38.2}	134.5 ^{+83.4} _{-69.7}	114.0 ^{+81.2} _{-42.8}	70.3 ^{+33.5} _{-24.8}	101.3 ^{+64.2} _{-42.1}	115.4 ^{+68.2} _{-36.3}	154.1 ^{+68.0} _{-62.4}
a_0	285.22	265.1 ^{+47.0} _{-41.7}	285.1 ^{+39.9} _{-34.3}	294.1 ^{+49.0} _{-44.8}	280.4 ^{+61.1} _{-32.2}	256.0 ^{+30.6} _{-24.4}	273.9 ^{+45.1} _{-30.8}	279.2 ^{+47.7} _{-26.3}	298.8 ^{+41.7} _{-38.8}
$L(P_0 [\text{bar}])$	0.006	0.2 ^{+0.3} _{-0.3}	0.0 ^{+0.4} _{-0.3}	-0.1 ^{+0.5} _{-0.3}	0.0 ^{+0.3} _{-0.4}	0.3 ^{+0.3} _{-0.3}	0.1 ^{+0.4} _{-0.4}	0.0 ^{+0.3} _{-0.3}	-0.1 ^{+0.3} _{-0.2}
$R [R_\oplus]$	1.0	0.92 ^{+0.09} _{-0.09}	1.01 ^{+0.07} _{-0.07}	1.03 ^{+0.06} _{-0.05}	1.03 ^{+0.05} _{-0.05}	0.98 ^{+0.08} _{-0.08}	1.02 ^{+0.06} _{-0.06}	1.02 ^{+0.04} _{-0.04}	1.01 ^{+0.04} _{-0.03}
$L(M [M_\oplus])$	0.0	0.0 ^{+0.3} _{-0.3}	0.0 ^{+0.3} _{-0.3}	0.0 ^{+0.3} _{-0.3}	0.0 ^{+0.3} _{-0.3}	-0.0 ^{+0.3} _{-0.3}	-0.0 ^{+0.3} _{-0.3}	-0.0 ^{+0.3} _{-0.3}	0.0 ^{+0.3} _{-0.3}
$L(\text{N}_2)$	-0.107	-6.5 ^{+4.0} _{-4.6}	-7.6 ^{+4.5} _{-4.5}	-7.3 ^{+4.4} _{-4.7}	-7.6 ^{+4.7} _{-4.5}	-7.9 ^{+4.5} _{-4.1}	-7.9 ^{+4.8} _{-4.5}	-7.4 ^{+4.4} _{-4.6}	-7.4 ^{+4.6} _{-4.7}
$L(\text{O}_2)$	-0.679	-7.8 ^{+4.5} _{-4.3}	-7.2 ^{+4.4} _{-4.5}	-7.1 ^{+4.5} _{-4.7}	-7.5 ^{+4.7} _{-4.5}	-7.4 ^{+4.2} _{-4.4}	-7.8 ^{+5.0} _{-4.3}	-7.3 ^{+4.5} _{-4.7}	-7.5 ^{+4.6} _{-4.6}
$L(\text{H}_2\text{O})$	-3.000	-3.7 ^{+1.1} _{-2.1}	-2.8 ^{+0.8} _{-0.8}	-2.7 ^{+0.7} _{-0.8}	-2.8 ^{+0.8} _{-0.7}	-3.6 ^{+0.9} _{-0.8}	-3.0 ^{+0.8} _{-0.8}	-2.9 ^{+0.6} _{-0.6}	-2.7 ^{+0.5} _{-0.6}
$L(\text{CO}_2)$	-3.387	-4.0 ^{+0.8} _{-0.8}	-3.3 ^{+0.7} _{-0.7}	-3.2 ^{+0.7} _{-0.7}	-3.3 ^{+0.7} _{-0.7}	-3.9 ^{+0.8} _{-0.7}	-3.4 ^{+0.7} _{-0.7}	-3.3 ^{+0.6} _{-0.5}	-3.2 ^{+0.5} _{-0.5}
$L(\text{CH}_4)$	-5.770	-8.5 ^{+3.1} _{-3.8}	-9.0 ^{+3.1} _{-3.6}	-8.8 ^{+2.9} _{-3.7}	-7.7 ^{+2.1} _{-4.4}	-9.5 ^{+3.2} _{-3.3}	-8.7 ^{+2.7} _{-3.7}	-6.8 ^{+1.3} _{-4.2}	-5.9 ^{+0.7} _{-1.4}
$L(\text{O}_3)$	-6.523	-7.7 ^{+1.4} _{-4.1}	-6.5 ^{+0.6} _{-0.6}	-6.5 ^{+0.6} _{-0.6}	-6.5 ^{+0.5} _{-0.5}	-7.0 ^{+0.7} _{-0.7}	-6.6 ^{+0.6} _{-0.5}	-6.5 ^{+0.4} _{-0.4}	-6.4 ^{+0.4} _{-0.4}
$L(\text{CO})$	-6.903	-7.8 ^{+4.0} _{-4.0}	-7.8 ^{+4.5} _{-4.3}	-7.7 ^{+4.4} _{-4.5}	-7.9 ^{+4.4} _{-4.3}	-8.1 ^{+4.5} _{-4.0}	-7.7 ^{+4.7} _{-4.5}	-7.8 ^{+4.6} _{-4.4}	-8.0 ^{+4.6} _{-4.4}
$L(\text{N}_2\text{O})$	-6.495	-9.0 ^{+3.8} _{-3.4}	-8.5 ^{+3.7} _{-3.8}	-8.7 ^{+3.5} _{-3.9}	-8.9 ^{+3.4} _{-3.7}	-9.1 ^{+3.5} _{-3.4}	-9.0 ^{+3.6} _{-3.7}	-9.0 ^{+3.4} _{-3.6}	-9.3 ^{+3.5} _{-3.7}

Notes. Here, $L(\cdot)$ stands for $\log_{10}(\cdot)$.

Table D.2: Retrieval results for the 3 – 20 μm wavelength range for the optimized case.

Parameter	Input	R=20				R=35			
		S/N=5	S/N=10	S/N=15	S/N=20	S/N=5	S/N=10	S/N=15	S/N=20
$\sqrt[4]{a_4}$	1.14	1.2 ^{+0.2} _{-0.3}	1.0 ^{+0.2} _{-0.2}	1.0 ^{+0.2} _{-0.2}	1.0 ^{+0.2} _{-0.2}	1.1 ^{+0.2} _{-0.2}	1.0 ^{+0.2} _{-0.2}	1.0 ^{+0.2} _{-0.2}	1.0 ^{+0.2} _{-0.2}
a_3	23.12	25.5 ^{+20.0} _{-12.3}	14.2 ^{+9.4} _{-6.7}	10.7 ^{+8.0} _{-5.3}	13.2 ^{+11.7} _{-6.4}	16.4 ^{+14.3} _{-8.2}	10.6 ^{+7.1} _{-5.1}	11.5 ^{+10.3} _{-5.4}	11.8 ^{+8.2} _{-5.0}
a_2	99.70	108.3 ^{+59.0} _{-41.4}	60.4 ^{+36.3} _{-27.5}	38.9 ^{+30.2} _{-20.8}	61.3 ^{+51.6} _{-32.6}	64.1 ^{+41.2} _{-30.6}	43.3 ^{+33.8} _{-22.8}	47.0 ^{+36.5} _{-21.8}	50.0 ^{+26.1} _{-20.2}
a_1	146.63	128.8 ^{+67.5} _{-60.6}	105.4 ^{+51.8} _{-37.0}	71.4 ^{+42.2} _{-25.9}	130.8 ^{+97.0} _{-60.7}	86.5 ^{+56.6} _{-43.8}	91.4 ^{+53.7} _{-31.0}	89.4 ^{+59.0} _{-32.5}	89.1 ^{+42.1} _{-30.6}
a_0	285.22	201.5 ^{+73.6} _{-73.0}	266.4 ^{+42.4} _{-33.2}	266.6 ^{+33.0} _{-27.8}	323.4 ^{+66.8} _{-45.3}	227.9 ^{+46.2} _{-59.1}	294.7 ^{+40.7} _{-37.9}	285.8 ^{+43.6} _{-32.5}	277.9 ^{+29.5} _{-24.8}
$L(P_0 [\text{bar}])$	0.006	0.5 ^{+0.3} _{-0.4}	0.2 ^{+0.3} _{-0.4}	0.2 ^{+0.4} _{-0.4}	-0.3 ^{+0.4} _{-0.3}	0.6 ^{+0.3} _{-0.4}	-0.1 ^{+0.4} _{-0.4}	0.0 ^{+0.4} _{-0.4}	0.1 ^{+0.3} _{-0.3}
$R [R_\oplus]$	1.0	0.9 ^{+0.1} _{-0.1}	0.99 ^{+0.09} _{-0.09}	1.01 ^{+0.07} _{-0.06}	1.02 ^{+0.06} _{-0.05}	0.9 ^{+0.1} _{-0.1}	1.01 ^{+0.07} _{-0.07}	1.02 ^{+0.05} _{-0.05}	1.02 ^{+0.04} _{-0.04}
$L(M [M_\oplus])$	0.0	0.0 ^{+0.3} _{-0.3}	0.0 ^{+0.3} _{-0.3}	0.0 ^{+0.3} _{-0.3}	0.0 ^{+0.3} _{-0.3}	0.0 ^{+0.3} _{-0.3}	0.0 ^{+0.3} _{-0.3}	0.0 ^{+0.3} _{-0.3}	0.0 ^{+0.3} _{-0.3}
$L(\text{N}_2)$	-0.107	-7.6 ^{+4.3} _{-4.2}	-7.9 ^{+4.5} _{-4.2}	-7.7 ^{+4.4} _{-4.5}	-7.8 ^{+4.7} _{-4.3}	-7.6 ^{+4.2} _{-4.3}	-7.2 ^{+4.2} _{-4.6}	-7.5 ^{+4.6} _{-4.5}	-7.5 ^{+4.6} _{-4.4}
$L(\text{O}_2)$	-0.679	-7.0 ^{+4.8} _{-4.6}	-7.3 ^{+4.4} _{-4.6}	-7.1 ^{+4.3} _{-4.3}	-7.9 ^{+4.5} _{-4.3}	-7.1 ^{+4.2} _{-4.5}	-7.8 ^{+4.6} _{-4.4}	-7.4 ^{+4.4} _{-4.5}	-7.5 ^{+4.6} _{-4.5}
$L(\text{H}_2\text{O})$	-3.000	-4.2 ^{+1.1} _{-3.0}	-2.9 ^{+0.9} _{-0.8}	-2.9 ^{+0.8} _{-0.8}	-1.7 ^{+0.7} _{-0.9}	-3.8 ^{+1.0} _{-0.9}	-2.1 ^{+0.9} _{-1.0}	-2.4 ^{+0.9} _{-0.9}	-2.7 ^{+0.7} _{-0.6}
$L(\text{CO}_2)$	-3.387	-6.6 ^{+2.0} _{-4.6}	-3.9 ^{+0.9} _{-0.9}	-3.7 ^{+0.8} _{-0.8}	-2.6 ^{+0.6} _{-0.8}	-5.1 ^{+1.2} _{-2.4}	-3.1 ^{+0.9} _{-0.9}	-3.1 ^{+0.8} _{-0.8}	-3.3 ^{+0.6} _{-0.6}
$L(\text{CH}_4)$	-5.770	-9.8 ^{+2.8} _{-3.0}	-9.9 ^{+3.1} _{-3.1}	-9.5 ^{+3.0} _{-3.4}	-7.9 ^{+2.6} _{-4.1}	-10.2 ^{+2.8} _{-2.8}	-9.4 ^{+3.1} _{-3.3}	-8.0 ^{+2.2} _{-4.2}	-6.5 ^{+0.9} _{-4.0}
$L(\text{O}_3)$	-6.523	-9.7 ^{+2.3} _{-3.0}	-6.7 ^{+0.7} _{-0.7}	-6.6 ^{+0.6} _{-0.6}	-5.9 ^{+0.6} _{-0.6}	-7.5 ^{+0.8} _{-2.7}	-6.2 ^{+0.7} _{-0.7}	-6.3 ^{+0.6} _{-0.6}	-6.5 ^{+0.5} _{-0.4}
$L(\text{CO})$	-6.903	-9.0 ^{+3.9} _{-3.6}	-7.5 ^{+4.4} _{-4.5}	-7.8 ^{+4.5} _{-4.5}	-7.9 ^{+4.5} _{-4.3}	-8.3 ^{+3.9} _{-3.9}	-7.5 ^{+4.4} _{-4.5}	-7.7 ^{+4.4} _{-4.4}	-8.1 ^{+4.3} _{-4.4}
$L(\text{N}_2\text{O})$	-6.495	-9.8 ^{+3.3} _{-3.0}	-8.9 ^{+3.7} _{-3.6}	-9.0 ^{+3.6} _{-3.6}	-8.3 ^{+3.4} _{-3.9}	-8.8 ^{+3.4} _{-3.5}	-8.8 ^{+3.8} _{-3.7}	-9.4 ^{+3.8} _{-3.3}	-9.4 ^{+3.3} _{-3.4}

Parameter	Input	R=50				R=100			
		S/N=5	S/N=10	S/N=15	S/N=20	S/N=5	S/N=10	S/N=15	S/N=20
$\sqrt[4]{a_4}$	1.14	1.3 ^{+0.2} _{-0.2}	1.0 ^{+0.2} _{-0.2}	1.0 ^{+0.2} _{-0.2}	1.1 ^{+0.2} _{-0.2}	1.0 ^{+0.2} _{-0.2}	1.0 ^{+0.2} _{-0.2}	1.1 ^{+0.2} _{-0.2}	1.0 ^{+0.2} _{-0.2}
a_3	23.12	30.4 ^{+16.3} _{-13.0}	14.1 ^{+11.0} _{-6.7}	11.7 ^{+9.5} _{-5.1}	13.9 ^{+9.7} _{-6.2}	10.7 ^{+7.6} _{-5.1}	14.7 ^{+10.1} _{-6.4}	19.1 ^{+18.2} _{-8.4}	17.0 ^{+10.6} _{-6.7}
a_2	99.70	112.7 ^{+47.3} _{-41.3}	64.4 ^{+41.8} _{-30.6}	43.8 ^{+25.2} _{-18.1}	53.2 ^{+28.0} _{-19.9}	40.3 ^{+31.5} _{-21.0}	67.9 ^{+38.4} _{-26.6}	86.6 ^{+59.2} _{-37.8}	78.0 ^{+41.7} _{-26.9}
a_1	146.63	141.1 ^{+81.8} _{-54.4}	126.8 ^{+72.6} _{-44.3}	69.1 ^{+32.7} _{-20.7}	79.3 ^{+37.2} _{-27.2}	79.7 ^{+55.1} _{-33.1}	128.1 ^{+72.9} _{-46.1}	148.4 ^{+81.3} _{-72.5}	132.2 ^{+61.8} _{-56.2}
a_0	285.22	255.5 ^{+48.8} _{-41.8}	311.1 ^{+52.0} _{-31.6}	260.9 ^{+23.3} _{-19.7}	260.8 ^{+22.6} _{-19.2}	273.8 ^{+44.5} _{-32.1}	306.9 ^{+56.2} _{-39.7}	298.4 ^{+54.4} _{-42.5}	286.7 ^{+39.6} _{-34.3}
$L(P_0 [\text{bar}])$	0.006	0.2 ^{+0.2} _{-0.3}	-0.2 ^{+0.3} _{-0.3}	0.3 ^{+0.2} _{-0.3}	0.3 ^{+0.3} _{-0.2}	0.1 ^{+0.4} _{-0.4}	-0.2 ^{+0.4} _{-0.3}	-0.1 ^{+0.4} _{-0.3}	-0.0 ^{+0.4} _{-0.2}
$R [R_\oplus]$	1.0	0.98 ^{+0.09} _{-0.09}	1.02 ^{+0.06} _{-0.06}	1.01 ^{+0.05} _{-0.04}	1.01 ^{+0.03} _{-0.03}	1.01 ^{+0.08} _{-0.08}	1.01 ^{+0.05} _{-0.04}	1.0 ^{+0.03} _{-0.03}	1.0 ^{+0.02} _{-0.02}
$L(M [M_\oplus])$	0.0	0.1 ^{+0.2} _{-0.3}	0.0 ^{+0.3} _{-0.3}	0.0 ^{+0.3} _{-0.3}	0.0 ^{+0.3} _{-0.3}	0.0 ^{+0.3} _{-0.3}	0.0 ^{+0.3} _{-0.3}	0.0 ^{+0.3} _{-0.3}	0.0 ^{+0.3} _{-0.3}
$L(\text{N}_2)$	-0.107	-7.8 ^{+4.2} _{-4.0}	-7.7 ^{+4.7} _{-4.3}	-7.8 ^{+4.6} _{-4.4}	-7.1 ^{+4.2} _{-4.5}	-7.3 ^{+4.5} _{-4.8}	-7.4 ^{+4.6} _{-4.6}	-7.5 ^{+4.6} _{-4.7}	-7.1 ^{+4.5} _{-4.9}
$L(\text{O}_2)$	-0.679	-7.1 ^{+4.2} _{-4.2}	-7.6 ^{+4.5} _{-4.6}	-7.5 ^{+4.5} _{-4.6}	-7.4 ^{+4.6} _{-4.7}	-7.2 ^{+4.3} _{-4.6}	-7.1 ^{+4.4} _{-4.7}	-7.7 ^{+4.8} _{-4.5}	-7.9 ^{+5.0} _{-4.2}
$L(\text{H}_2\text{O})$	-3.000	-3.2 ^{+0.8} _{-0.7}	-2.0 ^{+0.7} _{-0.7}	-3.2 ^{+0.7} _{-0.6}	-3.3 ^{+0.6} _{-0.6}	-2.8 ^{+1.1} _{-0.9}	-2.4 ^{+0.8} _{-0.8}	-2.8 ^{+0.6} _{-0.7}	-2.9 ^{+0.5} _{-0.6}
$L(\text{CO}_2)$	-3.387	-4.2 ^{+0.8} _{-1.0}	-2.9 ^{+0.7} _{-0.7}	-3.7 ^{+0.6} _{-0.5}	-3.7 ^{+0.5} _{-0.5}	-3.5 ^{+1.0} _{-0.9}	-2.9 ^{+0.7} _{-0.7}	-3.2 ^{+0.6} _{-0.6}	-3.3 ^{+0.5} _{-0.5}
$L(\text{CH}_4)$	-5.770	-9.5 ^{+2.9} _{-3.0}	-8.0 ^{+2.6} _{-4.4}	-6.6 ^{+0.7} _{-3.3}	-6.2 ^{+0.5} _{-0.6}	-8.9 ^{+2.8} _{-3.8}	-5.7 ^{+0.9} _{-1.1}	-5.7 ^{+0.6} _{-0.7}	-5.8 ^{+0.5} _{-0.6}
$L(\text{O}_3)$	-6.523	-7.0 ^{+0.6} _{-0.9}	-6.1 ^{+0.5} _{-0.5}	-6.7 ^{+0.4} _{-0.4}	-6.7 ^{+0.4} _{-0.4}	-6.6 ^{+0.8} _{-0.6}	-6.2 ^{+0.6} _{-0.5}	-6.4 ^{+0.5} _{-0.5}	-6.5 ^{+0.4} _{-0.4}
$L(\text{CO})$	-6.903	-7.8 ^{+4.3} _{-4.1}	-8.0 ^{+4.6} _{-4.4}	-8.0 ^{+4.5} _{-4.2}	-8.2 ^{+4.5} _{-4.0}	-7.9 ^{+4.6} _{-4.6}	-7.8 ^{+4.3} _{-4.4}	-8.6 ^{+4.4} _{-4.0}	-8.5 ^{+4.1} _{-4.1}
$L(\text{N}_2\text{O})$	-6.495	-9.8 ^{+3.6} _{-3.0}	-8.3 ^{+3.5} _{-3.9}	-9.3 ^{+3.2} _{-3.4}	-9.5 ^{+3.2} _{-3.5}	-8.5 ^{+3.7} _{-3.9}	-9.0 ^{+3.6} _{-3.6}	-9.4 ^{+3.2} _{-3.5}	-9.7 ^{+3.2} _{-3.2}

Notes. Here, $L(\cdot)$ stands for $\log_{10}(\cdot)$.

Table D.3: Retrieval results for the 4 – 18.5 μm wavelength range for the nominal case.

Parameter	Input	R=20				R=35			
		S/N=5	S/N=10	S/N=15	S/N=20	S/N=5	S/N=10	S/N=15	S/N=20
$\sqrt[4]{a_4}$	1.14	1.3 ^{+0.3} _{-0.3}	1.1 ^{+0.2} _{-0.2}	1.1 ^{+0.2} _{-0.2}	1.0 ^{+0.2} _{-0.2}	1.1 ^{+0.2} _{-0.2}	1.0 ^{+0.2} _{-0.2}	1.0 ^{+0.2} _{-0.2}	1.0 ^{+0.2} _{-0.2}
a_3	23.12	39.3 ^{+28.4} _{-22.0}	15.1 ^{+10.1} _{-7.1}	14.9 ^{+13.0} _{-7.4}	11.7 ^{+10.5} _{-5.7}	18.9 ^{+17.0} _{-9.3}	12.1 ^{+10.1} _{-5.9}	12.6 ^{+9.7} _{-5.8}	13.5 ^{+11.1} _{-6.5}
a_2	99.70	192.8 ^{+137.4} _{-90.8}	60.8 ^{+34.4} _{-28.7}	59.1 ^{+46.5} _{-29.8}	45.3 ^{+37.7} _{-22.1}	85.3 ^{+58.3} _{-41.0}	53.4 ^{+36.6} _{-26.3}	52.4 ^{+28.2} _{-24.2}	57.6 ^{+35.7} _{-24.2}
a_1	146.63	176.0 ^{+176.3} _{-90.0}	98.3 ^{+38.2} _{-31.5}	99.4 ^{+60.6} _{-35.8}	80.5 ^{+56.6} _{-31.1}	127.6 ^{+89.4} _{-60.3}	103.3 ^{+53.6} _{-36.5}	84.0 ^{+47.5} _{-32.6}	93.0 ^{+55.1} _{-33.2}
a_0	285.22	272.1 ^{+93.4} _{-107.3}	267.3 ^{+32.8} _{-30.9}	280.4 ^{+40.9} _{-31.4}	275.1 ^{+41.1} _{-33.0}	265.1 ^{+59.5} _{-53.7}	291.7 ^{+44.0} _{-33.7}	270.0 ^{+33.3} _{-28.4}	273.6 ^{+36.6} _{-26.8}
$L(P_0 [\text{bar}])$	0.006	0.1 ^{+0.5} _{-0.5}	0.2 ^{+0.2} _{-0.3}	0.0 ^{+0.3} _{-0.3}	0.1 ^{+0.4} _{-0.4}	0.2 ^{+0.4} _{-0.4}	-0.1 ^{+0.4} _{-0.4}	0.2 ^{+0.4} _{-0.3}	0.1 ^{+0.3} _{-0.3}
$R [R_\oplus]$	1.0	0.86 ^{+0.1} _{-0.09}	0.99 ^{+0.1} _{-0.1}	1.01 ^{+0.07} _{-0.08}	1.03 ^{+0.06} _{-0.06}	0.9 ^{+0.1} _{-0.1}	1.01 ^{+0.08} _{-0.08}	1.02 ^{+0.06} _{-0.06}	1.03 ^{+0.05} _{-0.05}
$L(M [M_\oplus])$	0.0	0.1 ^{+0.3} _{-0.3}	0.0 ^{+0.3} _{-0.3}	0.0 ^{+0.3} _{-0.3}	0.0 ^{+0.3} _{-0.3}	-0.0 ^{+0.3} _{-0.3}	0.0 ^{+0.3} _{-0.3}	0.0 ^{+0.3} _{-0.3}	0.0 ^{+0.3} _{-0.3}
$L(\text{N}_2)$	-0.107	-7.6 ^{+4.2} _{-4.2}	-7.4 ^{+4.4} _{-4.4}	-7.6 ^{+4.7} _{-4.5}	-7.1 ^{+4.2} _{-4.7}	-7.0 ^{+4.0} _{-4.3}	-7.2 ^{+4.5} _{-4.7}	-7.2 ^{+4.5} _{-4.9}	-7.4 ^{+4.6} _{-4.7}
$L(\text{O}_2)$	-0.679	-7.4 ^{+4.5} _{-4.5}	-7.6 ^{+4.5} _{-4.5}	-7.7 ^{+4.5} _{-4.3}	-7.2 ^{+4.5} _{-4.5}	-8.0 ^{+4.6} _{-4.2}	-8.0 ^{+4.4} _{-4.4}	-8.0 ^{+4.8} _{-4.4}	-7.5 ^{+4.5} _{-4.8}
$L(\text{H}_2\text{O})$	-3.000	-9.5 ^{+4.1} _{-3.2}	-3.2 ^{+0.9} _{-0.8}	-2.7 ^{+0.8} _{-0.8}	-2.7 ^{+0.9} _{-0.9}	-3.8 ^{+1.4} _{-1.6}	-2.5 ^{+0.9} _{-0.9}	-2.9 ^{+0.8} _{-0.8}	-2.8 ^{+0.7} _{-0.7}
$L(\text{CO}_2)$	-3.387	-9.2 ^{+3.7} _{-3.5}	-3.8 ^{+0.8} _{-0.8}	-3.4 ^{+0.8} _{-0.7}	-3.4 ^{+0.8} _{-0.7}	-4.3 ^{+1.1} _{-1.3}	-3.2 ^{+0.9} _{-0.8}	-3.5 ^{+0.7} _{-0.7}	-3.4 ^{+0.7} _{-0.6}
$L(\text{CH}_4)$	-5.770	-10.2 ^{+2.9} _{-2.8}	-9.5 ^{+3.3} _{-3.4}	-9.2 ^{+3.1} _{-3.5}	-9.2 ^{+3.1} _{-3.5}	-9.2 ^{+3.1} _{-3.3}	-9.5 ^{+3.4} _{-3.4}	-9.0 ^{+2.9} _{-3.5}	-8.0 ^{+2.1} _{-4.3}
$L(\text{O}_3)$	-6.523	-10.5 ^{+2.6} _{-2.5}	-7.0 ^{+0.8} _{-3.5}	-6.4 ^{+0.6} _{-0.6}	-6.5 ^{+0.6} _{-0.6}	-8.5 ^{+2.0} _{-3.7}	-6.3 ^{+0.7} _{-0.6}	-6.6 ^{+0.5} _{-0.6}	-6.6 ^{+0.5} _{-0.5}
$L(\text{CO})$	-6.903	-10.5 ^{+3.1} _{-2.7}	-7.8 ^{+4.4} _{-4.4}	-8.0 ^{+4.5} _{-4.3}	-8.2 ^{+4.7} _{-4.2}	-8.1 ^{+4.0} _{-3.9}	-7.5 ^{+4.3} _{-4.5}	-7.9 ^{+4.7} _{-4.5}	-7.9 ^{+4.6} _{-4.4}
$L(\text{N}_2\text{O})$	-6.495	-10.5 ^{+2.7} _{-2.6}	-8.8 ^{+3.8} _{-3.6}	-8.5 ^{+3.7} _{-3.8}	-8.9 ^{+3.5} _{-3.8}	-9.6 ^{+3.5} _{-3.1}	-8.9 ^{+4.0} _{-3.9}	-9.2 ^{+3.8} _{-3.6}	-9.3 ^{+3.6} _{-3.5}

Parameter	Input	R=50				R=100			
		S/N=5	S/N=10	S/N=15	S/N=20	S/N=5	S/N=10	S/N=15	S/N=20
$\sqrt[4]{a_4}$	1.14	1.1 ^{+0.2} _{-0.2}	1.1 ^{+0.2} _{-0.2}	1.0 ^{+0.2} _{-0.2}	1.0 ^{+0.2} _{-0.2}	1.0 ^{+0.2} _{-0.2}	1.0 ^{+0.2} _{-0.2}	1.0 ^{+0.2} _{-0.2}	1.1 ^{+0.2} _{-0.2}
a_3	23.12	17.4 ^{+12.5} _{-8.8}	16.5 ^{+14.5} _{-8.9}	14.4 ^{+9.1} _{-6.6}	14.4 ^{+12.1} _{-6.5}	14.5 ^{+12.9} _{-7.4}	13.5 ^{+9.5} _{-6.0}	14.9 ^{+10.7} _{-6.1}	19.8 ^{+13.1} _{-8.1}
a_2	99.70	77.0 ^{+54.3} _{-39.5}	62.6 ^{+56.0} _{-29.8}	63.4 ^{+39.7} _{-26.0}	60.2 ^{+32.0} _{-21.5}	61.2 ^{+44.3} _{-29.6}	59.6 ^{+37.7} _{-23.1}	67.2 ^{+32.6} _{-24.4}	86.9 ^{+35.4} _{-27.1}
a_1	146.63	127.5 ^{+93.3} _{-56.3}	100.0 ^{+78.3} _{-38.0}	109.7 ^{+85.1} _{-44.5}	90.2 ^{+46.2} _{-29.3}	105.6 ^{+68.9} _{-40.4}	109.0 ^{+61.0} _{-51.3}	107.0 ^{+60.5} _{-43.6}	135.3 ^{+47.2} _{-43.5}
a_0	285.22	286.7 ^{+57.0} _{-47.0}	280.9 ^{+39.3} _{-30.5}	286.4 ^{+58.7} _{-35.9}	264.2 ^{+30.3} _{-20.0}	287.3 ^{+46.9} _{-37.2}	286.0 ^{+41.3} _{-41.4}	276.4 ^{+38.4} _{-30.8}	284.5 ^{+31.4} _{-26.5}
$L(P_0 [\text{bar}])$	0.006	0.0 ^{+0.4} _{-0.3}	0.0 ^{+0.3} _{-0.3}	-0.0 ^{+0.4} _{-0.4}	0.2 ^{+0.2} _{-0.3}	-0.0 ^{+0.4} _{-0.3}	-0.0 ^{+0.5} _{-0.3}	0.1 ^{+0.4} _{-0.3}	0.0 ^{+0.2} _{-0.2}
$R [R_\oplus]$	1.0	1.0 ^{+0.1} _{-0.1}	1.02 ^{+0.07} _{-0.07}	1.03 ^{+0.05} _{-0.05}	1.02 ^{+0.04} _{-0.04}	1.00 ^{+0.08} _{-0.08}	1.03 ^{+0.05} _{-0.05}	1.01 ^{+0.04} _{-0.04}	1.00 ^{+0.03} _{-0.03}
$L(M [M_\oplus])$	0.0	-0.0 ^{+0.3} _{-0.3}	0.0 ^{+0.3} _{-0.3}	0.0 ^{+0.3} _{-0.3}	0.0 ^{+0.3} _{-0.3}	0.0 ^{+0.3} _{-0.3}	0.0 ^{+0.3} _{-0.3}	0.0 ^{+0.3} _{-0.3}	0.0 ^{+0.3} _{-0.3}
$L(\text{N}_2)$	-0.107	-7.1 ^{+4.3} _{-4.5}	-7.5 ^{+4.6} _{-4.7}	-7.4 ^{+4.5} _{-4.6}	-7.5 ^{+4.6} _{-4.7}	-7.5 ^{+4.7} _{-4.7}	-7.4 ^{+4.5} _{-4.6}	-7.5 ^{+4.5} _{-4.7}	-7.6 ^{+4.8} _{-4.5}
$L(\text{O}_2)$	-0.679	-7.6 ^{+4.4} _{-4.3}	-7.8 ^{+4.6} _{-4.2}	-7.5 ^{+4.5} _{-4.6}	-7.4 ^{+4.7} _{-4.9}	-7.5 ^{+4.6} _{-4.5}	-7.2 ^{+4.4} _{-4.7}	-7.5 ^{+4.7} _{-4.5}	-7.9 ^{+4.9} _{-4.6}
$L(\text{H}_2\text{O})$	-3.000	-3.1 ^{+1.0} _{-1.1}	-2.8 ^{+0.7} _{-0.8}	-2.6 ^{+0.8} _{-0.8}	-3.1 ^{+0.6} _{-0.6}	-2.8 ^{+0.9} _{-0.9}	-2.7 ^{+0.7} _{-0.9}	-3.0 ^{+0.6} _{-0.7}	-2.9 ^{+0.5} _{-0.5}
$L(\text{CO}_2)$	-3.387	-3.7 ^{+0.9} _{-0.9}	-3.3 ^{+0.7} _{-0.7}	-3.1 ^{+0.8} _{-0.7}	-3.6 ^{+0.6} _{-0.5}	-3.3 ^{+0.8} _{-0.8}	-3.2 ^{+0.6} _{-0.8}	-3.4 ^{+0.5} _{-0.6}	-3.3 ^{+0.4} _{-0.5}
$L(\text{CH}_4)$	-5.770	-8.8 ^{+3.0} _{-3.5}	-9.3 ^{+3.1} _{-3.5}	-7.9 ^{+2.3} _{-4.2}	-6.9 ^{+1.1} _{-4.3}	-9.2 ^{+3.2} _{-3.4}	-7.9 ^{+2.3} _{-4.2}	-6.3 ^{+0.9} _{-2.0}	-5.8 ^{+0.6} _{-0.6}
$L(\text{O}_3)$	-6.523	-7.2 ^{+1.1} _{-4.3}	-6.5 ^{+0.5} _{-0.5}	-6.4 ^{+0.6} _{-0.6}	-6.7 ^{+0.4} _{-0.4}	-6.5 ^{+0.7} _{-0.7}	-6.5 ^{+0.5} _{-0.6}	-6.6 ^{+0.4} _{-0.5}	-6.5 ^{+0.4} _{-0.4}
$L(\text{CO})$	-6.903	-7.6 ^{+4.4} _{-4.2}	-7.5 ^{+4.5} _{-4.6}	-8.0 ^{+4.8} _{-4.4}	-7.9 ^{+4.6} _{-4.3}	-7.7 ^{+4.5} _{-4.3}	-7.8 ^{+4.4} _{-4.5}	-8.0 ^{+4.4} _{-4.3}	-8.3 ^{+4.3} _{-4.2}
$L(\text{N}_2\text{O})$	-6.495	-8.3 ^{+3.8} _{-3.7}	-8.9 ^{+3.9} _{-3.6}	-8.6 ^{+3.5} _{-3.8}	-9.0 ^{+3.2} _{-3.7}	-8.5 ^{+4.0} _{-4.0}	-8.8 ^{+3.6} _{-3.6}	-9.2 ^{+3.3} _{-3.6}	-9.4 ^{+3.3} _{-3.4}

Notes. Here, $L(\cdot)$ stands for $\log_{10}(\cdot)$.

Table D.4: Retrieval results for the 4 – 18.5 μm wavelength range for the optimized case.

Parameter	Input	R=20				R=35			
		S/N=5	S/N=10	S/N=15	S/N=20	S/N=5	S/N=10	S/N=15	S/N=20
$\sqrt[4]{a_4}$	1.14	1.2 ^{+0.3} _{-0.2}	1.0 ^{+0.2} _{-0.2}	1.0 ^{+0.2} _{-0.2}	1.0 ^{+0.2} _{-0.2}	1.1 ^{+0.2} _{-0.2}	1.0 ^{+0.2} _{-0.2}	1.0 ^{+0.2} _{-0.2}	1.0 ^{+0.2} _{-0.2}
a_3	23.12	22.6 ^{+18.3} _{-11.5}	13.1 ^{+9.8} _{-6.3}	13.0 ^{+7.8} _{-6.1}	11.7 ^{+8.5} _{-5.6}	16.4 ^{+15.1} _{-8.0}	10.8 ^{+9.2} _{-5.4}	12.2 ^{+10.8} _{-5.8}	12.1 ^{+11.2} _{-5.4}
a_2	99.70	101.3 ^{+51.4} _{-42.6}	61.5 ^{+42.6} _{-31.9}	51.7 ^{+34.6} _{-26.4}	49.0 ^{+32.9} _{-25.0}	71.5 ^{+49.6} _{-34.7}	39.5 ^{+29.5} _{-20.3}	55.6 ^{+43.9} _{-27.4}	47.8 ^{+39.1} _{-20.3}
a_1	146.63	135.8 ^{+57.9} _{-56.7}	132.1 ^{+62.6} _{-47.6}	94.7 ^{+71.5} _{-39.4}	94.7 ^{+61.3} _{-32.5}	113.8 ^{+53.7} _{-44.9}	65.7 ^{+36.2} _{-23.4}	112.4 ^{+81.2} _{-45.4}	89.8 ^{+47.5} _{-40.3}
a_0	285.22	211.1 ^{+60.6} _{-79.7}	304.6 ^{+45.6} _{-36.4}	283.3 ^{+55.6} _{-37.6}	290.9 ^{+48.1} _{-28.4}	246.6 ^{+56.3} _{-67.9}	259.4 ^{+30.6} _{-28.2}	310.0 ^{+55.4} _{-44.4}	275.8 ^{+29.8} _{-28.1}
$L(P_0 [\text{bar}])$	0.006	0.5 ^{+0.3} _{-0.3}	-0.1 ^{+0.3} _{-0.3}	0.1 ^{+0.5} _{-0.4}	-0.0 ^{+0.3} _{-0.4}	0.4 ^{+0.3} _{-0.4}	0.4 ^{+0.3} _{-0.4}	-0.2 ^{+0.5} _{-0.4}	0.1 ^{+0.4} _{-0.3}
$R [R_\oplus]$	1.0	0.9 ^{+0.1} _{-0.1}	0.98 ^{+0.09} _{-0.09}	0.99 ^{+0.07} _{-0.07}	1.01 ^{+0.06} _{-0.05}	0.9 ^{+0.1} _{-0.1}	1.00 ^{+0.07} _{-0.08}	1.01 ^{+0.05} _{-0.05}	1.01 ^{+0.04} _{-0.04}
$L(M [M_\oplus])$	0.0	0.0 ^{+0.3} _{-0.3}	0.0 ^{+0.3} _{-0.3}	0.0 ^{+0.3} _{-0.3}	0.0 ^{+0.3} _{-0.3}	0.0 ^{+0.3} _{-0.3}	-0.0 ^{+0.3} _{-0.3}	0.0 ^{+0.3} _{-0.3}	0.0 ^{+0.3} _{-0.3}
$L(\text{N}_2)$	-0.107	-6.6 ^{+4.0} _{-4.4}	-7.2 ^{+4.1} _{-4.6}	-7.0 ^{+4.1} _{-4.6}	-7.1 ^{+4.3} _{-4.7}	-8.0 ^{+4.3} _{-4.1}	-7.8 ^{+4.6} _{-4.4}	-7.8 ^{+4.7} _{-4.4}	-7.6 ^{+4.6} _{-4.6}
$L(\text{O}_2)$	-0.679	-7.3 ^{+4.4} _{-4.4}	-7.8 ^{+4.4} _{-4.4}	-7.9 ^{+4.5} _{-4.2}	-7.3 ^{+4.3} _{-4.5}	-7.7 ^{+4.6} _{-4.5}	-7.3 ^{+4.2} _{-4.5}	-7.5 ^{+4.5} _{-4.5}	-7.3 ^{+4.6} _{-4.8}
$L(\text{H}_2\text{O})$	-3.000	-3.9 ^{+0.9} _{-1.4}	-2.1 ^{+0.9} _{-0.9}	-2.5 ^{+1.1} _{-0.9}	-2.2 ^{+0.8} _{-0.8}	-3.3 ^{+1.1} _{-0.8}	-3.1 ^{+0.9} _{-0.8}	-2.0 ^{+0.9} _{-0.9}	-2.7 ^{+0.7} _{-0.8}
$L(\text{CO}_2)$	-3.387	-6.3 ^{+1.9} _{-4.3}	-3.5 ^{+1.0} _{-1.1}	-3.5 ^{+1.0} _{-0.8}	-3.1 ^{+0.7} _{-0.8}	-5.0 ^{+1.4} _{-3.1}	-3.9 ^{+0.9} _{-0.8}	-2.8 ^{+0.8} _{-0.9}	-3.4 ^{+0.7} _{-0.7}
$L(\text{CH}_4)$	-5.770	-9.6 ^{+2.8} _{-3.1}	-9.5 ^{+3.3} _{-3.2}	-9.4 ^{+3.0} _{-3.4}	-8.8 ^{+2.9} _{-3.7}	-10.1 ^{+2.9} _{-2.9}	-9.9 ^{+3.0} _{-3.1}	-7.8 ^{+2.5} _{-4.4}	-6.7 ^{+1.1} _{-3.9}
$L(\text{O}_3)$	-6.523	-9.7 ^{+2.4} _{-3.1}	-6.2 ^{+0.7} _{-0.7}	-6.5 ^{+0.7} _{-0.6}	-6.2 ^{+0.6} _{-0.6}	-7.2 ^{+0.9} _{-2.1}	-6.8 ^{+0.6} _{-0.6}	-6.0 ^{+0.7} _{-0.7}	-6.5 ^{+0.5} _{-0.5}
$L(\text{CO})$	-6.903	-8.9 ^{+3.9} _{-3.6}	-7.8 ^{+4.6} _{-4.5}	-7.2 ^{+4.3} _{-4.4}	-7.7 ^{+4.3} _{-4.5}	-8.2 ^{+4.5} _{-4.1}	-8.1 ^{+4.7} _{-4.3}	-7.8 ^{+4.6} _{-4.5}	-8.0 ^{+4.3} _{-4.3}
$L(\text{N}_2\text{O})$	-6.495	-9.7 ^{+3.5} _{-3.1}	-8.2 ^{+3.8} _{-4.0}	-8.4 ^{+3.7} _{-3.8}	-8.5 ^{+3.6} _{-3.8}	-8.7 ^{+3.6} _{-3.5}	-8.9 ^{+3.4} _{-3.6}	-9.3 ^{+3.7} _{-3.5}	-9.2 ^{+3.2} _{-3.4}

Parameter	Input	R=50				R=100			
		S/N=5	S/N=10	S/N=15	S/N=20	S/N=5	S/N=10	S/N=15	S/N=20
$\sqrt[4]{a_4}$	1.14	1.0 ^{+0.2} _{-0.2}	1.0 ^{+0.2} _{-0.2}	1.0 ^{+0.2} _{-0.2}	1.0 ^{+0.2} _{-0.2}	1.0 ^{+0.2} _{-0.2}	1.1 ^{+0.2} _{-0.2}	1.1 ^{+0.2} _{-0.2}	1.1 ^{+0.2} _{-0.2}
a_3	23.12	13.1 ^{+10.4} _{-6.5}	11.5 ^{+7.8} _{-5.5}	13.9 ^{+10.5} _{-5.8}	15.7 ^{+13.0} _{-6.7}	13.2 ^{+9.8} _{-6.3}	17.0 ^{+13.7} _{-7.5}	16.3 ^{+13.5} _{-7.2}	19.7 ^{+14.4} _{-8.7}
a_2	99.70	59.2 ^{+44.2} _{-31.6}	36.8 ^{+22.5} _{-17.5}	62.0 ^{+42.8} _{-25.8}	74.7 ^{+44.0} _{-28.0}	53.6 ^{+36.4} _{-26.3}	81.4 ^{+57.7} _{-35.6}	73.6 ^{+41.0} _{-27.1}	84.6 ^{+40.5} _{-27.7}
a_1	146.63	125.9 ^{+69.8} _{-51.9}	60.8 ^{+29.0} _{-20.1}	113.3 ^{+92.3} _{-41.9}	130.1 ^{+68.4} _{-48.3}	97.0 ^{+55.4} _{-33.6}	156.6 ^{+101.0} _{-70.0}	118.9 ^{+62.2} _{-43.0}	132.7 ^{+51.0} _{-47.1}
a_0	285.22	298.7 ^{+56.7} _{-49.8}	257.1 ^{+24.7} _{-20.7}	299.9 ^{+63.9} _{-37.3}	298.7 ^{+40.7} _{-37.0}	280.5 ^{+41.7} _{-31.4}	325.9 ^{+71.9} _{-53.1}	282.2 ^{+43.2} _{-28.6}	283.1 ^{+31.3} _{-27.3}
$L(P_0 [\text{bar}])$	0.006	-0.1 ^{+0.4} _{-0.4}	0.4 ^{+0.3} _{-0.3}	-0.1 ^{+0.4} _{-0.4}	-0.1 ^{+0.3} _{-0.2}	0.1 ^{+0.3} _{-0.3}	-0.3 ^{+0.4} _{-0.3}	0.0 ^{+0.3} _{-0.3}	0.0 ^{+0.3} _{-0.2}
$R [R_\oplus]$	1.0	1.0 ^{+0.1} _{-0.1}	1.01 ^{+0.07} _{-0.06}	1.01 ^{+0.05} _{-0.05}	1.00 ^{+0.04} _{-0.03}	1.00 ^{+0.08} _{-0.08}	1.01 ^{+0.05} _{-0.05}	1.00 ^{+0.03} _{-0.03}	1.00 ^{+0.02} _{-0.02}
$L(M [M_\oplus])$	0.0	0.0 ^{+0.3} _{-0.3}	0.0 ^{+0.3} _{-0.3}	0.0 ^{+0.3} _{-0.3}	0.0 ^{+0.3} _{-0.3}	0.0 ^{+0.3} _{-0.3}	0.0 ^{+0.3} _{-0.3}	0.0 ^{+0.3} _{-0.3}	0.0 ^{+0.3} _{-0.3}
$L(\text{N}_2)$	-0.107	-7.6 ^{+4.3} _{-4.2}	-7.6 ^{+4.5} _{-4.3}	-7.3 ^{+4.3} _{-4.3}	-7.5 ^{+4.6} _{-4.6}	-7.9 ^{+4.7} _{-4.4}	-7.6 ^{+4.6} _{-4.8}	-7.5 ^{+4.6} _{-4.4}	-7.4 ^{+4.7} _{-4.6}
$L(\text{O}_2)$	-0.679	-7.7 ^{+4.5} _{-4.3}	-7.4 ^{+4.4} _{-4.6}	-7.4 ^{+4.5} _{-4.6}	-7.2 ^{+4.4} _{-4.7}	-7.1 ^{+4.3} _{-4.7}	-8.1 ^{+4.9} _{-4.3}	-7.4 ^{+4.5} _{-4.7}	-7.8 ^{+4.9} _{-4.7}
$L(\text{H}_2\text{O})$	-3.000	-2.4 ^{+1.0} _{-1.1}	-3.1 ^{+0.8} _{-0.7}	-2.3 ^{+0.8} _{-0.9}	-2.7 ^{+0.6} _{-0.7}	-2.6 ^{+0.8} _{-0.8}	-2.2 ^{+0.8} _{-0.8}	-2.9 ^{+0.6} _{-0.6}	-3.0 ^{+0.5} _{-0.5}
$L(\text{CO}_2)$	-3.387	-3.6 ^{+1.1} _{-1.3}	-3.8 ^{+0.7} _{-0.6}	-3.0 ^{+0.8} _{-0.7}	-3.1 ^{+0.5} _{-0.6}	-3.5 ^{+0.8} _{-0.8}	-2.8 ^{+0.7} _{-0.7}	-3.3 ^{+0.6} _{-0.6}	-3.4 ^{+0.5} _{-0.5}
$L(\text{CH}_4)$	-5.770	-9.9 ^{+3.2} _{-3.1}	-9.1 ^{+2.6} _{-3.7}	-6.2 ^{+1.2} _{-3.9}	-5.7 ^{+0.6} _{-0.7}	-8.4 ^{+2.5} _{-3.8}	-5.5 ^{+0.9} _{-1.1}	-5.8 ^{+0.6} _{-0.6}	-5.8 ^{+0.5} _{-0.5}
$L(\text{O}_3)$	-6.523	-6.4 ^{+0.8} _{-1.0}	-6.8 ^{+0.5} _{-0.5}	-6.2 ^{+0.6} _{-0.6}	-6.3 ^{+0.4} _{-0.5}	-6.5 ^{+0.6} _{-0.6}	-6.1 ^{+0.6} _{-0.5}	-6.5 ^{+0.5} _{-0.4}	-6.5 ^{+0.4} _{-0.4}
$L(\text{CO})$	-6.903	-8.2 ^{+4.5} _{-3.9}	-8.0 ^{+4.6} _{-4.2}	-8.0 ^{+4.5} _{-4.4}	-8.3 ^{+4.6} _{-4.1}	-7.4 ^{+4.6} _{-4.4}	-7.8 ^{+4.3} _{-4.5}	-7.9 ^{+4.3} _{-4.4}	-8.7 ^{+4.2} _{-4.0}
$L(\text{N}_2\text{O})$	-6.495	-8.5 ^{+3.9} _{-3.9}	-9.2 ^{+3.4} _{-3.3}	-9.0 ^{+3.5} _{-3.5}	-9.3 ^{+3.2} _{-3.5}	-8.7 ^{+3.7} _{-3.7}	-9.0 ^{+3.7} _{-3.7}	-9.5 ^{+3.2} _{-3.4}	-9.9 ^{+3.1} _{-3.2}

Notes. Here, $L(\cdot)$ stands for $\log_{10}(\cdot)$.

Table D.5: Retrieval results for the 6 – 17 μm wavelength range for the nominal case.

Parameter	Input	R=20				R=35			
		S/N=5	S/N=10	S/N=15	S/N=20	S/N=5	S/N=10	S/N=15	S/N=20
$\sqrt{a_4}$	1.14	1.2 ^{+0.3} _{-0.3}	1.2 ^{+0.3} _{-0.3}	1.1 ^{+0.2} _{-0.2}	1.1 ^{+0.2} _{-0.2}	1.2 ^{+0.3} _{-0.3}	1.1 ^{+0.2} _{-0.2}	1.1 ^{+0.2} _{-0.2}	1.1 ^{+0.2} _{-0.2}
a_3	23.12	43.0 ^{+29.6} _{-23.8}	30.0 ^{+29.9} _{-17.0}	17.9 ^{+17.6} _{-9.1}	15.4 ^{+11.3} _{-7.3}	35.5 ^{+26.6} _{-18.3}	15.5 ^{+11.6} _{-7.5}	16.8 ^{+16.3} _{-8.7}	16.8 ^{+14.4} _{-7.8}
a_2	99.70	167.4 ^{+96.9} _{-77.4}	120.6 ^{+96.3} _{-62.6}	71.6 ^{+50.3} _{-33.6}	59.6 ^{+31.5} _{-25.6}	130.7 ^{+97.7} _{-62.0}	63.4 ^{+34.7} _{-27.9}	61.4 ^{+57.6} _{-28.2}	63.7 ^{+41.9} _{-26.0}
a_1	146.63	148.2 ^{+122.3} _{-79.8}	118.5 ^{+71.1} _{-47.4}	101.1 ^{+59.8} _{-37.0}	80.6 ^{+41.1} _{-28.1}	103.7 ^{+117.6} _{-54.7}	96.6 ^{+40.7} _{-32.6}	84.1 ^{+81.8} _{-34.6}	86.8 ^{+55.1} _{-38.3}
a_0	285.22	217.6 ^{+92.3} _{-88.8}	235.7 ^{+47.4} _{-70.0}	269.6 ^{+37.1} _{-34.3}	258.0 ^{+26.7} _{-26.5}	213.8 ^{+53.4} _{-61.3}	269.6 ^{+35.4} _{-32.5}	261.2 ^{+45.5} _{-27.0}	258.2 ^{+29.4} _{-22.8}
$L(P_0 [\text{bar}])$	0.006	0.4 ^{+0.3} _{-0.4}	0.3 ^{+0.2} _{-0.3}	0.2 ^{+0.3} _{-0.3}	0.3 ^{+0.2} _{-0.3}	0.5 ^{+0.2} _{-0.3}	0.2 ^{+0.3} _{-0.3}	0.2 ^{+0.3} _{-0.4}	0.3 ^{+0.3} _{-0.3}
$R [R_\oplus]$	1.0	0.9 ^{+0.1} _{-0.1}	1.01 ^{+0.1} _{-0.09}	1.00 ^{+0.09} _{-0.08}	1.01 ^{+0.07} _{-0.07}	0.9 ^{+0.1} _{-0.1}	0.99 ^{+0.09} _{-0.08}	1.01 ^{+0.07} _{-0.07}	1.01 ^{+0.06} _{-0.06}
$L(M [M_\oplus])$	0.0	0.0 ^{+0.3} _{-0.3}	-0.0 ^{+0.3} _{-0.3}	0.0 ^{+0.3} _{-0.3}	0.0 ^{+0.3} _{-0.3}	0.0 ^{+0.3} _{-0.3}	0.0 ^{+0.3} _{-0.3}	0.0 ^{+0.3} _{-0.3}	0.0 ^{+0.3} _{-0.3}
$L(\text{N}_2)$	-0.107	-7.5 ^{+4.2} _{-4.3}	-7.4 ^{+4.3} _{-4.4}	-7.4 ^{+4.4} _{-4.5}	-7.5 ^{+4.8} _{-4.6}	-8.1 ^{+4.4} _{-4.1}	-7.6 ^{+4.7} _{-4.3}	-7.1 ^{+4.4} _{-4.8}	-7.6 ^{+4.7} _{-4.8}
$L(\text{O}_2)$	-0.679	-7.7 ^{+4.5} _{-4.1}	-7.5 ^{+4.4} _{-4.1}	-7.2 ^{+4.4} _{-4.5}	-7.8 ^{+4.8} _{-4.7}	-6.8 ^{+4.2} _{-4.9}	-7.3 ^{+4.4} _{-4.5}	-7.7 ^{+4.7} _{-4.6}	-7.6 ^{+4.7} _{-4.6}
$L(\text{H}_2\text{O})$	-3.000	-9.5 ^{+3.3} _{-3.1}	-5.5 ^{+2.2} _{-5.1}	-3.2 ^{+0.9} _{-1.1}	-3.2 ^{+0.8} _{-0.8}	-8.6 ^{+3.4} _{-3.6}	-3.2 ^{+1.0} _{-1.2}	-3.2 ^{+0.9} _{-0.8}	-3.2 ^{+0.7} _{-0.7}
$L(\text{CO}_2)$	-3.387	-5.1 ^{+1.0} _{-2.2}	-4.0 ^{+0.6} _{-0.5}	-3.6 ^{+0.7} _{-0.6}	-3.8 ^{+0.6} _{-0.6}	-4.5 ^{+0.6} _{-0.7}	-3.6 ^{+0.8} _{-0.7}	-3.7 ^{+0.7} _{-0.7}	-3.8 ^{+0.6} _{-0.6}
$L(\text{CH}_4)$	-5.770	-9.6 ^{+2.8} _{-3.1}	-9.1 ^{+3.1} _{-3.5}	-8.4 ^{+2.8} _{-3.6}	-9.3 ^{+3.0} _{-3.5}	-9.6 ^{+3.1} _{-3.2}	-8.9 ^{+3.2} _{-3.9}	-9.2 ^{+3.0} _{-3.5}	-9.2 ^{+2.9} _{-3.5}
$L(\text{O}_3)$	-6.523	-10.4 ^{+2.7} _{-2.7}	-7.8 ^{+1.1} _{-3.5}	-6.7 ^{+0.6} _{-0.6}	-6.8 ^{+0.5} _{-0.5}	-9.6 ^{+2.3} _{-3.1}	-6.7 ^{+0.7} _{-0.7}	-6.8 ^{+0.6} _{-0.5}	-6.8 ^{+0.5} _{-0.4}
$L(\text{CO})$	-6.903	-7.8 ^{+4.4} _{-4.1}	-7.1 ^{+4.5} _{-4.4}	-7.8 ^{+4.4} _{-4.3}	-7.4 ^{+4.7} _{-4.8}	-7.7 ^{+4.4} _{-4.2}	-7.4 ^{+4.4} _{-4.4}	-7.6 ^{+4.7} _{-4.8}	-7.4 ^{+4.7} _{-4.7}
$L(\text{N}_2\text{O})$	-6.495	-9.7 ^{+3.0} _{-3.0}	-9.4 ^{+3.3} _{-3.3}	-8.9 ^{+3.9} _{-3.7}	-8.5 ^{+3.6} _{-4.0}	-10.0 ^{+2.9} _{-2.9}	-8.7 ^{+3.8} _{-3.7}	-9.0 ^{+3.7} _{-3.8}	-8.9 ^{+3.6} _{-3.7}

Parameter	Input	R=50				R=100			
		S/N=5	S/N=10	S/N=15	S/N=20	S/N=5	S/N=10	S/N=15	S/N=20
$\sqrt{a_4}$	1.14	1.2 ^{+0.3} _{-0.3}	1.1 ^{+0.2} _{-0.2}	1.1 ^{+0.2} _{-0.2}	1.1 ^{+0.2} _{-0.2}	1.1 ^{+0.3} _{-0.2}	1.1 ^{+0.2} _{-0.2}	1.1 ^{+0.2} _{-0.2}	1.1 ^{+0.2} _{-0.2}
a_3	23.12	33.5 ^{+22.8} _{-17.3}	15.0 ^{+14.3} _{-7.6}	16.3 ^{+13.6} _{-7.8}	15.5 ^{+12.2} _{-6.6}	17.8 ^{+18.9} _{-9.1}	16.2 ^{+13.6} _{-7.7}	19.0 ^{+16.5} _{-8.5}	19.4 ^{+15.5} _{-8.7}
a_2	99.70	127.0 ^{+75.9} _{-57.5}	62.9 ^{+39.9} _{-28.5}	63.1 ^{+48.4} _{-28.5}	66.3 ^{+30.7} _{-24.3}	70.1 ^{+43.5} _{-31.0}	67.0 ^{+35.9} _{-26.8}	78.3 ^{+52.3} _{-26.8}	81.7 ^{+48.2} _{-30.0}
a_1	146.63	118.8 ^{+109.9} _{-58.6}	94.5 ^{+47.3} _{-31.0}	92.7 ^{+82.6} _{-48.3}	92.8 ^{+50.9} _{-33.7}	102.3 ^{+45.1} _{-35.8}	98.4 ^{+56.9} _{-39.0}	126.9 ^{+60.6} _{-54.5}	119.9 ^{+72.1} _{-50.9}
a_0	285.22	232.6 ^{+49.7} _{-50.4}	271.5 ^{+34.5} _{-30.5}	266.7 ^{+48.3} _{-32.9}	261.4 ^{+32.4} _{-22.0}	269.0 ^{+37.2} _{-32.6}	271.0 ^{+36.1} _{-29.7}	281.0 ^{+35.3} _{-32.5}	275.9 ^{+43.7} _{-30.8}
$L(P_0 [\text{bar}])$	0.006	0.3 ^{+0.2} _{-0.3}	0.1 ^{+0.3} _{-0.3}	0.2 ^{+0.5} _{-0.4}	0.2 ^{+0.3} _{-0.3}	0.1 ^{+0.3} _{-0.3}	0.1 ^{+0.3} _{-0.3}	0.0 ^{+0.3} _{-0.2}	0.1 ^{+0.3} _{-0.3}
$R [R_\oplus]$	1.0	1.0 ^{+0.1} _{-0.1}	1.01 ^{+0.08} _{-0.08}	1.01 ^{+0.06} _{-0.06}	1.02 ^{+0.05} _{-0.05}	1.0 ^{+0.1} _{-0.1}	1.01 ^{+0.07} _{-0.06}	1.02 ^{+0.05} _{-0.05}	1.01 ^{+0.04} _{-0.04}
$L(M [M_\oplus])$	0.0	0.0 ^{+0.3} _{-0.3}	0.0 ^{+0.3} _{-0.3}	0.0 ^{+0.3} _{-0.3}	-0.0 ^{+0.3} _{-0.3}	-0.0 ^{+0.3} _{-0.3}	0.0 ^{+0.3} _{-0.3}	-0.0 ^{+0.3} _{-0.3}	0.0 ^{+0.3} _{-0.3}
$L(\text{N}_2)$	-0.107	-8.0 ^{+4.5} _{-4.1}	-7.4 ^{+4.6} _{-4.8}	-7.6 ^{+4.7} _{-4.5}	-7.5 ^{+4.6} _{-4.6}	-7.4 ^{+4.3} _{-4.4}	-7.3 ^{+4.5} _{-4.7}	-7.7 ^{+4.9} _{-4.7}	-7.4 ^{+4.7} _{-4.7}
$L(\text{O}_2)$	-0.679	-7.3 ^{+4.4} _{-4.4}	-7.4 ^{+4.4} _{-4.5}	-7.6 ^{+4.6} _{-4.6}	-7.7 ^{+4.9} _{-4.7}	-7.4 ^{+4.5} _{-4.6}	-7.7 ^{+4.7} _{-4.5}	-7.3 ^{+4.5} _{-4.6}	-7.5 ^{+4.8} _{-4.6}
$L(\text{H}_2\text{O})$	-3.000	-7.5 ^{+3.2} _{-4.5}	-3.0 ^{+0.9} _{-0.9}	-3.1 ^{+0.8} _{-0.9}	-3.2 ^{+0.7} _{-0.6}	-3.5 ^{+1.1} _{-1.6}	-3.0 ^{+0.7} _{-0.7}	-2.9 ^{+0.6} _{-0.6}	-3.0 ^{+0.6} _{-0.6}
$L(\text{CO}_2)$	-3.387	-4.1 ^{+0.6} _{-0.6}	-3.5 ^{+0.7} _{-0.7}	-3.6 ^{+0.7} _{-0.8}	-3.6 ^{+0.6} _{-0.6}	-3.6 ^{+0.7} _{-0.6}	-3.5 ^{+0.7} _{-0.6}	-3.4 ^{+0.5} _{-0.6}	-3.5 ^{+0.6} _{-0.6}
$L(\text{CH}_4)$	-5.770	-8.8 ^{+2.9} _{-3.5}	-9.1 ^{+3.1} _{-3.6}	-9.3 ^{+3.1} _{-3.5}	-8.2 ^{+2.2} _{-3.9}	-9.0 ^{+3.1} _{-3.5}	-8.4 ^{+2.5} _{-4.1}	-7.1 ^{+1.4} _{-4.5}	-6.3 ^{+0.9} _{-2.6}
$L(\text{O}_3)$	-6.523	-8.4 ^{+1.5} _{-3.7}	-6.6 ^{+0.6} _{-0.5}	-6.7 ^{+0.6} _{-0.6}	-6.7 ^{+0.5} _{-0.5}	-6.8 ^{+0.7} _{-1.3}	-6.6 ^{+0.5} _{-0.5}	-6.6 ^{+0.5} _{-0.4}	-6.6 ^{+0.4} _{-0.5}
$L(\text{CO})$	-6.903	-8.0 ^{+4.7} _{-4.1}	-7.4 ^{+4.5} _{-4.7}	-7.4 ^{+4.5} _{-4.7}	-7.9 ^{+4.6} _{-4.4}	-7.2 ^{+4.4} _{-4.5}	-7.7 ^{+4.8} _{-4.6}	-7.2 ^{+4.4} _{-4.6}	-7.2 ^{+4.5} _{-4.8}
$L(\text{N}_2\text{O})$	-6.495	-9.5 ^{+3.0} _{-3.1}	-8.9 ^{+3.9} _{-3.8}	-8.8 ^{+3.8} _{-3.6}	-9.3 ^{+3.6} _{-3.5}	-8.5 ^{+3.5} _{-3.8}	-8.5 ^{+3.6} _{-3.9}	-9.2 ^{+3.8} _{-3.6}	-9.3 ^{+3.6} _{-3.6}

Notes. Here, $L(\cdot)$ stands for $\log_{10}(\cdot)$.

Table D.6: Retrieval results for the 6 – 17 μm wavelength range for the optimized case.

Parameter	Input	R=20				R=35			
		S/N=5	S/N=10	S/N=15	S/N=20	S/N=5	S/N=10	S/N=15	S/N=20
$\sqrt[4]{a_4}$	1.14	1.3 ^{+0.3} _{-0.3}	1.1 ^{+0.2} _{-0.2}	1.0 ^{+0.2} _{-0.2}	1.0 ^{+0.2} _{-0.2}	1.1 ^{+0.2} _{-0.2}	1.0 ^{+0.2} _{-0.2}	1.0 ^{+0.2} _{-0.2}	1.1 ^{+0.2} _{-0.2}
a_3	23.12	32.1 ^{+27.0} _{-16.6}	14.7 ^{+11.3} _{-7.7}	11.4 ^{+8.5} _{-5.5}	12.6 ^{+9.3} _{-5.9}	18.4 ^{+12.0} _{-9.5}	13.3 ^{+10.0} _{-6.7}	12.2 ^{+10.3} _{-5.9}	14.3 ^{+10.4} _{-6.9}
a_2	99.70	113.7 ^{+76.8} _{-48.6}	64.6 ^{+43.4} _{-35.0}	46.9 ^{+33.7} _{-23.7}	54.6 ^{+38.5} _{-26.9}	80.2 ^{+41.0} _{-36.5}	55.2 ^{+32.8} _{-28.9}	49.5 ^{+32.5} _{-22.9}	54.5 ^{+37.8} _{-23.4}
a_1	146.63	114.4 ^{+79.8} _{-57.1}	114.1 ^{+71.8} _{-44.2}	87.6 ^{+55.1} _{-31.7}	110.4 ^{+63.1} _{-37.0}	125.6 ^{+64.4} _{-51.4}	97.7 ^{+55.9} _{-36.3}	91.4 ^{+48.6} _{-36.8}	88.7 ^{+65.9} _{-31.1}
a_0	285.22	194.6 ^{+68.0} _{-72.8}	277.5 ^{+53.6} _{-44.3}	276.4 ^{+46.8} _{-30.8}	310.2 ^{+46.0} _{-35.3}	247.1 ^{+47.8} _{-59.5}	281.9 ^{+44.8} _{-34.2}	283.4 ^{+38.2} _{-31.7}	277.0 ^{+42.8} _{-26.1}
$L(P_0 [\text{bar}])$	0.006	0.5 ^{+0.3} _{-0.4}	0.1 ^{+0.3} _{-0.4}	0.2 ^{+0.3} _{-0.4}	-0.2 ^{+0.4} _{-0.3}	0.3 ^{+0.3} _{-0.3}	0.1 ^{+0.3} _{-0.4}	0.1 ^{+0.4} _{-0.3}	0.1 ^{+0.3} _{-0.4}
$R [R_\oplus]$	1.0	1.0 ^{+0.1} _{-0.1}	0.96 ^{+0.1} _{-0.09}	0.99 ^{+0.07} _{-0.08}	0.99 ^{+0.06} _{-0.06}	0.9 ^{+0.1} _{-0.1}	0.98 ^{+0.08} _{-0.08}	1.00 ^{+0.06} _{-0.06}	1.00 ^{+0.04} _{-0.05}
$L(M [M_\oplus])$	0.0	0.0 ^{+0.3} _{-0.3}	-0.0 ^{+0.3} _{-0.3}	0.0 ^{+0.3} _{-0.3}	0.0 ^{+0.3} _{-0.3}	0.0 ^{+0.3} _{-0.3}	0.1 ^{+0.3} _{-0.3}	0.0 ^{+0.3} _{-0.3}	0.0 ^{+0.3} _{-0.3}
$L(\text{N}_2)$	-0.107	-7.7 ^{+4.2} _{-4.2}	-7.4 ^{+4.5} _{-4.4}	-7.4 ^{+4.4} _{-4.6}	-7.5 ^{+4.4} _{-4.7}	-7.4 ^{+4.5} _{-4.4}	-7.2 ^{+4.4} _{-4.6}	-7.8 ^{+4.7} _{-4.7}	-7.4 ^{+4.7} _{-4.6}
$L(\text{O}_2)$	-0.679	-7.0 ^{+4.8} _{-4.6}	-7.5 ^{+4.4} _{-4.4}	-7.4 ^{+4.4} _{-4.5}	-7.9 ^{+4.5} _{-4.3}	-6.7 ^{+4.3} _{-4.8}	-7.4 ^{+4.6} _{-4.5}	-7.8 ^{+4.7} _{-4.5}	-7.6 ^{+4.5} _{-4.5}
$L(\text{H}_2\text{O})$	-3.000	-5.1 ^{+1.5} _{-5.5}	-2.7 ^{+1.0} _{-0.9}	-2.6 ^{+1.0} _{-0.8}	-1.9 ^{+0.8} _{-0.8}	-3.3 ^{+0.9} _{-1.0}	-2.4 ^{+0.8} _{-0.9}	-2.5 ^{+0.8} _{-0.8}	-2.6 ^{+0.8} _{-0.7}
$L(\text{CO}_2)$	-3.387	-5.6 ^{+1.5} _{-3.0}	-4.0 ^{+1.0} _{-1.1}	-3.7 ^{+0.9} _{-0.8}	-3.0 ^{+0.8} _{-0.8}	-4.8 ^{+1.2} _{-2.0}	-3.5 ^{+0.8} _{-0.8}	-3.4 ^{+0.8} _{-0.7}	-3.4 ^{+0.7} _{-0.7}
$L(\text{CH}_4)$	-5.770	-9.9 ^{+2.7} _{-2.9}	-9.9 ^{+3.1} _{-2.9}	-9.5 ^{+2.9} _{-3.4}	-9.0 ^{+3.1} _{-3.6}	-9.6 ^{+2.8} _{-3.0}	-9.5 ^{+3.0} _{-3.4}	-9.1 ^{+2.8} _{-3.5}	-7.2 ^{+1.4} _{-4.2}
$L(\text{O}_3)$	-6.523	-10.6 ^{+2.7} _{-2.6}	-6.6 ^{+0.7} _{-0.7}	-6.5 ^{+0.6} _{-0.6}	-6.0 ^{+0.6} _{-0.6}	-7.2 ^{+0.8} _{-3.1}	-6.4 ^{+0.6} _{-0.6}	-6.4 ^{+0.6} _{-0.6}	-6.5 ^{+0.5} _{-0.5}
$L(\text{CO})$	-6.903	-7.5 ^{+4.3} _{-4.3}	-7.2 ^{+4.2} _{-4.5}	-7.2 ^{+4.3} _{-4.7}	-7.5 ^{+4.3} _{-4.5}	-6.7 ^{+4.0} _{-4.6}	-7.5 ^{+4.6} _{-4.6}	-7.5 ^{+4.4} _{-4.7}	-7.8 ^{+4.7} _{-4.5}
$L(\text{N}_2\text{O})$	-6.495	-10.1 ^{+3.1} _{-2.8}	-8.7 ^{+4.0} _{-3.8}	-8.9 ^{+3.8} _{-3.7}	-8.7 ^{+3.7} _{-3.7}	-8.7 ^{+3.6} _{-3.6}	-8.9 ^{+3.8} _{-3.8}	-9.1 ^{+3.5} _{-3.6}	-9.4 ^{+3.4} _{-3.4}

Parameter	Input	R=50				R=100			
		S/N=5	S/N=10	S/N=15	S/N=20	S/N=5	S/N=10	S/N=15	S/N=20
$\sqrt[4]{a_4}$	1.14	1.1 ^{+0.2} _{-0.2}	1.0 ^{+0.2} _{-0.2}	1.1 ^{+0.2} _{-0.2}	1.0 ^{+0.2} _{-0.2}	1.0 ^{+0.2} _{-0.2}	1.0 ^{+0.2} _{-0.2}	1.1 ^{+0.2} _{-0.2}	1.1 ^{+0.2} _{-0.2}
a_3	23.12	16.4 ^{+13.3} _{-8.1}	14.0 ^{+10.3} _{-7.1}	13.0 ^{+12.7} _{-6.5}	14.9 ^{+11.3} _{-6.8}	12.5 ^{+10.9} _{-6.0}	15.0 ^{+11.7} _{-7.5}	19.4 ^{+18.3} _{-8.9}	21.8 ^{+16.8} _{-9.8}
a_2	99.70	76.1 ^{+42.9} _{-37.6}	57.8 ^{+43.0} _{-31.1}	49.6 ^{+40.7} _{-23.1}	67.8 ^{+36.7} _{-30.5}	56.3 ^{+38.3} _{-28.2}	68.5 ^{+53.1} _{-33.7}	88.9 ^{+66.8} _{-37.4}	93.1 ^{+56.3} _{-32.7}
a_1	146.63	130.4 ^{+65.2} _{-49.4}	105.9 ^{+77.0} _{-43.8}	84.5 ^{+56.4} _{-32.7}	119.0 ^{+60.0} _{-59.8}	99.9 ^{+66.8} _{-37.2}	126.8 ^{+106.8} _{-59.3}	161.8 ^{+94.6} _{-83.2}	149.2 ^{+80.3} _{-59.5}
a_0	285.22	268.3 ^{+44.3} _{-45.0}	293.2 ^{+53.4} _{-34.0}	274.2 ^{+35.7} _{-27.1}	286.0 ^{+47.4} _{-37.7}	277.1 ^{+47.8} _{-33.1}	308.5 ^{+68.5} _{-51.4}	307.7 ^{+59.3} _{-51.1}	295.9 ^{+49.0} _{-37.8}
$L(P_0 [\text{bar}])$	0.006	0.2 ^{+0.3} _{-0.3}	-0.0 ^{+0.4} _{-0.4}	0.1 ^{+0.4} _{-0.3}	0.0 ^{+0.4} _{-0.3}	0.1 ^{+0.3} _{-0.4}	-0.2 ^{+0.5} _{-0.4}	-0.1 ^{+0.4} _{-0.3}	-0.1 ^{+0.3} _{-0.3}
$R [R_\oplus]$	1.0	0.9 ^{+0.1} _{-0.1}	0.99 ^{+0.07} _{-0.07}	1.00 ^{+0.05} _{-0.05}	1.00 ^{+0.04} _{-0.04}	0.99 ^{+0.09} _{-0.09}	1.00 ^{+0.06} _{-0.05}	1.00 ^{+0.03} _{-0.03}	1.00 ^{+0.03} _{-0.03}
$L(M [M_\oplus])$	0.0	0.0 ^{+0.3} _{-0.3}	-0.0 ^{+0.3} _{-0.3}	0.0 ^{+0.3} _{-0.3}	0.0 ^{+0.3} _{-0.3}	-0.0 ^{+0.3} _{-0.3}	0.0 ^{+0.3} _{-0.3}	0.0 ^{+0.3} _{-0.3}	0.0 ^{+0.3} _{-0.3}
$L(\text{N}_2)$	-0.107	-7.6 ^{+4.5} _{-4.2}	-7.2 ^{+4.4} _{-4.7}	-7.6 ^{+4.7} _{-4.7}	-7.6 ^{+4.6} _{-4.6}	-7.8 ^{+4.5} _{-4.1}	-7.4 ^{+4.6} _{-4.6}	-7.7 ^{+4.9} _{-4.5}	-7.5 ^{+4.7} _{-4.5}
$L(\text{O}_2)$	-0.679	-7.7 ^{+4.6} _{-4.3}	-7.3 ^{+4.4} _{-4.5}	-7.4 ^{+4.6} _{-4.8}	-7.3 ^{+4.5} _{-4.6}	-7.5 ^{+4.5} _{-4.5}	-7.2 ^{+4.5} _{-4.7}	-7.5 ^{+4.6} _{-4.5}	-7.9 ^{+4.7} _{-4.4}
$L(\text{H}_2\text{O})$	-3.000	-2.9 ^{+0.8} _{-0.7}	-2.4 ^{+0.9} _{-0.8}	-2.8 ^{+0.8} _{-0.8}	-2.8 ^{+0.7} _{-0.8}	-2.8 ^{+0.9} _{-0.9}	-2.4 ^{+0.9} _{-0.9}	-2.7 ^{+0.6} _{-0.7}	-2.8 ^{+0.6} _{-0.6}
$L(\text{CO}_2)$	-3.387	-4.3 ^{+1.1} _{-1.9}	-3.3 ^{+0.8} _{-0.8}	-3.4 ^{+0.7} _{-0.7}	-3.3 ^{+0.7} _{-0.7}	-3.7 ^{+0.9} _{-0.8}	-3.0 ^{+0.8} _{-0.8}	-3.1 ^{+0.6} _{-0.6}	-3.2 ^{+0.6} _{-0.6}
$L(\text{CH}_4)$	-5.770	-10.0 ^{+3.1} _{-2.9}	-8.7 ^{+2.9} _{-3.9}	-6.5 ^{+1.0} _{-3.7}	-5.9 ^{+0.8} _{-0.9}	-8.6 ^{+2.6} _{-3.7}	-5.8 ^{+1.0} _{-1.6}	-5.6 ^{+0.6} _{-0.7}	-5.6 ^{+0.6} _{-0.6}
$L(\text{O}_3)$	-6.523	-6.8 ^{+0.6} _{-0.6}	-6.3 ^{+0.6} _{-0.6}	-6.5 ^{+0.5} _{-0.5}	-6.5 ^{+0.6} _{-0.6}	-6.6 ^{+0.6} _{-0.6}	-6.2 ^{+0.7} _{-0.6}	-6.3 ^{+0.5} _{-0.5}	-6.4 ^{+0.4} _{-0.4}
$L(\text{CO})$	-6.903	-7.1 ^{+4.3} _{-4.5}	-7.4 ^{+4.6} _{-4.4}	-7.5 ^{+4.7} _{-4.7}	-7.4 ^{+4.5} _{-4.6}	-7.4 ^{+4.4} _{-4.6}	-7.7 ^{+4.8} _{-4.5}	-7.1 ^{+4.3} _{-4.7}	-7.6 ^{+4.7} _{-4.6}
$L(\text{N}_2\text{O})$	-6.495	-8.8 ^{+3.6} _{-3.7}	-8.4 ^{+3.5} _{-3.8}	-9.2 ^{+3.4} _{-3.4}	-9.4 ^{+3.2} _{-3.5}	-8.7 ^{+3.8} _{-3.7}	-8.8 ^{+3.5} _{-3.7}	-9.2 ^{+3.3} _{-3.6}	-9.6 ^{+3.3} _{-3.3}

Notes. Here, $L(\cdot)$ stands for $\log_{10}(\cdot)$.

Table E.1: Required observation time in days.

(a) Nominal case						
R		Observation Time [days]				
		20	35	50	100	
S/N	1 m Mirrors	5	48.6	85.7	122.5	249.1
		10	194.6	342.7	490.1	996.2
		15	437.8	771.0	1102.7	2241.5
		20	778.3	1370.6	1960.4	3984.8
	2 m Mirrors	5	4.7	8.2	11.7	23.9
		10	18.6	32.7	46.7	95.4
		15	41.9	73.5	105.0	214.7
		20	74.5	130.7	186.6	381.7
	3.5 m Mirrors	5	1.0	1.7	2.4	4.9
		10	3.8	6.7	9.5	19.6
		15	8.6	15.1	21.5	44.2
		20	15.3	26.8	38.2	78.5

(b) Optimized case						
R		Observation Time [days]				
		20	35	50	100	
S/N	1 m Mirrors	5	57.7	102.5	147.1	294.7
		10	230.6	410.0	588.5	1178.7
		15	518.9	922.2	1324.2	2652.2
		20	922.5	1639.5	2354.1	4714.9
	2 m Mirrors	5	4.0	7.1	10.2	20.6
		10	16.0	28.5	41.0	82.3
		15	36.2	64.2	92.1	185.2
		20	64.4	114.2	163.8	329.2
	3.5 m Mirrors	5	0.6	1.0	1.4	2.9
		10	2.2	3.9	5.7	11.4
		15	5.0	8.9	12.7	25.7
		20	8.9	15.8	22.6	45.8

Notes. Observation times necessary for *LIFE* to investigate an Earth-twin at 10 pc in orbit around a G2 star for the grid of R and S/N discussed in this publication. The S/N in the Table corresponds to the S/N at $11.2\ \mu\text{m}$. We consider three different aperture diameters (1m, 2m, and 3.5m). (a): Nominal case; (b): Optimized case.